TECHNISCHE
UNIVERSITÄT
DARMSTADT

Data Driven Estimation of Wall Shear Stress from Magnetic Resonance Imaging

Vom Fachbereich Mathematik

der Technischen Universität Darmstadt

zur Erlangung des Grades eines

Doktors der Naturwissenschaften

(Dr. rer. nat.)

genehmigte Dissertation

von

Gabriel Teschner, M.Sc.

aus Frankfurt am Main

Referent : Prof. Dr. Herbert Egger

Korreferent : Prof. Dr. Jan-Frederik Pietschmann

Tag der Einreichung: 09.02.2022

Tag der mündlichen Prüfung: 01.04.2022

Darmstadt, 2022

D17

Data Driven Estimation of Wall Shear Stress from Magnetic Resonance Imaging

Accepted doctoral thesis by Gabriel Teschner

Dissertationsort: Darmstadt, Technische Universität Darmstadt
Jahr der Veröffentlichung der Dissertation auf TUprints: 2023
Referent: Prof. Dr. Herbert Egger
Korreferent: Prof. Dr. Jan-Frederik Pietschmann

Date of submission: 09.02.2022
Date of thesis defense: 01.04.2022

Darmstadt – D17

Bitte zitieren Sie dieses Dokument als:
URN: urn:nbn:de:tuda-tuprints-232185
URL: https://tuprints.ulb.tu-darmstadt.de/23218

Dieses Dokument wird bereitgestellt von tuprints,
E-Publishing-Service der TU Darmstadt
http://tuprints.ulb.tu-darmstadt.de
tuprints@ulb.tu-darmstadt.de

Abstract

Flows occur in various applications in engineering and medicine. Dynamic quantities, in particular the forces, that the flowing viscous fluid exerts on the neighbouring material, are of special interest. Following the widely accepted flow model, these dynamic quantities are representable by derivatives of the velocity field.

A modification of magnetic resonance imaging is capable to measure besides morphological data, also velocity fields in the interior of an object. As a non-invasive method, it is in particular suited for *in vivo* investigations of the cardiovascular system.

This thesis deals with the problem of reconstructing the wall shear stress, the distribution of the shear forces, that the blood flow exerts on the aortic vessel wall. This involves the reconstruction of both the flow geometry and velocity from magnetic resonance data and the evaluation of the normal velocity derivative, the shear rate. At first glance, this problem might seem trivial. However, there are several issues:

- Magnetic resonance imaging acquires local means of the flow velocity with comparatively low spatial and temporal resolution. Additionally, the measurements are contaminated by noise.

- The blood flow exhibits boundary layers, where the flow field dramatically changes over small distances. This complicates an accurate approximation of the velocity field in the region near to the boundary.

- The flow geometry and the flow velocity are structurally connected: Just the shear-rate, that has to be evaluated, exhibits a discontinuity at the boundary.

In the first part of this work we present a framework for the purely data driven wall shear stress reconstruction. For this purpose, we approximate the flow geometry first, and then the flow velocity using parametric representations. The reconstruction method allows for a continuous analysis as regularization procedure for two coupled inverse problems. Since the corresponding forward operators satisfy a conditional stability estimate, convergence of the reconstruction method can be established under reasonable smoothness assumptions on the geometry and the flow velocity. These results widely carry over to the discrete setting, where we introduce discrete versions of the forward operators to minimize the data error.

In the second part of this work we use methods of data assimilation, to enhance the purely data driven reconstruction using a fluid dynamical model. In a first study, we utilize a variational approach for the enhancement of the velocity reconstruction under known geometry, that minimizes a functional consisting of a data error and a model error and was formerly developed and analyzed in our research group. The variational approach

is formally equivalent to an optimal control problem. Secondly, we demonstrate the basic possibility to enhance the geometry identification based on a fixed fluid dynamical model. For both methods, we utilize the widely accurate purely data driven reconstructions for linearization and localization of the applied fluid dynamic model.

For the assessment of the developed methods we have conducted a comprehensive validation in collaboration with experts of fluid dynamics and radiology from the Institute for Fluid Mechanics and Aerodynamics, Technical University Darmstadt, and the Department of Radiology – Medical Physics, University Hospital Freiburg, respectively. A big issue is the lack of *ground truth*. The wall shear stress is highly sensitve to perturbations of the environmental conditions. Hence, the experiments have to be performed with meticulous diligence, to ensure reproducibility and hence validity of the reference values, that are obtained from high-resolution laser Doppler anemometry or computational fluid dynamics. Additionally, we have developed highly robust and accurate but to specific flows limited reconstruction methods, to estimate the wall shear stress directly from the magnetic resonance data. Furthermore we fall back on virtual *in silico* data in some cases.

Already the purely data driven reconstruction method provides largely convincing results. However, the reconstruction is highly sensitve to perturbations of the geometry identification and reveals sometimes systematic errors due to the coarse resolution. Our analysis identifies the error sources and their contribution to the overall error. This offers a guideline for a suitable choice of several parameters in the measurement setup. Furthermore, the described shortcomings of the purely data driven reconstruction are essentially corrected by the provided data assimilation techniques. The specialization to the application in the aorta leads to a fully integrated reconstruction method with low computational effort, typical running times for all provided methods are in the range of several minutes using common hardware. Therefore, a valid estimation of wall shear stress in the aorta is feasible, even under the limitations of clinical routine.

This thesis was funded by the DFG via grant EG-331/1-1. The collaboration with the project partners resulted in the following papers:

- H. Egger and G. Teschner. On the Stable Estimation of Flow Geometry and Wall Shear Stress from Magnetic Resonance Images. *Inverse Problems*, 35:095001, 2019.
- A. Bauer, S. Wegt, M. Bopp, S. Jakirlic, C. Tropea, A. J. Krafft, N. Shokina, J. Hennig, G. Teschner and H. Egger. Comparison of Wall Shear Stress Estimates Obtained by Laser Doppler Velocimetry, Magnetic Resonance Imaging and Numerical Simulations. *Experiments in Fluids*, 60:1–16, 2019.
- N. Shokina, A. Bauer, G. Teschner, W. B. Buchenberg, C. Tropea, H. Egger, J. Hennig and A. J. Krafft. MR-based Wall Shear Stress Measurements in Fully Developed Turbulent Flow using the Clauser Plot Method. *Journal of Magnetic Resonance*, 305:16–21, 2019.
- N. Shokina, G. Teschner, A. Bauer, C. Tropea, H. Egger, J. Hennig and A. J. Krafft. Quantification of Wall Shear Stress in Large Blood Vessels using Magnetic Resonance Imaging. *Computational Technologies*, 24:4–27, 2019.

- N. Shokina, G. Teschner, A. Bauer, C. Tropea, H. Egger, J. Hennig and A. J. Krafft. Parametric Sequential Method for MRI-based Wall Shear Stress Quantification. *IEEE Transactions on Medical Imaging*, 40:1105–1112, 2020.

In this thesis, we will summarize the findings of the papers mentioned above and appropriatly extend them to an entire analysis of the wall shear stress reconstruction.

Zusammenfassung in Deutscher Sprache

In vielen ingenieurwissenschaftlichen und medizinischen Anwendungen treten Strömungen auf. Von besonderem Interesse sind dabei dynamische Größen, insbesondere Kräfte, die ein strömendes viskoses Fluid auf seine Umgebung ausübt. Nach dem allgemein akzeptierten Strömungsmodell lassen sich diese dynamischen Größen durch Ableitungen des Geschwindigkeitsfeldes ausdrücken.

Mit Varianten der Magnetresonanztomographie können sowohl morphologische als auch Geschwindigkeitsdaten im Inneren eines Körpers erfasst werden. Als nichtinvasive Methode ist sie besonders für *in vivo* Untersuchungen des kardiovaskulären Systems geeignet.

In dieser Arbeit beschäftigen wir uns mit der Bestimmung der Wandschubspannung, der Verteilung der Scherkräfte, die die Blutströmung auf die Aortenwand ausübt. Dazu muss aus den Magnetresonanzdaten die Strömungsgeometrie sowie das Geschwindigkeitsfeld bestimmt und anschließend dessen Normalableitung, die Schergeschwindigkeit, ausgewertet werden. Auf den ersten Blick mag diese Aufgabe trivial erscheinen, allerdings erschweren einige Probleme ihre Lösung:

- Die Magnetresonanztomographie misst lokale Mittel der Strömungsgeschwindigkeit mit vergleichsweise niedriger Auflösung. Zusätzlich sind die Messungen verrauscht.
- Die Blutströmungen bilden Grenzschichten aus, in welchen sich das Strömungsfeld stark verändert. Dies erschwert die akkurate Approximation des Geschwindigkeitsfeldes gerade im Wandbereich.
- Es besteht eine strukturelle Verbindung zwischen Strömungsgeschwindigkeit und Strömungsgeometrie: An der Wand besitzt gerade die auszuwertende Schergeschwindigkeit eine Unstetigkeit.

Im ersten Teil dieser Arbeit stellen wir ein Framework zur rein datenbasierten Berechnung der Wandschubspannung vor. Dabei werden zunächst die Strömungsgeometrie und anschließend die Strömungsgeschwindigkeit durch Parametrisierungen approximiert. Im Kontinuierlichen lässt sich die Rekonstruktionsmethode als Regularisierungsverfahren zweier gekoppelter inverser Probleme analysieren. Die zugehörigen Vorwärtsoperatoren erfüllen eine bedingte Stabilitätsabschätzung, womit die Konvergenz des Rekonstruktionsverfahrens unter akzeptablen Glattheitsvoraussetzungen an Geometrie und Strömung nachgewiesen werden kann. Diese Resultate lassen sich weitgehend in den diskreten Fall übertragen, wobei zur Minimierung des Datenfehlers diskrete Vorwärtsoperatoren eingeführt werden.

Im zweiten Teil der Arbeit nutzen wir Methoden der Datenassimilation, um mithilfe eines Strömungsmodells die rein datenbasierte Rekonstruktion zu verbessern. Einerseits greifen

wir dafür auf einen in der Arbeitsgruppe entwickelten Variationszugang zur Geschwindigkeitsrekonstruktion unter bekannter Geometrie zurück, der ein aus Datenfehler und Modellfehler bestehendes Zielfunktional minimiert. Formal entspricht dieses Verfahren einem Optimalsteuerungsproblem. Andererseits demonstrieren wir die prinzipielle Möglichkeit, die Geometrierekonstruktion mit einem Strömungsmodell zu verbessern. In beiden Fällen nutzen wir die weitgehend akkuraten datenbasierten Rekonstruktionen zur Linearisierung und Lokalisierung des eingesetzten Strömungsmodells.

Die theoretischen Aussagen wurden in Kooperation mit Experten vom Fachgebiet für Strömungslehre und Aerodynamik der Technischen Universität Darmstadt und des Fachbereichs Radiologie und Medizinphysik des Universitätsklinikums Freiburg umfangreich validiert. Eine große Schwierigkeit ist der Mangel an Referenzwerten. Die Wandschubspannung reagiert sehr sensibel auf Störungen der Umgebungsbedingungen. Deshalb mussten die Experimente mit akribischer Genauigkeit durchgeführt werden, um Reproduzierbarkeit und damit die Aussagekraft der durch hochauflösende Laser-Doppler-Anemometrie sowie Computersimulationen erhaltenen Referenzwerte sicherzustellen. Zusätzlich wurden besonders stabile, aber auf bestimmte Strömungen spezialisierte Verfahren entwickelt, um die Wandschubspannung mit hoher Genauigkeit auch aus den Magnetresonanzdaten zu bestimmen. Weiterhin wird in einigen Fällen auf virtuelle *in silico* Daten zurückgegriffen.

Bereits die rein datenbasierte Methode liefert weitgehend überzeugende Resultate. Allerdings ist die Rekonstruktion sehr sensibel bezüglich Fehlern in der Geometrieerkennung und zeigt in einigen Fällen durch die grobe Auflösung verursachte systematische Störungen. Unsere Analyse identifiziert die Fehlerquellen und ihren Beitrag zum Rekonstruktionsfehler. Dies liefert wichtige Hinweise für eine geeignete Wahl der Messparameter. Weiterhin lassen sich die beschriebenen Schwachstellen der rein datenbasierten Rekonstruktion durch die vorgestellten Datenassimilationsmethoden substantiell verbessern. Die Spezialisierung unseres Rekonstruktionsframeworks auf die Anwendung in der Aorta führt zu einem niedrigen Rechenaufwand, typische Rechenzeiten für alle vorgestellten Methoden liegen im Bereich von wenigen Minuten auf gewöhnlicher Hardware. Damit ist auch unter den Limitierungen der klinischen Routine eine valide Schätzung der Wandschubspannung möglich.

Diese Arbeit wurde durch das DFG Projekt EG-331/1-1 finanziert. In dessen Rahmen entstanden in Zusammenarbeit mit den Projektpartnern die folgenden Arbeiten:

- H. Egger and G. Teschner. On the Stable Estimation of Flow Geometry and Wall Shear Stress from Magnetic Resonance Images. *Inverse Problems*, 35:095001, 2019.

- A. Bauer, S. Wegt, M. Bopp, S. Jakirlic, C. Tropea, A. J. Krafft, N. Shokina, J. Hennig, G. Teschner and H. Egger. Comparison of Wall Shear Stress Estimates Obtained by Laser Doppler Velocimetry, Magnetic Resonance Imaging and Numerical Simulations. *Experiments in Fluids*, 60:1–16, 2019.

- N. Shokina, A. Bauer, G. Teschner, W. B. Buchenberg, C. Tropea, H. Egger, J. Hennig and A. J. Krafft. MR-based Wall Shear Stress Measurements in Fully Developed Turbulent Flow using the Clauser Plot Method. *Journal of Magnetic Resonance*, 305:16–21, 2019.

- N. Shokina, G. Teschner, A. Bauer, C. Tropea, H. Egger, J. Hennig and A. J. Krafft. Quantification of Wall Shear Stress in Large Blood Vessels using Magnetic Resonance Imaging. *Computational Technologies*, 24:4–27, 2019.

- N. Shokina, G. Teschner, A. Bauer, C. Tropea, H. Egger, J. Hennig and A. J. Krafft. Parametric Sequential Method for MRI-based Wall Shear Stress Quantification. *IEEE Transactions on Medical Imaging*, 40:1105–1112, 2020.

Wir fassen die in den obigen Arbeiten gewonnen Resultate in dieser Dissertationsschrift zusammen und ergänzen sie an geeigneter Stelle zu einer vollständigen Analyse der Rekonstruktion der Wandschubspannung.

Acknowledgements

First of all, I would like to thank Dr. Nina Shokina and my supervisor Prof. Dr. Herbert Egger for the fruitful collaboration and their constant support. Also, I would like to thank the further project collaborators Dr. Andreas Bauer, Prof. Dr.-Ing. Cameron Tropea and Apl. Prof. Dr.-Ing. habil. Suad Jakirlic as well as Dr. Axel Krafft and Prof. Dr. Dr. h.c. Jürgen Hennig. I am very grateful to Prof. Dr. Jan-Frederik Pietschmann for reviewing this dissertation.

Second, let me express a special thanks to my colleagues Moritz, Bogdan, Elisa und Nora for providing me a pleasant atmosphere and the good mixture of mathematical discussions and relaxed moments.

Schließlich möchte ich mich noch bei meiner Familie und meinen Freunden - speziell Esther, Olivia, Veronika, Judith und Stephan - bedanken, die mich über die vergangenen Jahre neben der Arbeit - die mich ja auch nie ganz in Ruhe gelassen hat - begleitet haben. Gerade mit Beginn der Pandemie und in der sehr nervenaufreibenden Schlussphase der Arbeit habe ich mich von Euch sehr unterstützt gefühlt.

The experimental data were provided by the Medical Physics group at the University Medical Center in Freiburg and by the Institute for Fluid Mechanics and Aerodynamics at the Technical University Darmstadt.

The German Research Foundation (DFG) supported this work via grant EG-331/1-1.

Contents

Chapter 1

Introduction

1.1 Motivation for the Estimation of Wall Shear Stress

Cardiovascular diseases are a leading cause of death [75]. The asymptomatic development followed by a sudden occurance of life-threatening events that are typical for cardiovascular diseases, pose a major challenge to modern medicine. Hence, identification of risk factors and staging of diagnosted cardiovascular diseases that appear stable become important [35].

Phase contrast magnetic resonance imaging offers the unique opportunity for non-invasive investigation of the cardiovascular system in acceptable measurement times [63]. It is a multimodal imaging technique, providing both morphological data, containing information about the tissue, and velocity data in a single measurement. For illustration, in Figures 1.1 and 1.2 we present measurements in a two-dimensional cross section of the ascending aorta in the phase of peak systole, i.e. maximum volume flow, of the cardiac cycle. Other imaging techniques provide only one modality, like the morphological data from computed tomography or the velocity data from transcranial Doppler ultrasound. Additionally, these methods suffer from drawbacks like considerable radiation exposure or difficult positioning of the transducer [80], making them inappropriate for regular monitoring of a detected cardiovascular disease. In the last 40 years, magnetic resonance imaging underwent further enhancements: Triggered by an electrocardiogram, cine magnetic resonance imaging allows for spatiotemporally resolved measurements of the periodic evolution of an object in a three-dimensional cubic domain [59].

Given the ability of magnetic resonance imaging, one uses different observable quantities, like vessel diameter, aspect ratios, flow rates or peak flow velocities, for the staging of cardiovascular diseases. Although this is the current procedure in the medical practice, different studies revealed a poor correlation between these basic quantities and the risk of the sudden occurance of severe complications. For example, one observes no significant differences in the aspect ratios between ruptured and unruptured cerebral aneurysms [83]. Regarding aortic valve stenosis, one finds a considerable number of cases with several indicators for the severeness of the disease in discordance [35]. Consequently, these simple quantities, that are accessible from the magnetic resonance data with high accuracy and under negligable computational effort, do not allow for an enhanced staging of cardiovascular diseases.

Following a commonly accepted paradigm [38], the forces, that the blood flow exerts on

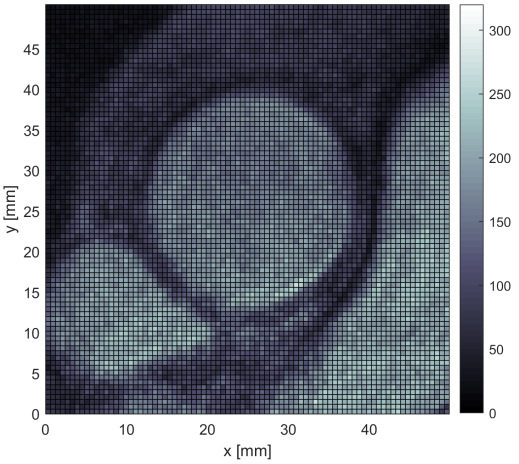

Figure 1.1: Morphological data of the ascending human aorta (circle in the center) at peak systole with surrounding tissue.

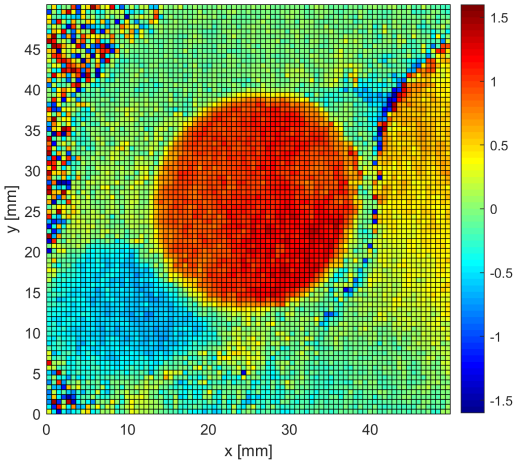

Figure 1.2: Velocity data of the ascending human aorta at peak systole; velocity in [m/s].

the vessel wall, play a key role in the development of endothelial cells, i.e. the inner layer of cells in the vessel wall, and consequently the disease. The forces the blood flow exerts on the boundary are normal forces, i.e. the static and dynamic pressure, and shear forces in tangential direction, i.e. the wall shear stress.

Regarding the blood pressure, the most prominent example is the hypertension: long-term increased blood pressure may trigger several cardiocascular diseases and is, therefore, treated with medical drugs [87]. In addition, the velocity of the pressure wave through the cardiovascular system, caused by the heart contraction, is measured as indicator for arterial stiffness [99].

Various studies have shown that especially the wall shear stress renders a precise indicator for the severeness of various diseases. Amongst other, we mention the correlation of wall shear stress with the risk of rapture or dissection of aneurysms [83], the development of arteriosclerosis [82], arterial stenosis [95] and bicuspid aortic valve, a significant risk factor for general aortic diseases [4, 5]. The importance of wall shear stress is highlighted as well in several review articles [50, 72, 85].

Beside its use in the medical practice, magnetic resonance imaging has gained attraction in industrial applications, due to its capability of non-invasive volumetric flow measurements within reasonable data acquisition times [16, 34]. In this context, the method is typically referred to as magnetic resonance velocimetry. Thus, the presented work provides a specialized framework for the aortic flow regime, it might also be of interest for industrial applications. In particular we mention the frequently considered phenomenon of flow separation, that is characterized by a change of sign of the wall shear stress. For this accurate wall shear stress estimates are required.

1.2 Definition of Wall Shear Stress

The wall shear stress τ is the surface shear force density, that a viscous fluid applies on the boundary. Under some reasonable assumptions, the wall shear stress is accessible from the flow geometry and the flow velocity. We briefly present this representation and the required conditions, a detailed description can be found in the standard literature [79].

According to Newton's third law of motion, the force density applied to the boundary corresponds to the negative internal force density at the boundary transported in normal direction n. The latter is given by the fluid stress vector σn, where the stress tensor σ itself consists of two components

$$\sigma = f(E) + pI. \tag{1.1}$$

The second term is the normal stress generated by the pressure p. The first term is the viscous stress, which is characteristic for viscous fluids and generated by differences of the velocity field u. The concrete source E for these viscous stresses is the strain rate tensor

$$E = Eu = \frac{1}{2}\left(Du + (Du)^T\right). \tag{1.2}$$

Now, we make a fundamental assumption on the considered fluid:

Assumption 1.1. *Let the flow consist of an incompressible Newtonian fluid, satisfying the no-slip boundary condition, i.e. the fluid sticks on the wall. Finally, assume the wall to be smooth and non-moving in time.*

Since the fluid is Newtonian, we have $f(E) = 2\mu E$, where $\mu > 0$ is the fluid specific dynamic viscosity. W.l.o.g assume, that the normal direction coincides with the first coordinate. Then we have by the no-slip condition and the smoothness of the boundary for the tangential velocity derivatives

$$\partial_2 u = \partial_3 u = 0.$$

For an incompressible fluid, we further obtain

$$\partial_1 u_1 = \operatorname{div}(u) - \partial_2 u_2 - \partial_3 u_3 = 0.$$

Thus, the fluid stress vector simplifies to

$$\sigma n = \mu \partial_n u + \mu \nabla u_n + pn = \mu \partial_n u + pn.$$

The wall shear stress is the projection into the tangential space and, since $\partial_n u_n = 0$, we have

$$\tau = -\mu\, \partial_n u. \tag{1.3}$$

Given the dynamic viscosity μ, the estimation of wall shear stress from magnetic resonance imaging reduces to the problem of computing the normal derivative of the velocity field at the vessel boundary from the morphological data that contains the information about the geometry, and the velocity data. Although this problem appears very basic, there are several complicating issues, as we will outline in the following section.

1.3 Challenges and Existing Approaches for Wall Shear Stress Estimation

The most conspicuous issue for computing an accurate wall shear stress estimate is the complexity of the velocity profile. As depicted in Figure 1.2, the velocity exhibits boundary layers. Starting from a vanishing velocity at the boundary due to the no-slip condition, the flow velocity increases to the free-stream velocity at considerably small distances from the boundary. Outside the boundary layer, the velocity profile is rather constant.

Secondly, the magnetic resonance imaging data are affected by noise. This holds in particular at the boundary, where partial volume effects occur [3]. The region near to the vessel wall exhibits low velocities, leading additionally to a reduced signal due to magnetic saturation [26]. Unfortunately, this leads to the situation, that the region, which is most important for the wall shear stress estimation, contains highly noisy data.

Another frequently mentioned issue is the low data resolution [69]. This is related to a more severe problem, that also occurs for higher resolutions: the measurement operator contains a filtering process and although the velocity data in Figure 1.2 optically appears complete, these data are just sparse samples of an infinitely dimensional quantity.

In the end, there are some secondary issues affecting the design of wall shear stress estimators. On the one hand, we have to deal with the lack of *ground truth*: the complexity of the physiological blood flow with Reynolds numbers $\mathrm{Re} \approx 4000 - 8000$ [8], the individual geometry, the interaction with the surrounding tissue with even more complex cellular structure [46] and the blood rheology [47] are beyond the limitations of a direct numerical simulation or a highly resolved experimental study. Hence, there is no available gold standard for an overall validation, there can only be limited validation. On the other hand, the application of the estimator in the medical context poses some limitations on the data acquisition and the computational effort.

For the existing wall shear stress estimators, we distinguish among three different paradigms that have their inidividual advantages and drawbacks. Note that a reconstruction of the flow geometry is relatively easily obtained by standard methods [22] and the estimators focus on reconstructing the velocity profile. However, one should keep in mind, that only an approximation of the geometry is accessible.

The data based approach. Data based wall shear stress estimators aim for approximating the wall shear rate $\partial_n u$ directly from the magnetic resonance imaging data. Usually, they require an *a priori* given geometry identification. Furthermore, they are substantially affected by the aforementioned issues: since no generally applicable theory about the shape of the velocity profile in the boundary layer is known, generic approximation schemes are required. Due to the formation of the boundary layer, high order derivatives of the velocity profile, such as the curvature, exhibit large values, leading to large discretization errors at the application of generic approximation schemes [21]. The combination of noisy data with the reconstruction from sparse measurements leads to an ill-posed problem [28]. Finally, even in the case of available exact velocity data, the wall shear rate decreases rapidly while

going to the interior of the flow domain and is constant zero outside the flow domain, since the flow velocity vanishes there. Hence, only a slight overestimation or a moderate underestimation of the geometry would lead to a vanishing or nearly vanishing shear rate. Therefore, a straightforward separate reconstruction of the ingredients, the geometry and the velocity, leads to a non-robust estimate.

In an extensive study, existing data based wall shear stress estimators were found to systematically underestimate the wall shear stress, making Petersson et al. [69] conclude that

> *"Even in the absence of noise and for relatively simple velocity profiles, all methods evaluated were found to be impacted by considerable errors depending on parameter settings such as VENC, velocity resolution, and especially spatial resolution."*

However, the striking advantage of these data driven methods is their computational simplicity. Typical processing times are in the range of several seconds. Despite their inaccuracy, they are found to be monotonic, i.e. regions of higher wall shear stress were reproduced. These advantages make them currently a standard procedure in medical practice [94]. There are several techniques [67, 68, 70, 73, 88], which we will characterize in Subsection 2.1.2.

The model based approach. On the other hand, model driven approaches use computational fluid dynamics to calculate the flow velocity and subsequently the wall shear stress. The methodology is to identify the geometry from the measurement data and to perform a flow simulation, where a data driven velocity reconstruction is used as boundary data [2]. The aforementioned issues affect the methods in another way; the complexity of the flow requires a highly resolved computational mesh for the simulation that tracks all important features of the flow. Furthermore, there arise difficulties with the model: usually, blood is modelled as a Newtonian fluid. Although in general blood is a shear thinning Non-Newtonian fluid [47], there is justification for the Newtonian idealization in aortic flow regimes [17]. Apart from the blood rheology, an appropriate turbulence model should be taken into account, since there is some evidence that the blood flow might be turbulent [89] and as mentioned above, the problem is out of range of a direct numerical simulation.

Since the available velocity data are filtered and microscales of the flow unresolved, they are only of limited use for the simulation. However, boundary conditions have to be defined and, in particular, the inlet conditions are of crucial impact for the result [90]. A remedy is to simulate in a domain containing a large section upstream the region of interest. For instance, this might lead up to a electro-mechano-fluidic model of the left ventricle of the heart and the aorta, a fully integrated simulation of the electrochemical stimulation, the contraction of the heart muscle and the induced blood flow in the cardiac system [51]. These methods are believed to be accurate and inherit the sensitivity for mismatches of the geometry from the physical sensitivity for changes of the geometry. On the other hand, they pose a huge computational effort and make only little use of the acquired velocity measurements.

To exploit the acquired measurements in a model based approach, data assimilation techniques has been applied to the reconstruction of the velocity field [54,58]. These methods formulate the reconstruction as an optimal boundary control problem governed by a fluid dynamical model, utilizing the volumetric velocity data to find an enhanced boundary value using a tracking type functional. Although these methods may be applicable to smaller computational domains, they remain costly, since several solutions of the non-stationary non-linear state equation are required for the solution of the optimal control problem. Another data assimilation method uses the given velocity data to linearize the flow model [24], making it substantially less expensive, but relying on high data accuracy.

Specialized approach. Beside these generic wall shear stress estimators that are in principal applicable to all flows, there are specialized wall shear stress estimators, whose applicability is restricted to particular flow regimes. These estimators have in common that they use knowledge about the flow regime to reduce the dimensionality of the unknown velocity profile. Hence, the original problem of recovering a high dimensional state from sparse data turns into the problem of recovering low dimensional data from high dimensional measurements. Thus, the aforementioned issues are negligable. The most prominent example in the investigation of blood flow is the method of Womersley [98]. Originally designed for a straight pipe, it considers a periodic laminar flow in a generalized cylinder $\Omega = \Omega_2 \times (0, 1)$. For simple shapes of the cross section Ω_2, the flow governing equations exhibit a unique analytical solution, depending only on the temporal evolution of the volume flow rate. For more complex geometries, there are fast and accurate numerical methods to compute the velocity profile from the volume flow rate. A second example for a specialized wall shear stress estimator is the Clauser method [20]. It is based on the logarithmic law of the wall [79] - an experimental correlation - that represents the velocity profile in the boundary layer by only one unknown. Hence, fitting this friction factor velocity to the data unlocks access to the entire velocity profile in the boundary layer and, thus, the wall shear stress.

1.4 Methodology

Before touching upon the essential concepts, we formulate the main goal of this work.

Problem 1.2. *Let the morphological data $\overline{m}^\delta$ and the velocity data u^ε be given from magnetic resonance imaging. Compute estimates $\Gamma^{\delta,\varepsilon} \subset \mathbb{R}^3$ and*

$$\tau^{\delta,\varepsilon} : \Gamma^{\delta,\varepsilon} \to \mathbb{R}^3$$

on the boundary of the flow geometry and the wall shear stress, respectively.

For simplification of the study, we make several assumptions. Apart from some reasonable technical assumptions, that will be mentioned in due course, they concern the following major points.

- **Geometry:** we consider a nearly circular (2D) or tubular (3D) stationary geometry.

- **Fluid:** we consider an incompressible Newtonian fluid flow satisfying the no-slip condition. In particular, Assumption 1.1 is valid.

- **Flow and measurement:** we consider measurements of flows that share important properties like the Reynolds number and the presence of boundary layers with typical flow regimes present in the human aorta. Important measurement conditions like resolution and noise level are realistic for *in vivo* investigations. The data acquisition times are short compared to changes of the flow, such that we can treat the data as snapshots of a possibly instationary flow.

Due to their limited applicability and high computational effort, we discard specialized and model based approaches and develop a data based estimation framework. However, specialized wall shear stress estimators play a key role in the validation and some model based concepts are utilized to enhance the initially purely data driven reconstruction method. The overall strategy becomes apparent, when we consider the organization of the work subsequently to this introductory first chapter.

In Chapter 2, we develop a new purely data driven reconstruction method that sequentially computes approximations of the flow geometry, the flow velocity, and finally the wall shear stress from the magnetic resonance imaging data. To ensure a mathematically sound design of the method, we analyze it with tools of the investigation of inverse problems, yielding convergence rates of the reconstruction in terms of the data error. In particular, the method is robust against small errors of the flow geometry reconstruction. This chapter is based on our publication [25].

Chapter 3 is dedicated to the validation of the data driven reconstruction method. First, we present an enhanced model for the discrete measurement data and discuss the discretization of the method that matches the data model and maintains the advantage of low computational complexity. For validation, we apply the method to several flows that share important features, like the Reynolds number and the formation of a boundary layer with physiological flows in the human aorta and for which highly accurate reference values for the wall shear stress are accessible. By comparison with the reference data, we detect the capabilities and issues of the method. The chapter is rounded off with illustrative applications to more complex simulated and physiological flows. This chapter is based on our publication [86].

In Chapter 4, we discuss the possibility of resolving some of the detected problems of the data based reconstruction method by the appropriate incorporation of fluid dynamical models. From a practical viewpoint, the developed methods differ significantly from the aforementioned model based wall shear stress estimators: on the one hand, the computational complexity of the proposed methods remains manageable. On the other hand, our strategies make a higher use of and put higher trust in the data. This chapter is partly motivated by preliminary work in our group [24, 81], but important results are so far unpublished.

Chapter 5 finally refers back to Problem 1.2 and summarizes, how far the proposed methods resolve it.

Our reconstruction concept was developed based on several preliminary studies of our research collaboration with experts in medical imaging and both experimental and numerical fluid dynamics. Carefully conducted experiments revealed the high sensitivity of the wall shear stress on changes of various external parameters like the temperature distribution and the high accuracy of the laminar Womersley solution for physiologically pulsating flows. Furthermore, by making use of the known flow geometry in the experiment and extensive averaging, we discovered the principal capability of magnetic resonance imaging to track important flow features [7,8] that motivates the data driven paradigm of this work. Regarding the validation, we developed a wall shear stress estimator for fully developed shear flows based on the Clauser method that computes highly accurate reference values from magnetic resonance data [84, 85].

To conclude this introduction, let us emphasize that in particular, the data driven approach with a mathematically sound reconstruction method as kernel and the extensive validation, set this work apart from existing investigations on similar subjects. In comparison with our publications [8, 25, 84–86], this thesis additionally includes

- the generalization of the conditional stability analysis to regularization with seminorms,
- the extension to 3D applications,
- the application of the conditional stability analysis to the discrete numerical solutions, and
- the development of enhancement strategies using a localized and linearized flow model.

Chapter 2

Data Driven Wall Shear Stress Reconstruction

This chapter is dedicated to the stable estimation of wall shear stress from magnetic resonance data. As presented in the introduction, the wall shear stress is defined at the boundary and represented in terms of the flow geometry and the flow velocity. For its estimation, we consider the following sequential strategy:

(i) reconstruction of the geometry Ω from magnetic resonance density data,

(ii) approximation of the velocity u from magnetic resonance velocity data,

(iii) estimation of wall shear stress $\tau : \partial\Omega \to \mathbb{R}^d$ from the geometry reconstruction and the velocity approximation using

$$\tau \;=\; -\,\mu\,\partial_n u, \tag{2.1}$$

where μ is the dynamic viscosity and n the outer normal.

We will see that, especially the first two steps, i.e. the geometry reconstruction and the velocity approximation, are ill-posed problems. Thus, regularization techniques are required for their stable solution. Since the topology of the flow domain is already known and a coarse approximation easily obtainable, we utilize a parametric representation of the geometry.

A technical difficulty for the analysis of the investigated problems arises from the non-differentiability of the forward operator that models the measurement process. Hence, standard results for the analysis of non-linear ill-posed problems are not directly applicable. Therefore, we utilize *conditional stability estimates* for the analysis of the regularization process: An extension of the basic results from Cheng and Yamamoto [19] allows for an entire analysis of the regularized solutions of the sub-problems, including modelling and discretization errors.

In Section 2.1, we discuss methods for the geometry reconstruction and the velocity approximation and motivate our proposed strategy. In Section 2.2, we present abstract results for the stable solution of ill-posed problems using Tikhonov regularization, in particular we derive a convergence result under *conditional stability estimates*. The parametric

representation of flow domains with a suited topology is presented in Section 2.3; furthermore we provide some important technical results for the subsequent analysis. The main results of this chapter are presented in Section 2.4: We consider the separate sub-problems listed above, cast them in the presented framework of ill-posed problems by introducing the measurement operator and analyze their basic properties. Then, we apply the convergence analysis of Section 2.2 to prove stability and convergence of solutions obtained by Tikhonov regularization. Finally, we combine the results to analyze the whole reconstruction process, yielding quantitative bonds for the error of the estimated wall shear stress in terms of the measurement errors.

For our theoretical considerations, we pose simplifying assumptions on the measurement operators. A more detailed measurement model, including some details of practical relevance, is presented alongside the numerical realization in Chapter 3. The analytical results presented in this chapter are based on our publication [25] and extended here in two directions: On the one hand, the results are extended to 3D, which causes complications in the parametric representation. Furthermore, we utilize the seminorm for the Tikhonov regularization.

2.1 Existing Approaches and Mathematical Challenges

In this section, we briefly comment on existing data driven approaches for the estimation of wall shear stress with respect to its two ingredients, the flow geometry and velocity. Finally, we sketch our approach.

2.1.1 Geometry Reconstruction

The precise localization of the flow domain Ω is of course an important ingredient for the wall shear stress estimation. We assume, that magnetic resonance density data are available on the measurement domain $\Omega_{\mathrm{FOV}} \supset \Omega$, i.e. the *field of view*, like the data depicted in Figure 1.1. In this chapter, we assume that these density or magnitude data m^δ are

$$m^\delta \;=\; \chi_\Omega + \nu^\delta \text{ in } \Omega_{\mathrm{FOV}} \tag{2.2}$$

where $\nu^\delta : \Omega_{\mathrm{FOV}} \to \mathbb{R}$ denotes some noise. Let us briefly discuss two widely used approaches for geometry representation and estimation:

- the implicit representation using a *level set function* and
- the explicit representation using a parameterization.

The more flexible approach is the representation by a scalar *level set function* ϕ [66] with the property

$$\phi(x) \begin{cases} > 0 & \text{for } x \in \Omega, \\ = 0 & \text{for } x \in \partial\Omega, \\ < 0 & \text{for } x \notin \overline{\Omega}. \end{cases}$$

A smooth *level set function* provides access to several associated geometric quantities such as the boundary, implicitly given by $\partial\Omega = \{x \mid \phi(x) = 0\}$, with the outer normal $n = -\nabla\phi/|\nabla\phi|$. This representation is not restricted to domains Ω of a specific topology, making the method very flexible.

The automatic computation of a *level set function* is a standard problem of image processing. A prominent example is the method of Mumford and Shah [62]. The geometry reconstruction leads to the problem [92]

$$\min_{\phi} \left\|\phi - (2m^{\delta} - 1)\right\|^2_{L^2(\Omega_{\mathrm{FOV}})} + \alpha\|\nabla\phi\|_{L^1(\Omega_{\mathrm{FOV}})}. \tag{2.3}$$

The second term leads to a denoising of the *level set function*, but allows for steep gradients at the boundary in contrast to a L^2 regularization of the gradient. This gives good results in practice, but leads to non-linear optimality systems and impedes Hilbert space techniques.

On the other hand, there is a parametric representation, specifying the boundary $\partial\Omega$ by a function $\Gamma : D \to \mathbb{R}^d$ given on a parameter domain $D \subset \mathbb{R}^{d-1}$

$$\partial\Omega = \Gamma(D).$$

By specifying the inner and outer side of $\partial\Omega$, this determines the domain Ω. By differentiation of the parameterization, an explicit representation of the outer normal is obtained as well. Contrary to the *level set method*, this parametric description requires Ω to be of a specific topology. On the other hand, the domain D is of lower dimension than Ω_{FOV} and usually requires less computional effort.

In the medical practive, the flow geometry Ω is usually parametrized and the parametrization reconstructed by a manual segmentation [67, 88]. However, an automatic representation is possible as well. Transferring the technique of Mumford and Shah to the parametric representation leads to a problem of the type

$$\min_{\Gamma} \left\|m(\Gamma) - m^{\delta}\right\|^2_{L^2(\Omega_{\mathrm{FOV}})} + \alpha\|\nabla\Gamma\|_{L^2(D)}.$$

We have to include an appropriate measurement operator m, that generates for given parameter Γ the corresponding magnitude data. In contrast to (2.3) a Hilbert space formulation is possible, since smoothness of the boundary corresponds to smoothness of the parametrization.

As aforementioned, the topology of our geometry is known and hence a parametric approach appears naturally. However, as we will outline in this chapter, the accuracy of the reconstruction is crucial. Therefore, we follow the last approach, an automatized reconstruction of a geometry parameter, that takes the details of the data into account.

2.1.2 Velocity Approximation and Wall Shear Stress Estimation

Alongside with the capability of conducting phase contrast magnetic resonance measurements in vivo and the discovery of wall shear stress as an important biomarker in the

1990s, the development of estimators for the wall shear stress $\tau = -\mu\partial_n u$ became the subject of current research. These estimators aim at approximating $\partial_n u$ from approximations of the geometry, its outer normal and the velocity. The latter is computed from magnetic resonance velocity data u^ε and we assume in this chapter

$$u^\varepsilon \;=\; u \,+\, \nu^\varepsilon \text{ in } \Omega_{\mathrm{FOV}} \tag{2.4}$$

where u is the flow velocity inside the flow domain Ω and vanishes outside and $\nu^\varepsilon : \Omega_{\mathrm{FOV}} \to \mathbb{R}^d$ denotes some noise

Early approaches use a polynomial ansatz to compute a local approximation of the velocity at the boundary. The estimator proposed in [67], for instance, approximates the wall shear rate $\partial_n u$ by

$$(\partial_n u)_{\varepsilon,h}(x) \;=\; \frac{1}{h}\, u^\varepsilon(x - hn(x)), \tag{2.5}$$

where the boundary positions x and the outer normal n are given from an *a priori* specified (usually by hand) geometry reconstruction and h denotes the data resolution. This method is based on a linear interpolation of the velocity, where the *no-slip* condition $u = 0$ at the boundary is incorporated. A modification [68] uses a quadratic ansatz to compute a local approximation of the velocity. Instead of enforcing $u = 0$ at the boundary, only data are incorporated for the interpolation and the boundary is repositioned to the next zero of the approximate velocity profile. The concept of local approximations of the velocity remains popular, recently developed methods [70,73] approximate the velocity profile on an inward normal line. They utilize a fixed *a priori* given geometry reconstruction. To avoid incorporating data outside the flow domain, the data, that is utilized in the reconstruction of the velocity profile, lies further in the interior beyond a certain safety region at the wall.

From a mathematical point of view, these methods provide reasonable approximations of the wall shear rate $\partial_n u$, but rely on sufficiently high data resolution. In particular for boundary layers, the incorporated interior data has to track the characteristic behaviour inside the boundary layer. Furthermore, these methods require the user to provide *a priori* geometry information and choose various method parameter by hand. Automatically tuning these method parameters seems difficult: For instance the parameters of the method [73] were tuned to find the best approximation of a quadratic Hagen-Pouseuille flow. The optimal reconstruction was found utilizing only three widely spaced data points. Although this produces a very stable estimator of Hagen-Poiseuille flows, it is not possible to compute reasonable wall shear rate approximations and consequently wall shear stress for physiological flows with boundary layers.

Data driven wall shear stress estimators underwent a change of paradigm, replacing local approximations of the velocity, that are controlled by complex parameter setups, with a user-friendly global approximation of the velocity in the kernel of the wall shear stress estimator. The prototype of this modern wall shear stress estimators is the method of Stalder et al. [88]. Here, the velocity is approximated by

$$u_{\varepsilon,h} \;=\; I_h(u^\varepsilon * G_\gamma), \tag{2.6}$$

where G_γ is a Gaussian smoothing kernel of bandwidth $\gamma = 1\text{mm}$, h is the data resolution and I_h the cubic spline interpolation on a regular grid with spacing h. The wall shear stress is estimated from the wall shear rate approximation $(\partial_n u)_{\varepsilon,h}$ and the boundary $\partial\Omega$, whose location has to be specified by the user. Note that the velocity approximation is computed without knowledge about the flow geometry. Numerous similar methods were developed and used for various studies, see for instance [53, 100].

Although computing a global approximation of the velocity seems straighforward, there is a major mathematical issue: Outside the flow domain, the velocity is constant zero, resulting in a kink of the measured velocity field u at the boundary $\partial\Omega$. This amounts to a discontinuity of the wall shear rate $\partial_n u$ for fixed normal direction n. Hence, the global velocity is non-smooth. This obviously makes estimation of $\partial_n u$ difficult. Also for an applicable exact velocity, the estimate is not stable with respect to errors of the reconstructed geometry.

2.1.3 Sketch of the Data Driven Reconstruction Method

The proposed reconstruction method consists of three steps, the geometry reconstruction, the velocity approximation and finally the wall shear stress estimation.

Geometry reconstruction. We use a parametric representation of the geometry $\Omega = \Omega(R)$ with $R \in \mathcal{G}$, where R is the geometry parameter and $\mathcal{G} \subset H^k(D)$ the set of admissible geometries with a simple parameter domain D. The parametrization is introduced in Section 2.3. Motivated from the measurement model (2.2), we introduce the parameter-to-measurement operator

$$F : \mathcal{G} \to L^2(\Omega_{\text{FOV}}), \quad R \mapsto \chi_{\Omega(R)} := \begin{cases} 1 & \text{in } \Omega(R), \\ 0 & \text{in } \Omega_{\text{FOV}} \setminus \Omega(R), \end{cases}$$

where χ is the characteristic function. The geometry reconstruction can then be cast as

$$\text{find } R^* \in \mathcal{G} \text{ with } F(R^*) = m^\delta, \tag{2.7}$$

which is a non-linear and ill-posed inverse problem. We will show, that this operator is only Hölder continuous, but not differentiable. As a consequence, standard regularization theory, that is presented in Subsection 2.2.2, is not directly applicable. Hence, an alternative approach is presented, that will provide stability and error bounds on the reconstructions.

Velocity approximation. After computing an approximation $\Omega = \Omega(R)$ of the geometry, we consider the problem of approximating the flow velocity. To obtain stability with respect to small geometry errors, we approximate the velocity, mapped to a simple reference domain $\widehat{\Omega} \subset \mathbb{R}^d$. For this purpose, we introduce a family of domain transformations, associating with any admissible geometry parameter $R \in \mathcal{G}$ a transformation $\Psi_R : \Omega(R) \to \widehat{\Omega}$. Then we introduce a set of admissible velocities on the reference domain $\mathcal{U} \subset H^k(\widehat{\Omega})$ and

the velocity measurement operator

$$T_R : \mathcal{U} \subset H^k(\hat{\Omega}) \to L^2(\Omega_{\mathrm{FOV}}), \quad Tv := E_R(v \circ \Psi_R), \tag{2.8}$$

where $E : L^2(\Omega(R)) \to L^2(\Omega_{\mathrm{FOV}})$ denotes the extension by zero. Note that the measurement operator depends on the geometry parameter R. With the reconstructed geometry parameter $R^* \in \mathcal{G}$, the velocity approximation problem reads:

$$\text{Find } v^* \in \mathcal{U} \text{ with } T_{R^*} v^* = u^\varepsilon. \tag{2.9}$$

This is a linear ill-posed problem, whose stable solution can in principle be analysed with standard regularization theory [29]. Note that we have for the range of the operator $\mathcal{R}(T_{R^*}) \subseteq L^2(\Omega(R^*))$ and consequently, only data in the interior of the flow domain are relevant for the velocity approximation. The stability with respect to the geometry parameter will be established by explicit estimates on the deviation between the corresponding operators $T_{R_1} - T_{R_2}$, that are presented in Subsection 2.4.2.

Wall shear stress estimation. For the wall shear stress estimation, we map the reconstructed velocity to the physical domain by $u^* = v^* \circ \Psi_{R^*}$. Then the consistent estimate reads

$$\tau^* = -\mu \, \partial_{n^*} u^*. \tag{2.10}$$

For the error analysis, we have to transform the wall shear stress to a reference domain for the boundary, which naturally coincides the parameter domain D. Based on the previously established error estimates for the constituants, we will arrive at a fully analyzed, convergent wall shear stress estimate.

Outlook. Before analyzing the sketched reconstruction technique in Section 2.4, we present a framework for the analysis of the arising ill-posed problems and introduce the parametric representation of the flow domain.

2.2 Inverse Problems

In this section, we discuss the stable solution of ill-posed non-linear problems in Hilbert spaces under *conditional stability estimates*. The results are derived on an abstract level here and they are later applied to the aforementioned geometry reconstruction and velocity approximation problems.

2.2.1 Ill-posed Problems

We consider inverse problems in Hilbert spaces of the following type:

$$\text{Find } x \in \mathcal{D}(F) \text{ with } F(x) = y^\delta. \tag{2.11}$$

Here, X and Y are Hilbert spaces for the parameter and the data, respectively. The measurement acquisition is modelled with a operator $F : \mathcal{D}(F) \subseteq X \to Y$, where $\mathcal{D}(F)$ is closed and convex. The available data $y^\delta \in Y$ is a noisy image of an exact solution $x^\dagger \in \mathcal{D}(F)$ and we assume, that an upper bound on the measurement error is available, i.e.

$$\|F(x^\dagger) - y^\delta\|_Y \leq \delta \text{ with } \delta > 0 \text{ known.} \tag{2.12}$$

Following Hadamard [42], the operator equation (2.11) is called well-posed at $x_0 \in \mathcal{D}(F)$, if there is a neighbourhood $B(y_0) \subset Y$ around $y_0 = F(x_0)$ with the properties:

- **Existence:** For all $y \in B(y_0)$, there exists a solution $x \in \mathcal{D}(F)$ of (2.11).
- **Uniqueness:** For all $y \in B(y_0)$, the solution $x \in \mathcal{D}(F)$ of (2.11) is unique.
- **Stability:** The inverse operator $F^{-1} : B(y_0) \to \mathcal{D}(F)$ is continuous at y_0.

Problems (2.11), that violate at least one of these conditions, are called *ill-posed*. Ill-posed problems typically arise from compact forward operators. Unfortunately, both the geometry reconstruction problem (2.7) and the velocity approximation problem (2.9) violate the stability condition and are therefore ill-posed.

The main challenge for the solution of ill-posed inverse problems (2.11) is to find a stable approximation of the original parameter $x^\dagger$ from the measured data y^δ under knowledge of δ, which can only be accomplised by so-called regularization techniques. One of the most popular approaches is Tikhonov regularization [97]. Spectral calculus allows for a rather comprehensive analysis of linear inverse problems using standard regularization techniques such as Tikhonov regularization or truncated singular value decomposition [28]. Alternative arguments are required for the analysis of non-linear inverse problems [28, Chapter 10] and briefly summarized in the following subsection.

2.2.2 Tikhonov Regularization for Non-linear Inverse Problems

For the stable solution of (2.11), we consider Tikhonov regularization

$$\min_{x \in \mathcal{D}(F)} \|F(x) - y^\delta\|_Y^2 + \alpha \|x - x^*\|_X^2, \tag{2.13}$$

where $\alpha > 0$ is a regularization parameter and $x^* \in X$ is an initial guess on the solution. By $x_\alpha^\delta \in \mathcal{D}(F)$ we denote an arbitrary minimizer of the Tikhonov functional (2.13). Using elementary arguments, one can prove the existence of Tikhonov minimizers under the conditions, that

$$F \text{ is continuous and weakly continuous,} \tag{2.14}$$

but uniqueness of Tikhonov minimizers can obviously not be guaranteed in general [9, Section 3]. To simplify the following discussion, we assume, that F is injective on $\mathcal{D}(F)$. Then one obtains the following convergence result [28, Theorem 10.3].

Proposition 2.1. *Let $x^\dagger \in \mathcal{D}(F)$. Let $y_k \to F(x^\dagger)$ in Y with $\|F(x^\dagger) - y^k\|_Y \leq \delta_k$. Set $\alpha_k = \alpha(\delta_k) = \delta_k$. Then we have for any sequence of associated Tikhonov minimizers $x_{\alpha_k}^{\delta_k}$ with y^δ replaced by y_k*

$$\lim_{k\to\infty} x_{\alpha_k}^{\delta_k} = x^\dagger \text{ in } X.$$

Note that the assertion holds independently of the choice of the possibly not unique Tikhonov minimizers x_α^δ. Under additional conditions, also quantitative convergence rates can be obtained [28, Theorem 10.4].

Proposition 2.2. *Let $x^\dagger \in \mathcal{D}(F)$. Let $y^\delta \in Y$ with $\|F(x^\dagger) - y^\delta\|_Y \leq \delta$. Further assume that*

(i) F is Frechet differentiable,

(ii) there is $L > 0$ with $\|F'(x^\dagger) - F'(x)\|_{\mathcal{L}(X;Y)} \leq L\|x^\dagger - x\|_X$ for all $x \in \mathcal{D}(F)$,

(iii) there is $w \in Y$ with $x^* - x^\dagger = F'(x^\dagger)^* w$,

(iv) it holds $L\|w\|_Y < 1$.

Then for $\alpha = \alpha(\delta) = \delta$ any Tikhonov minimizer x_α^δ satisfies

$$\|F(x_\alpha^\delta) - y\|_Y \leq C\delta \text{ and } \|x_\alpha^\delta - x^\dagger\|_X \leq C\sqrt{\delta}.$$

The first and second condition restrict the non-linear behavior of F. The two latter conditions are typically referred to as *source condition* and pose an abstract smoothness condition on the difference between solution and initial guess $x^\dagger - x^*$. There are investigations, that derive convergence rates under weaker smoothness assumptions on $x^\dagger - x^*$ than the previously assumed source condition. However, in this case abstract *non-linearity conditions* on the operator F are imposed [78], that are difficult to verify [49]. Due to the lack of differentiabilty, this standard approach is unfeasible for the investigation of the geometry reconstruction problem with non-differentiable forward operator.

An elegant alternative approach for the analysis of Tikhonov regularization for non-linear inverse problems was proposed by Cheng and Yamamoto [19]. Let us briefly discuss a simplified version of their approach in the current setting. Consider an additional Hilbert space $Z \subset X$ compactly embedded in X and define the forward operator $F : \mathcal{D}(F) \subset Z \to Y$, where

$$\mathcal{D}(F) = \{x \in Z \mid \|x\|_Z \leq M\}. \tag{2.15}$$

For the solution of $F(x) = y^\delta$ consider again the Tikhonov regularization

$$\min_{x\in\mathcal{D}(F)} \|F(x) - y^\delta\|_Y^2 + \alpha\|x\|_Z^2. \tag{2.16}$$

Existence of Tikhonov minimizers again follows from F continuous and weakly continuous. For the analysis, the authors of [19] require a *conditional stability estimate* of the form

$$\|x_1 - x_2\|_X \leq \omega(\|F(x_1) - F(x_2)\|_Y) \quad \forall x_1, x_2 \in \mathcal{D}(F). \tag{2.17}$$

Hence, we can bound the difference between two regular parameters x_1, x_2, where regularity refers to the affiliation to $\mathcal{D}(F)$, in terms of the distance between the associated data. Note that this condition inherently requires injectivity of F. Under these conditions, they proved the following result.

Proposition 2.3. *Let F with domain like in (2.15) allow for a conditional stability estimate (2.17). Let $x^\dagger \in \mathcal{D}(F)$ and $y^\delta \in Y$ with $\|F(x^\dagger) - y^\delta\|_Y \leq \delta$. Let $x_\alpha^\delta \in \mathcal{D}(F)$ be a minimizer of the Tikhonov functional (2.16) for $\alpha = \delta^2$. Then*

$$\|x_\alpha^\delta - x^\dagger\|_X \leq C\omega(\delta).$$

The conditional stability estimate replaces all non-linearity conditions on the operator in Proposition 2.2, while the source condition transforms to a workable smoothness condition $x^\dagger \in \mathcal{D}(F)$. In particular, the approach covers non-differentiable forward operators.

The stability function ω in (2.17) determines the convergence behaviour. Hölder-type stability $\omega(s) = Cs^\beta$ with $\beta \in (0, 1]$ and logarithmic-type stability $\omega(s) = -C/\log(s)$ are distinguished. For the former we obtain the convergence rates δ^β, while the logarithmic stability is the worse stability estimate resulting in a slow convergence. The stability is essentially affected from the choice of $\mathcal{D}(F)$. However, $\mathcal{D}(F)$ including the upper bound $M > 0$ must be known for the reconstruction and the state $x^\dagger$ to be reconstructed must satisfy $x^\dagger \in \mathcal{D}(F)$ [57].

Note that the additional regularity of the parameters in the conditional stability estimate is essential: An analogous stability estimate holding independently of the regularity of the parameters implies uniqueness and stability of the inverse problem and a relaxation to a minimum norm solution would give a stable reconstruction of $x^\dagger$, making the problem well-posed. It turns out, that conditional stability estimates are satisfied for various operators, governing ill-posed inverse problems [19, 23, 57, 93]. Furthermore, the approach enables analyzing inverse problems with non-differentiable or even discontinuous forward operators, making it attractive for the non-linear geometry reconstruction problem.

In the following subsection, we provide a modification, where we use Sobolev spaces with different smoothing index to define X and Z. Furthermore we will restrict us to Hölder-type stability ω. On the other hand, we will extend the results to regularization with the seminorm, like it was initially proposed by Tikhonov in his regularization technique [97]. This reduces the approximation error of the reconstruction technique. Furthermore, beside the *a priori* choice $\alpha = \alpha(\delta)$, we consider the *a posteriori* parameter choice by the discrepancy principle.

2.2.3 Tikhonov Regularization under Conditional Stability Estimates

For our analysis, we consider a particular setting, that fits into the abstract framework presented in the previous subsection.

Setting: Let $\Omega \subset \mathbb{R}^d$ be some bounded Lipschitz domain. We consider the Hilbert space

$X := L^2(\Omega)$ as parameter space and a general Hilbert space Y as space for the measurements. Finally, we introduce the measurement operator $F : \mathcal{D}(F) \subset X \to Y$ with domain

$$\mathcal{D}(F) \subseteq H^k(\Omega) \subset X \text{ convex and closed,} \tag{2.18}$$

where $k \in \mathbb{N}$ is the regularity order. We define $\|x\|_0 := \|x\|_{L^2(\Omega)}$ and $|x|_k := \|D^k x\|_{L^2(\Omega)}$. It is well known [1, p. 135] that $\|\cdot\|_{H^k(\Omega)}$ and $\|\cdot\|_k^2 := \|\cdot\|_0 + |\cdot|_k^2$ are equivalent.

Remark 2.4. The scale of fractional Sobolev spaces $H^s(\Omega)$ - after a rescaling of norms - can be obtained by complex interpolation. Let $s \in [0, k]$. We obtain for $x \in H^k(\Omega)$

$$\|x\|_{H^s(\Omega)} \leq \|x\|_0^{1-s/k} \|x\|_k^{s/k}. \tag{2.19}$$

For the subsequent analysis, we require that the forward operator satisfies a conditional stability estimate.

Assumption 2.5 (Conditional stability estimate)**.** *Let C_{cs} be a constant, such that*

$$\|x_1 - x_2\|_0 \leq C_{cs} \|F(x_1) - F(x_2)\|_Y \quad \forall x_1, x_2 \in \mathcal{D}(F). \tag{2.20}$$

We shall see later, that this condition is satisfied by the investigated operators. Note that we assume a Lipschitz stability function $\omega(s) = s$. Furthermore, we have no bound on $\|x_1\|_k$ and $\|x_2\|_k$.

We consider inverse problems of the following type:

$$\text{Find } x \in \mathcal{D}(F) \text{ with } F(x) = y^\delta, \tag{2.21}$$

where the noisy measurement $y^\delta \in Y$ satisfies with the exact parameter $x^\dagger \in \mathcal{D}(F)$

$$\|F(x^\dagger) - y^\delta\|_Y \leq \delta. \tag{2.22}$$

We assume, that the upper bound on the data error δ is available. For the stable solution, we consider generalized minimizers of the Tikhonov functional

$$\mathcal{T}_\alpha^\delta(x) := \left\|F(x) - y^\delta\right\|_Y^2 + \alpha |x|_k^2, \tag{2.23}$$

where $\alpha > 0$ is some regularization parameter and the seminorm is utilized for the regularization. We shall see later, that the regularization in the seminorm may substantially reduce the bias, that is incorporated by the Tikhonov regularization. In this direction, the proposed technique is an extension of the consisting approach of Cheng and Yamamoto [19]. The set of *approximate Tikhonov minimizers* (of tolerance δ^2) is defined by

$$\mathcal{M}_\alpha^\delta := \left\{ x \in \mathcal{D}(F) \mid \mathcal{T}_\alpha^\delta(x) \leq \min_{y \in \mathcal{D}(F)} \mathcal{T}_\alpha^\delta(y) + \delta^2 \right\}. \tag{2.24}$$

Note that since $x^\dagger \in \mathcal{D}(F)$ we have $\mathcal{D}(F) \neq \emptyset$ and an approximate Tikhonov minimizer $x_\alpha^\delta \in \mathcal{M}_\alpha^\delta$ exists by construction, but is usually not unique. We provide a comprehensive convergence analysis for approximate Tikhonov minimizers under the conditional stability assumption.

Auxiliary result: The first term in the Tikhonov functional ensures accordance with the data and the second term ensures the regularity of the reconstructed state. The regularization parameter α weights between the two terms. A simple computation reveals, that an upper bound on α controls the approximation error, whereas a lower bound controls the seminorm of the reconstruction:

Lemma 2.6. *Let $x_\alpha^\delta \in \mathcal{M}_\alpha^\delta$ be an approximate Tikhonov minimizer. Then we have*

$$\left\|F\left(x_\alpha^\delta\right) - y^\delta\right\|_Y^2 \leq 2\delta^2 + \alpha|x^\dagger|_k^2, \tag{2.25}$$

$$\left|x_\alpha^\delta\right|_k^2 \leq 2\frac{\delta^2}{\alpha} + |x^\dagger|_k^2. \tag{2.26}$$

Proof. Inserting the solution $x^\dagger \in \mathcal{D}(F)$ in the Tikhonov functional yields

$$\begin{aligned}\left\|F\left(x_\alpha^\delta\right) - y^\delta\right\|_Y^2 + \alpha\left|x_\alpha^\delta\right|_k^2 &= \mathcal{T}_\alpha^\delta\left(x_\alpha^\delta\right)\\ &\leq \mathcal{T}_\alpha^\delta\left(x^\dagger\right) + \delta^2\\ &= \left\|F\left(x^\dagger\right) - y^\delta\right\|_Y^2 + \alpha\left|x^\dagger\right|_k^2 + \delta^2\\ &= 2\delta^2 + \alpha|x^\dagger|_k^2.\end{aligned}$$

The first assertion follows by neglecting the regularization term on the left hand side, the second one by neglecting the data fidelity term and dividing by α. □

Main result: To entirely define the reconstruction process, we have to specify the regularization parameter in dependence of the noise level δ (2.22). On the one hand, we consider the explicit *a priori* choice $\alpha(\delta) := \delta^2/M^2$, where $M \geq |x^\dagger|_k$ is an upper bound on the size of the solution. As alternative strategy, we consider the discrepancy principle.

Definition 2.7. *Let $\alpha_{\max} > 0$ be an arbitrarily chosen maximum admissible regularization parameter. Set $\mathcal{A} := \{\alpha_{\max} 2^{-n} \mid n \in \mathbb{N}_0\}$. Let $x_\alpha^\delta \in \mathcal{M}_\alpha^\delta$ be an approximate Tikhonov minimizer for every $\alpha \in \mathcal{A}$. Define*

$$\alpha(\delta, y^\delta) := \max\left\{\alpha \in \mathcal{A} \mid \left\|F\left(x_\alpha^\delta\right) - y^\delta\right\|_Y \leq 2\delta\right\}. \tag{2.27}$$

The parameter $\alpha(\delta, y^\delta)$ depends on the concrete choice of the approximate Tikhonov minimizers $x_\alpha^\delta \in \mathcal{M}_\alpha^\delta$. For $\alpha \leq \delta^2/|x^\dagger|_k^2$ we have by Lemma 2.6

$$\left\|F\left(x_\alpha^\delta\right) - y^\delta\right\|_Y \leq \sqrt{2\delta^2 + \alpha|x^\dagger|_k^2} \leq \sqrt{3}\delta < 2\delta.$$

The set in (2.27) is non-empty, bounded from above and its supremum obviously contained. Hence, the regularization parameter is with fixed sequence of approximate Tikhonov minimizers x_α^δ well-defined. Independently of the concrete choice of this sequence, we obtain for sufficiently large $\alpha_{\max}$ a suitable reconstruction, as the following convergence result yields.

Theorem 2.8. *Let Assumption 2.5 hold true, $x^\dagger \in \mathcal{D}(F)$, $y^\delta \in Y$ and $\|y^\delta - F(x^\dagger)\|_Y \leq \delta$. Then we have for the a priori choice $\alpha(\delta) = \delta^2/M^2$, where $M \geq |x^\dagger|_k$, and any approximate Tikhonov minimizer $x_\alpha^\delta \in \mathcal{M}_\alpha^\delta$ the estimate*

$$\left\|x_\alpha^\delta - x^\dagger\right\|_s \leq C\,\delta^{1-s/k}\,(\delta + M)^{s/k}, \quad 0 \leq s \leq k, \tag{2.28}$$

with constant C depending only on Ω, k and C_{cs}. The same result holds with $M := \max\{|x^\dagger|_k, \delta/\sqrt{\alpha_{\max}}\}$, if $\alpha = \alpha(\delta, y^\delta)$ is chosen by the discrepancy principle (2.27).

Proof. We consider both parameter choices at the same time and divide the proof into 4 steps.

Step 1: Estimating the data error. For the *a priori* choice $\alpha = \delta^2/M^2$, Lemma 2.6 yields

$$\left\|F\left(x_\alpha^\delta\right) - y^\delta\right\|_Y \leq \sqrt{2\delta^2 + \frac{|x^\dagger|_k^2}{M^2}\delta^2} \leq \sqrt{3}\delta.$$

For $\alpha = \alpha(\delta, y^\delta)$ we obtain from the definition of the discrepancy principle $\|F(x_\alpha^\delta) - y^\delta)\|_Y \leq 2\delta$. Therefore, we have in all cases

$$\left\|F\left(x_\alpha^\delta\right) - F\left(x^\dagger\right)\right\|_Y \leq \left\|F\left(x_\alpha^\delta\right) - y^\delta\right\|_Y + \left\|y^\delta - F\left(x^\dagger\right)\right\|_Y \leq C\delta.$$

Step 2: Estimating the reconstruction error in the weak norm. We have $x_\alpha^\delta, x^\dagger \in \mathcal{D}(F)$. The conditional stability estimate (2.20) and the data error estimate (2.22) yield

$$\left\|x_\alpha^\delta - x^\dagger\right\|_0 \leq C_{cs}\left\|F\left(x_\alpha^\delta\right) - F\left(x^\dagger\right)\right\|_Y \leq C_{cs}\,C\,\delta.$$

Step 3: Estimating the reconstruction error. For the *a priori* choice $\alpha = \delta^2/M^2$ we have by the second estimate of Lemma 2.6

$$\left|x_\alpha^\delta\right|_k \leq \sqrt{2\,M^2 + |x^\dagger|_k^2} \leq \sqrt{3}\,M.$$

Now consider the choice $\alpha = \alpha(\delta, y^\delta)$, for which we distinguish two cases: In the exceptional case, the maximum regularization parameter is chosen with $\alpha = \alpha_{\max} \geq \delta^2/M^2$. In the usual case, the discrepancy criterion is violated for the doubled parameter 2α and we obtain for the corresponding specific approximate Tikhonov minimizer $x_{2\alpha}^\delta \in \mathcal{M}_{2\alpha}^\delta$ from the data error estimate of Lemma 2.6

$$(2\delta)^2 < \left\|F\left(x_{2\alpha}^\delta\right) - y^\delta\right\|_Y^2 \leq 2\delta^2 + 2\alpha|x^\dagger|_k^2.$$

Thus $\alpha > \delta^2/|x^\dagger|_k^2 > \delta^2/M^2$. In both cases the stability estimate of Lemma 2.6 yields

$$\left|x_\alpha^\delta\right|_k \leq \sqrt{2\frac{\delta^2}{\alpha} + |x^\dagger|_k^2} \leq \sqrt{3}M.$$

Summarizing, the strong seminorm of the error is bounded by

$$\left|x_\alpha^\delta - x^\dagger\right|_k \leq \left|x_\alpha^\delta\right|_k + \left|x^\dagger\right|_k \leq (\sqrt{3}+1)M.$$

In combination with the error estimate from Step 2, we obtain

$$\left\|x_\alpha^\delta - x^\dagger\right\|_k = \sqrt{\|x_\alpha^\delta - x^\dagger\|_0^2 + |x_\alpha^\delta - x^\dagger|_k^2} \leq C\,(\delta + M)\,.$$

Step 4: Interpolating the reconstruction error. By interpolation we have

$$\left\|x_\alpha^\delta - x^\dagger\right\|_s = \left\|x_\alpha^\delta - x^\dagger\right\|_0^{1-s/k} \left\|x_\alpha^\delta - x^\dagger\right\|_k^{s/k} \leq C\,\delta^{1-s/k}\,(\delta + M)^{s/k}\,.$$

Thus, we have established convergence of the approximate Tikhonov minimizers. □

Remark 2.9. Assume, that $\delta < |x^\dagger|_k$. Then the error estimate simplifies to

$$\left\|x_\alpha^\delta - x^\dagger\right\|_s \leq C\,\delta^{1-s/k}\,|x^\dagger|_k^{s/k}$$

for an appropriatly chosen α. In a fixed space $H^s(\Omega)$, we can achieve convergence with arbitrary rate $\gamma < 1$ by regularization in the seminorm $|\cdot|_k$ with $k = s/(1-\gamma)$ under the only condition, that the solution $x^\dagger$ is sufficiently smooth. The conditional stability estimate remains valid for stronger regularization.

2.2.4 Discussion

At the end of this section, we emphasize some points of the proposed framework.

Choice of the regularization parameter: We have considered an *a priori* parameter $\alpha(\delta) = \delta^2/M^2$ and $\alpha(\delta, y^\delta)$ by the discrepancy principle. Both require knowledge of δ, which is essential for convergent parameter choices [28, Thm. 3.3, p. 52]. The *a priori* choice demands knowledge about the size of $|x^\dagger|_k$. The discrepancy principle is an *a posteriori* parameter choice, since it requires knowledge of the approximate Tikhonov minimizer x_α^δ, potentially leading to several, at most $\log(\delta)$ many solves with different parameters, when a high-regularized Tikhonov minimizer produced by an initially chosen large regularization parameter is discarded. However, from a practical viewpoint, it provides a better balance between approximation error and noise amplification. Furthermore, the large regularization parameter simplifies the numerical solution and $x_{2\alpha}^\delta$ is a good initial value for the computation of x_α^δ.

Approximate Tikhonov minimizers: The relaxation from exact to approximate Tikhonov minimizers has several advantages. The existence is guaranteed by $x^\dagger \in \mathcal{D}(F)$. The computation of approximate Tikhonov minimizers remains difficult, since optimization algorithms compute only local minimizer. However, the theory covers also approximations of minimizers resulting from non-exact iterative optimization algorithms and even the use of appropriate (smooth) approximations $\widetilde{F}$ of the possibly non-differentiable forward operator F, which is important for the justification of numerical approximations.

Proposition 2.10. *Let $\widetilde{F} : \mathcal{D}(F) \to Y$ with $\|\widetilde{F}(x) - F(x)\|_Y \leq C_0\delta$ for all $x \in \mathcal{D}(F)$ with $\|x\|_k \leq C$ for sufficiently large C. Let $x_1, x_2 \in \mathcal{D}(F)$ be approximate Tikhonov minimizers for $\widetilde{T}_\alpha^\delta$ respective $\mathcal{T}_\alpha^\delta$ with tolerance $C_1^2\delta^2$, where $\widetilde{T}$ is defined in (2.23) with F replaced by $\widetilde{F}$. Let $\|\widetilde{F}(x_1) - y^\delta\|_Y \leq C_2\delta$ and $\|F(x_2) - y^\delta\|_Y \leq C_2\delta$. Then x_1 is an approximate Tikhonov minimizer of $\mathcal{T}_\alpha^\delta$ with tolerance $c\delta^2$, where $c = 2C_0^2 + 4C_0C_2 + 2C_1^2$.*

Proof. By the triangle inequality and the estimate on the approximation error we have

$$\begin{aligned}
\mathcal{T}_\alpha^\delta(x_1) &= \left\|F(x_1) - y^\delta\right\|_Y^2 + \alpha\,|x_1|_k^2 \\
&\leq \left(\left\|F(x_1) - \widetilde{F}(x_1)\right\|_Y + \left\|\widetilde{F}(x_1) - y^\delta\right\|_Y\right)^2 + \alpha\,|x_1|_k^2 \\
&= \widetilde{T}_\alpha^\delta(x_1) + \left\|\widetilde{F}(x_1) - F(x_1)\right\|_Y^2 + 2\,\left\|\widetilde{F}(x_1) - F(x_1)\right\|_Y\,\left\|\widetilde{F}(x_1) - y^\delta\right\|_Y \\
&\leq \widetilde{T}_\alpha^\delta(x_1) \;+\; C_0^2\delta^2 \;+\; 2C_0C_2\delta^2.
\end{aligned}$$

A similar estimate reveals, that

$$\widetilde{T}_\alpha^\delta(x_2) \;\leq\; \mathcal{T}_\alpha^\delta(x_2) \;+\; C_0^2\delta^2 \;+\; 2C_0C_2\delta^2.$$

Since x_1 and x_2 are approximate Tikhonov minimizers of $\widetilde{T}_\alpha^\delta$ respective $\mathcal{T}_\alpha^\delta$, we can show the assertion

$$\begin{aligned}
\mathcal{T}_\alpha^\delta(x_1) &\leq \widetilde{T}_\alpha^\delta(x_1) \;+\; \left(C_0^2 + 2C_0C_2\right)\delta^2 \\
&\leq \widetilde{T}_\alpha^\delta(x_2) \;+\; \left(C_0^2 + 2C_0C_2 + C_1^2\right)\delta^2 \\
&\leq \mathcal{T}_\alpha^\delta(x_2) \;+\; \left(2C_0^2 + 4C_0C_2 + C_1^2\right)\delta^2 \\
&\leq \inf_{x\in\mathcal{D}(F)} \mathcal{T}_\alpha^\delta(x) \;+\; \left(2C_0^2 + 4C_0C_2 + 2C_1^2\right)\delta^2.
\end{aligned}$$

Since approximate Tikhonov minimizers are bounded, the results holds, if $\|\widetilde{F}(x) - F(x)\|_Y \leq C_0\delta$ only for $x \in \mathcal{D}(F)$ with $\|x^\dagger\|_k \leq C$. □

Consequently, we may replace the measurement operator F by a numerical approximation $\widetilde{F}$. If the approximation is of order δ, the convergence behaviour of the associated reconstructions is preserved.

2.3 Parametrization

The mathematical formulation of the geometry reconstruction problem and the analysis of the subsequent velocity approximation and wall shear stress computation uses a parametric representation of the geometry. Motivated by the typical geometries of vessels and their cross-sections, we utilize parametrizations of a perturbed circular (2D) respectively tubular (3D) domain.

For the analysis of the geometry reconstruction problem, some results regarding the connection between the parametrization and the associated domain are necessary, which will be derived in Subsection 2.3.3.

In the subsequent velocity approximation problem, we have to deal with inexact approximations of the geometry. To allow for comparing velocities on different domains, that is necessary for the analysis of the velocity approximation, we have to represent functions on a uniform reference domain. This requires the extension of the parametrization to a domain transformation, that is sufficiently smooth with respect to both, the spatial variable and the geometry parameter, which is carried out in Subsection 2.3.4.

Finally, the estimation of wall shear stress requires access to the normal direction of the flow geometry. Like for the domain transformation, we establish smoothness of the outer normal direction with respect to the geometry parameter in Subsection 2.3.5.

2.3.1 Parametrization in 2D

When considering cross-sections of blood vessels, we may assume Ω to be a deformed circle with smooth boundary. By shifting the origin to some central point, we assume, that Ω is star-shaped with respect to the origin. We introduce the 1-torus as parameter domain $D := \mathbb{S}^1 \simeq (-\pi, \pi]$ and the polar basis

$$e_r(\varphi) := \begin{pmatrix} \cos(\varphi) \\ \sin(\varphi) \end{pmatrix}, \quad e_\varphi(\varphi) := \begin{pmatrix} -\sin(\varphi) \\ \cos(\varphi) \end{pmatrix}, \quad \varphi \in D.$$

We parametrize Ω by a radius function, defining the distance between the origin and the boundary in direction $e_r(\varphi)$ by a function of the polar variable φ.

Definition 2.11. *Let $R_{\min} \leq R_{\max} \in \mathcal{C}(\mathcal{S}^1)$ with $R_{\min} \geq C > 0$. The set of admissible parametrizations is given by*

$$\mathcal{G} := \{\, R \in \mathcal{C}^1(\mathcal{S}^1) \mid R_{\max} \geq R \geq R_{\min} \,\}. \tag{2.29}$$

Let $R \in \mathcal{G}$. Then R is associated with the domain

$$\Omega = \Omega(R) = \{ r e_r(\varphi, s) \mid 0 \leq r < R(\varphi),\ -\pi < \varphi \leq \pi \}. \tag{2.30}$$

The parametrization is depicted in Figure 2.1. The lower bound $R_{\min}$ is required for some inverse inequalities. The upper bound $R_{\max}$ is chosen to ensure $\Omega(R) \subseteq \Omega_{\mathrm{FOV}}$, i.e. the domain is contained in the field of view. Note that definition (2.29) implicitly contains corresponding boundary conditions, reflecting the periodicity of $D = \mathcal{S}^1$.

2.3.2 Parametrization in 3D

We consider subsets Ω of a blood vessel that look like a deformed pipe with smooth boundary. Since the pipe may be curved, as it is the case in the aortic arch, the parametrization is based on a centerline $\gamma \in \mathcal{C}^3([0,1]; \mathbb{R}^3)$. We define the parameter domain $D := \mathbb{S}^1 \times (0,1)$.

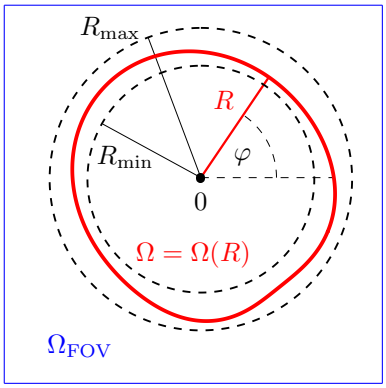

Figure 2.1: Parametrization of the domain $\Omega \subset \Omega_{\text{FOV}}$ by the radius function R.

Analogously to the two-dimensional case, we parametrize Ω by a radius function, defining the distance between the centerline and the boundary at the axial position s in the direction defined by φ. Before we define the parametrization, there are two difficulties to overcome:

- We have to define an appropriate axially aligned coordinate system.
- We have to ensure, that the assignment of an axial position to a physical point is unique.

Let $\overline{L}$ be the length of the centerline. We assume, that the speed $L(s) := \|\partial_s \gamma(s)\|$ is nearly constant, i.e. there is $c \ll 1$ with

$$(1-c)\overline{L} \;\leq\; L(s) \;\leq\; (1+c)\overline{L} \quad \forall s \in [0,1].$$

With this condition, the current axial direction is accessible in a stable manner by normalizing the tangential

$$t \in \mathcal{C}^k([0,1];\mathbb{R}^3), \quad t(s) := \frac{\partial_s \gamma(s)}{L(s)}.$$

A standard choice for the extension to an axially aligned coordinate system is given by the Frenet-Serret formulas [55], yielding the TNB (tangential, normal, binormal) frame:

$$t_{FS}(s) := \frac{\partial_s \gamma(s)}{L(s)}, \quad n_{FS}(s) := \frac{\partial_s t(s)}{\|\partial_s t(s)\|}, \quad b_{FS}(s) := t_{FS}(s) \times n_{FS}(s).$$

For a centerline with constant speed, the axial direction t_{FS} and the main normal n_{FS} are perpendicular. The TNB frame is defined by local quantities only. However, it is not appropriate for our purposes, since the main normal becomes unstable or even discontinuous in the axial position s at sections with low curvature as depicted in Figure 2.2.

Therefore, we introduce a stabilized frame, which is based on an approximate main normal, that is updated, when the tangential direction has changed significantly.

Step 1: Partition. Set $s_0 = 0$ and for $s_{m-1} \leq 1$ set

$$s_m := \min\left(\{s \in (s_{m-1}, 1) \mid \|t(s_{m-1}) \times t(s)\| \geq 1/10\} \cup \{1\}\right).$$

The iteration terminates at iteration $m = N$ with $s_N = 1$ by compactness.

Step 2: Discrete main normal. Starting with some arbitrary n_0 perpendicular to $t(0)$, we subsequentially define the normal vectors

$$n_m := [t(s_m) \times n_{m-1}] \times t(s_m) \quad \text{for } m = 1, ..., N.$$

Step 3: Approximate main normal. Let $(\phi_m)_m \subset \mathcal{C}^3([0,1])$ be a partition of unity with local support, i.e. $\text{supp}(\phi_m) \subseteq [s_{m-1}, s_{m+1}]$, and $\phi_m(s_j) = \delta_{mj}$. Set

$$\tilde{n}(s) := \sum_{m=0}^{N} n_m \, \phi_m(s).$$

The stabilized frame is then defined by

$$t(s) := \frac{\partial_s \gamma(s)}{L(s)}, \quad b(s) := \frac{t(s) \times \widetilde{n}(s)}{\|t(s) \times \widetilde{n}(s)\|}, \quad n(s) := b(s) \times t(s). \tag{2.31}$$

By construction, $t(s), n(s), b(s)$ is a locally defined right-handed coordinate system, which is $\mathcal{C}^3$-regular in s, as it is illustrated in Figure 2.3. We extend $t(s)$ to a cylindrical basis by introducing

$$\begin{array}{rcl} e_r(\varphi, s) & := & \cos(\varphi) n(s) + \sin(\varphi) b(s), \\ e_\varphi(\varphi, s) & := & -\sin(\varphi) n(s) + cos(\varphi) b(s). \end{array} \tag{2.32}$$

Now we consider the transformation

$$F : \mathbb{R}_+ \times (-\pi, \pi] \times [0,1] \to \mathbb{R}^3, \; F(r, \varphi, s) = \gamma(s) + r e_r(\varphi, s). \tag{2.33}$$

In general, the transformation F is not invertible, since a point may be in the cross section for several axial positions s. Let $x_0 = F(r_0, \varphi_0, s_0)$, then the axial position $s = s_0$ is characterized by the orthogonality relation

$$f(s) := \langle x_0 - \gamma(s), t(s) \rangle = 0.$$

The problem is locally well-posed, if $\partial_s f(s_0) \neq 0$. We compute

$$\begin{aligned} \partial_s f(s_0) &= \langle r_0 e_r(\varphi_0, s_0), \partial_s t(s_0) \rangle - \langle \partial_s \gamma(s_0), t(s_0) \rangle \\ &= -r_0 \langle \partial_s e_r(\varphi_0, s_0), t(s_0) \rangle - L(s), \end{aligned}$$

where we used $\langle e_r(\varphi, s), t(s) \rangle = 0$ and hence

$$\partial_s \langle e_r(\varphi, s), t(s) \rangle = \langle \partial_s e_r(\varphi, s), t(s) \rangle + \langle e_r(\varphi, s), \partial_s t(s) \rangle = 0.$$

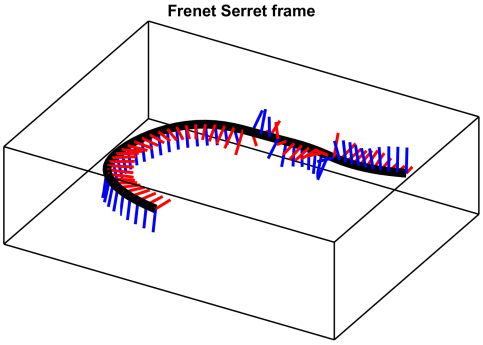

Figure 2.2: TNB frame by Frenet Serret formulas with n_{FS} (red) and b_{FS} (blue).

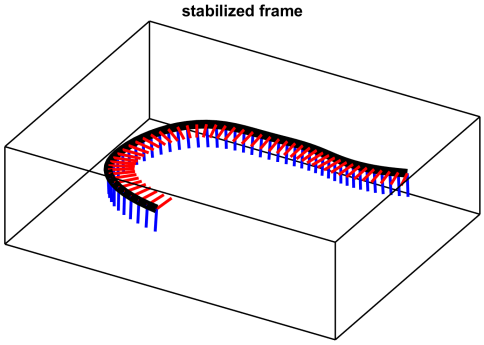

Figure 2.3: Stabilized frame given by (2.31) with n (red) and b (blue).

Therefore, we introduce an upper bound $R_{\max} \in \mathcal{C}(\overline{D})$ for the radius with

$$L + R_{\max}\langle \partial_s e_r, t\rangle \geq C > 0. \tag{2.34}$$

Since this guarantees only local well-posedness for $r \leq R_{\max}$, we define the cross sectional domains

$$Q(s) = \{\gamma(s) + re_r(\varphi, s) \mid 0 \leq r \leq R_{\max}(\varphi, s), -\pi < \varphi \leq \pi\}$$

and postulate

$$Q(s_1) \cap Q(s_2) = \emptyset \quad \forall s_1 \neq s_2 \in [0,1]. \tag{2.35}$$

In practice, the axial position is computed by a Newton method from the orthogonality relation, were the initial guess is determined by sampling. Finally, we define the set of admissible parametrizations and the geometry representation.

Definition 2.12. *Let $R_{\min} \leq R_{\max} \in C(\overline{D})$ with $R_{\min} \geq C > 0$ and $R_{\max}$ fulfil (2.34) and (2.35). The set of admissible parametrizations is given by*

$$\mathcal{G} := \{\, R \in \mathcal{C}(\overline{D}) \mid R_{\max} \geq R \geq R_{\min} \,\} \tag{2.36}$$

Let $R \in \mathcal{G}$. Then R is associated with the domain

$$\Omega = \Omega(R) = \{\gamma(s) + re_r(\varphi, s) \mid 0 \leq r < R(\varphi, s),\ -\pi < \varphi \leq \pi,\ 0 < s < 1\}\,. \tag{2.37}$$

Again, the periodicity of the parametric domain $D = \mathcal{S}^1 \times (0,1)$ implies corresponding boundary conditions in the polar variable. For ease of presentation, we will skip the dependence on the parametrization of associated objects in the following, for example $\Omega = \Omega(R)$, $\Omega_1 = \Omega(R_1)$.

Remark 2.13. It is possible, to extend a 2D geometry to a 3D geometry by introducing an artificial axial direction. In this case, the centerline is $\gamma(s) = (0, 0, s)^T$ with frame $(t, n, b) = (e_z, e_x, e_y)$ and all quantities except of γ are independent of the axial position s. Due to $\partial_s e_r = 0$, conditions (2.34) and (2.35) are satisfied for arbitrary $R_{\max}$.

2.3.3 Correlation between Domains and their Parametrization

In the following analysis, we will restrict ourselves to the 3D case, since the 2D case can be cast in the 3D framework.

Lemma 2.14. *Let $R_1, R_2 \in \mathcal{G}$, with $\mathcal{G}$ given by (2.36). Then*

$$|\Omega_1 \setminus \Omega_2| \leq \|\chi_1 - \chi_2\|_{L^1(\Omega_{\mathrm{FOV}})} \leq C \, \|R_1 - R_2\|_{L^1(D)} \, .$$

Proof. The first inequality is obviously satisfied. We estimate

$$\begin{aligned}
\|\chi_1 - \chi_2\|_{L^1(\Omega_{\mathrm{FOV}})} &= \int_D \left(\int_{\min\{R_1,R_2\}}^{\max\{R_1,R_2\}} r \, (L + r\langle \partial_s e_r, t \rangle) \, \mathrm{d}r \right) \mathrm{d}(\varphi, s) \\
&\leq C(\gamma) \int_D \left(\int_{\min\{R_1,R_2\}}^{\max\{R_1,R_2\}} r \, \mathrm{d}r \right) \mathrm{d}(\varphi, s) \\
&= C(\gamma) \int_D |R_1 - R_2| \; |R_1 + R_2| \; \mathrm{d}(\varphi, s) \\
&\leq 2 \, C(\gamma) \; \|R_{\max}\|_{L^\infty(D)} \; \|R_1 - R_2\|_{L^1(D)} \, ,
\end{aligned}$$

which proves the second inequality. □

Lemma 2.15. *Let $R_1, R_2 \in \mathcal{G}$, with $\mathcal{G}$ given by (2.36). Then*

$$\|\chi_1 - \chi_2\|_{L^1(\Omega_{\mathrm{FOV}})} \geq C \, \|R_1 - R_2\|^2_{L^2(D)} \, ,$$

where $C \geq C(\gamma) > 0$ and $C \to \infty$ for $\|R_{\max}/R_{\min}\|_{L^\infty(D)} \to 1$.

Proof. Similarly to the previous lemma, we have

$$\begin{aligned}
\|\chi_1 - \chi_2\|_{L^1(\Omega_{\mathrm{FOV}})} &= \int_D \int_{\min\{R_1,R_2\}}^{\max\{R_1,R_2\}} r \; (L + r\langle \partial_s e_r, t \rangle) \, \mathrm{d}r \, \mathrm{d}(\varphi, s) \\
&\geq C(\gamma) \int_D \int_{\min\{R_1,R_2\}}^{\max\{R_1,R_2\}} r \, \mathrm{d}r \, \mathrm{d}(\varphi, s) \\
&= C(\gamma) \int_D |R_1 - R_2| \; |R_1 + R_2| \; \mathrm{d}(\varphi, s).
\end{aligned}$$

The assertion follows from monotonicity of $f(x) = \frac{x-1}{x+1}$ with $x = \frac{\max\{R_1,R_2\}}{\min\{R_1,R_2\}}$ by

$$\begin{aligned}\|R_1 - R_2\|^2_{L^2(D)} &= \int_D |R_1 - R_2|\ |R_1 + R_2| \left|\frac{R_1 - R_2}{R_1 + R_2}\right| \mathrm{d}(\varphi, s) \\ &\leq \left(1 - \frac{2}{1 + \|R_{\max}/R_{\min}\|_{L^\infty(D)}}\right) \int_D |R_1 - R_2|\ |R_1 + R_2|\ \mathrm{d}(\varphi, s).\end{aligned}$$

□

These results imply a generalized continuity between parametrization R and domain Ω and vice versa. They are essential for the conditional stability estimate of the geometry reconstruction problem.

2.3.4 Transformation from Reference Domain to Flow Domain

The geometry parameter R defines only a parametrization for the wall part $\Gamma(R) \subset \partial\Omega(R)$, i.e. the surface of the cylinder without the upper and lower cross section. We now define two possible extensions to domain transformations, mapping a certain reference domain $\widehat{\Omega}$ to the physical flow domain Ω respective a part of it.

Definition 2.16 (Local Version)**.** *Let $R_0 \in \mathcal{C}^3(\overline{D})$ with $0 < R_0 < R_{\min}$. Define the reference domain $\widehat{\Omega} := (0,1) \times \mathcal{S}^1 \times (0,1)$ with reference wall $\widehat{\Gamma}_W := \{1\} \times \mathcal{S}^1 \times (0,1) \sim D$. For $R \in \mathcal{G}$ we define the local domain transformation*

$$\Phi_R(r, \varphi, s) := \gamma(s) + [R_0(\varphi, s)\ +\ r\,(R(\varphi, s) - R_0(\varphi, s))]\, e_r(\varphi, s).$$

If we consider several domain transformations from different parametrizations R_i, the transformation parameters $\varphi_0, \varphi_1, s_0, s_1, R_0$ are equal. In the following, we will usually skip these details. Naturally, we have $\Phi_R(\widehat{\Omega}) \subsetneq \Omega$, but in some cases we will mean $\Omega := \Phi_R(\widehat{\Omega})$ for ease of presentation, since we simultaneously consider.

Definition 2.17 (Global Version)**.** *Define the reference domain as unit cylinder $\widehat{\Omega} := \mathcal{B}^2 \times (0,1)$, where $\mathcal{B}^2$ denotes the unit disk. The associated reference wall is $\widehat{\Gamma}_W := \{1\} \times \mathcal{S}^1 \times (0,1) \sim D$. For $R \in \mathcal{G}$ we set $R_0 := \min_{(\varphi,s)\in\overline{D}} R(\varphi, s)$ and define the global domain transformation*

$$\Phi_R(r, \varphi, s)\ :=\ \gamma(s) + \left[rR_0 + r^4\,(R(\varphi, s) - R_0)\right] e_r(\varphi, s).$$

In the following, we establish auxiliary results, regarding smoothness and stability of the forward transformation, invertibility and finally smoothness and stability of the inverse transformation. For both versions, we have the following stability result.

Lemma 2.18. *Let $R, R_1, R_2 \in \mathcal{G}$. Let Φ_R, Φ_1, Φ_2 be either the local or the global associated domain transformations. Then we have $\Phi_R \in \mathcal{C}^1(\widehat{\Omega})$ with the stability estimate*

$$\|\Phi_R\|_{W^{m,\infty}(\widehat{\Omega})} \leq C\,(\gamma)\left(1 + \|R\|_{W^{m,\infty}(D)}\right) \quad \text{for } m = 0, 1.$$

The differences satisfy the estimate

$$\|\Phi_1 - \Phi_2\|_{W^{m,\infty}(\widehat{\Omega})} \leq C(\gamma)\,\|R_1 - R_2\|_{W^{m,\infty}(D)} \quad \text{for } m = 0, 1.$$

For $R, R_1, R_2 \in \mathcal{G} \cap \mathcal{C}^3(\overline{D})$ we have $\Phi_R \in \mathcal{C}^3(\widehat{\Omega})$ and analogous estimates for $m = 2, 3$.

Proof. We distinguish between the local and the global version.

Local version. For $R \in \mathcal{C}^k(\overline{D})$ with $k \leq 3$ we have with the $\mathcal{C}^3$-regularity of the centerline γ, the frame t, n, b and R_0

$$\begin{aligned}\left|D^k \Phi_R\right| \;&\leq\; \left|D^k \gamma\right| \;+\; \sum_{m=0}^{k} C(m)\,\left|D^m\left[R_0 + r\,(R - R_0)\right]\right|\,\left|D^{k-m} e_r\right| \\ &\leq\; C(\gamma)\,\left(1 \;+\; \|R_0\|_{W^{k,\infty}(D)} \;+\; \|R\|_{W^{k,\infty}(D)}\right).\end{aligned}$$

The estimate for the difference follows directly from the stability estimate, since Φ_R is affine linear with respect to R.

Global case. The polar coordinates (φ, r) are non-smooth with a singularity at $r = 0$. Hence, we have to study smoothness in particular at $r = 0$. We split

$$\Phi_R(r, \varphi, s) = \underbrace{\gamma(s) + r\,R_0\,e_r(\varphi, s)}_{F_1(r,\varphi,s)} + \underbrace{r^4\,(R(\varphi, s) - R_0)\;e_r(\varphi, s)}_{F_2(r,\varphi,s)}.$$

Switching to Cartesian coordinates, we have

$$F_1(\hat{x}, \hat{y}, \hat{z}) = \gamma(\hat{z}) + R_0\,\hat{x}\,n(\hat{z}) + R_0\,\hat{y}\,b(\hat{z}).$$

From the $\mathcal{C}^3$-regularity of the centerline γ and the frame t, n, b we obtain $F_1 \in \mathcal{C}^3(\widehat{\Omega})$ and $\|F_1\|_{W^{3,\infty}(\widehat{\Omega})} \leq C(\gamma)(1 + R_0)$.

Regarding the smoothness of F_2, we first observe from elementary calculations, that for a composition $h = f \circ g$ of smooth functions f, g it holds

$$D^k h \;=\; \sum_{\beta \in \mathbb{N}_0^k,\, \sum_{j=1}^k j\beta_j = k} C(\beta)\;\left(\left(D^{|\beta|} f\right) \circ g\right) \prod_{j=1}^{k} \left(D^j g\right)^{\beta_j}. \tag{2.38}$$

We define $f(\varphi, s) := (R(\varphi, s) - R_0)e_r(\varphi, s)$. For $R \in \mathcal{G}$, we find $f \in \mathcal{C}^1(\overline{D})$, periodic in the first argument and $\|f\|_{W^{1,\infty}(D)} \leq C(\gamma)\|R\|_{W^{1,\infty}(D)}$. For $R \in \mathcal{G} \cap \mathcal{C}^3(\overline{D})$, we have $f \in \mathcal{C}^3(\overline{D})$, periodic in the first argument and $\|f\|_{W^{3,\infty}(D)} \leq C(\gamma)\|R\|_{W^{3,\infty}(D)}$.

Furthermore we define $g(\hat{x}, \hat{y}, \hat{z}) := (\varphi, s)$ from the usual polar transformation. Switching to polar coordinates, g is indefinitely often differentiable at $r > 0$ and by elementary calculations we obtain

$$\left|\left(D^k g\right)(r, \varphi, s)\right| \leq C\, r^{-k}.$$

Consequently, we obtain for $h = f \circ g$ at $r > 0$ with $R \in \mathcal{G} \cap \mathcal{C}^3(\overline{D})$

$$|Dh(r, \varphi, s)| \leq C(\gamma)\ \|R\|_{W^{1,\infty}(D)}\ r^{-1}$$

and with $R \in \mathcal{C}^3(\overline{D})$ using the advanced chain rule (2.38) for $k \leq 3$

$$\begin{aligned}
\left|D^k h(r, \varphi, s)\right| &\leq C(\gamma)\ \|R\|_{W^{3,\infty}(D)} \sum_{\beta \in \mathbb{N}_0^k, \sum_{j=1}^k j\beta_j = k} \prod_{j=1}^k \left|D^j g(r, \varphi, s)\right|^{\beta_j} \\
&\leq C(\gamma)\ \|R\|_{W^{3,\infty}(D)} \sum_{\beta \in \mathbb{N}_0^k, \sum_{j=1}^k j\beta_j = k} \prod_{j=1}^k \left|r^{-j}\right|^{\beta_j} \\
&\leq C(\gamma)\ \|R\|_{W^{3,\infty}(D)}\ r^{-k}.
\end{aligned}$$

Finally, we obtain by the product rule for $R \in \mathcal{G}$

$$\begin{aligned}
|DF_2(r, \varphi, s)| &\leq r^4\, |Dh(r, \varphi, s)| + \left|D(r^4)\right|\ |h(r, \varphi, s)| \\
&\leq C(\gamma)\ \|R\|_{W^{1,\infty}(D)}\, r^3
\end{aligned}$$

and for $R \in \mathcal{G} \cap \mathcal{C}^3(\overline{D})$ with $k \leq 3$

$$\begin{aligned}
\left|D^k F_2(r, \varphi, s)\right| &\leq \sum_{m=0}^k C(m)\ \left|D^{k-m}(r^4)\right|\ |D^m h(r, \varphi, s)| \\
&\leq C(\gamma) \sum_{m=0}^k r^{4-k+m}\ \|R\|_{W^{3,\infty}(D)}\ r^{-m} \\
&\leq C(\gamma)\ \|R\|_{W^{3,\infty}(D)}\, r^{4-k}.
\end{aligned}$$

Hence, the considered derivatives can be continuously extended by $D^k F_2(0, \varphi, s) = 0$ to $r = 0$ with the desired estimates. The estimate for $\Phi_1 - \Phi_2$ follows analogously from the linearity of Φ_R with respect to R and R_0 considering, that for $R_1, R_2 \in \mathcal{G}$ it holds

$$|R_{0,1} - R_{0,2}| = \left|\min_{(\varphi,s)\in\overline{D}} R_1(\varphi, s) - \min_{(\varphi,s)\in\overline{D}} R_2(\varphi, s)\right| \leq \|R_1 - R_2\|_{L^\infty(D)}.$$

□

Lemma 2.19. *Let $R \in \mathcal{G}$ as defined in (2.36). Then Φ_R is injective.*

Proof. In both cases, the local and global version, we can write

$$\Phi_R(r,\varphi,s) = \gamma(s) + f(r;R,R_0,\varphi,s)e_r(\varphi,s),$$

where $0 \le f(\,\cdot\,;R,R_0,\varphi,s) \le R(\varphi,s)$ is strictly monotonic with respect to r.

Let $(r_1,\varphi_1,s_1),(r_2,\varphi_2,s_2) \in \widehat{\Omega}$ with $\Phi_R(r_1,\varphi_1,s_1) = \Phi_R(r_2,\varphi_2,s_2)$. Then the representation implies $\Phi_R(r_i,\varphi_i,s_i) \in Q(s_i)$ for $i = 1,2$ and we have $s_1 = s_2 =: s$. Thus,

$$0 = f(r_1;R,R_0,\varphi_1,s)e_r(\varphi_1,s) - f(r_2;R,R_0,\varphi_2,s)e_r(\varphi_2,s)$$

Since $f \ge 0$ we have $\varphi_1 = \varphi_2 =: \varphi$ and consequently

$$f(r_1;R,R_0,\varphi,s) - f(r_2;R,R_0,\varphi,s) = 0.$$

Since f is strictly monotonic in r, we finally have $r_1 = r_2 = r$. □

Let $\Psi_R = (\Phi_R)^{-1}$ be the inverse transformation. We have the following stability result.

Lemma 2.20. *Let $R,R_1,R_2 \in \mathcal{G}$. Then $\Psi_R = (\Phi_R)^{-1} \in \mathcal{C}^1(\Omega)$ with the stability estimate*

$$\|\Psi_R\|_{W^{1,\infty}(\Omega)} \le C\left(1 + \|R\|^2_{W^{1,\infty}(D)}\right).$$

Furthermore, we have for the differences

$$\|\Psi_1 - \Psi_2\|_{L^\infty(\Omega_1\cap\Omega_2)} \le C\left(1 + \|R_1\|^2_{W^{1,\infty}(D)}\right)\|R_1 - R_2\|_{L^\infty(D)}.$$

If additionally $R_1 \in \mathcal{C}^3(\overline{D})$, then

$$\|\Psi_1 - \Psi_2\|_{W^{1,\infty}(\Omega_1\cap\Omega_2)} \le C\left(\|R_1\|_{W^{3,\infty}(D)}, \|R_2\|_{W^{1,\infty}(D)}\right)\|R_1 - R_2\|_{W^{1,\infty}(D)}.$$

Proof. We split the proof in 3 steps.

Step 1: Stability estimate for derivatives. Again, we consider the representation

$$\Phi_R(r,\varphi,s) = \gamma(s) + f(r;R,R_0,\varphi,s)e_r(\varphi,s).$$

For the local version, we have for the Jacobian

$$D\Phi_R = (e_r \mid e_\varphi \mid t)\begin{pmatrix} \partial_r f & \partial_\varphi f & \partial_s f \\ 0 & f & f\langle \partial_s e_r, e_\varphi\rangle \\ 0 & 0 & L + f\langle \partial_s e_r, t\rangle \end{pmatrix}.$$

We estimate the determinant

$$\begin{aligned}\det D\Phi_R &= (R - R_0)\; f\; (L + f\langle \partial_s e_r, t\rangle) \\ &\ge \min_{(\varphi,s)\in\overline{D}}(R_{\min}(\varphi,s) - R_0(\varphi,s)) \min_{(\varphi,s)\in\overline{D}}(R_0(\varphi,s))\; C(\gamma).\end{aligned}$$

For the global version, we have for the Jacobian in polar coordinates

$$D\Phi_R \;=\; \begin{pmatrix} \partial_r f & \frac{1}{r}\mathrm{d}_\varphi f & \mathrm{d}_s f \\ 0 & \frac{1}{r} f & f\,\langle \partial_s e_r, e_\varphi \rangle \\ 0 & 0 & L \,+\, f\,\langle \partial_s e_r, t \rangle \end{pmatrix}.$$

Again, we estimate the determinant using $R \geq R_0 > 0$

$$\begin{aligned} \det D\Phi_R \;&=\; \partial_r f\, \frac{1}{r} f\; (L \,+\, f\,\langle \partial_s e_r, t\rangle) \\ &=\; \left(R_0 + 4r^3\,(R - R_0)\right)\, \left(R_0 + r^3\,(R - R_0)\right)\, (L \,+\, f\,\langle \partial_s e_r, t\rangle) \\ &\geq\; R_0^2\, C(\gamma) \\ &\geq\; \min_{(\varphi,s)\in\overline{D}} \left(R_{\min}(\varphi, s)\right)^2\, C(\gamma). \end{aligned}$$

Hence, we have established uniform lower bounds for the determinant. In particular, the Jacobian $D\Phi_R$ is invertible and the implicit function theorem yields

$$D\Psi_R = \left(D\Phi_R^{-1}\right) \circ \Psi_R \;=\; \left(\frac{1}{\det D\Phi_R}\, \widetilde{D\Phi_R}\right) \circ \Psi_R,$$

where $\widetilde{D\Phi}_R$ is the adjugate matrix of $D\Phi_R$ consisting of determinants of sub-matrices of $D\Phi_R$. Hence, we obtain using the uniform lower bound C_0 on the determinant, the estimate $\det A \leq C|A|^2$ for $A \in \mathbb{R}^{2,2}$ and the stability estimate for the forward transformation of Lemma 2.18

$$\|D\Psi_R\|_{L^\infty(\Omega)} \;\leq\; C_0^{-1}\, \left\|\widetilde{D\Phi}_R\right\|_{L^\infty(\Omega)} \;\leq\; C\, C_0^{-1}\, \|\Phi_R\|^2_{W^{1,\infty}(\widehat{\Omega})} \;\leq\; C\, C_0^{-1}\, \left(1 + \|R\|^2_{W^{1,\infty}(D)}\right).$$

The estimate $\|\Psi_R\|_{L^\infty(\Omega)} \leq C$ is trivial.

Step 2: Bound on the difference. Let $x \in \Omega_1 \cap \Omega_2$. Set $\hat{x}_i = \Psi_i(x)$ for $i = 1, 2$, where Ψ_i is the inverse transformation associated with R_i. The transformation conserves angular and axial positions independently of R. Thus, $\Phi_1(\hat{x}_1)$ and $\Phi_1(\hat{x}_2)$ have the same angular and axial position and consequently, the direction connection is contained in Ω_1. Using the mean value theorem, we obtain

$$\begin{aligned} |\hat{x}_1 - \hat{x}_2| &= |\Psi_1(\Phi_1(\hat{x}_1)) - \Psi_1(\Phi_1(\hat{x}_2))| \\ &\leq \|\Psi_1\|_{W^{1,\infty}(\Omega_1)}\, |\Phi_1(\hat{x}_1) - \Phi_1(\hat{x}_2)| \\ &= \|\Psi_1\|_{W^{1,\infty}(\Omega_1)}\, |\Phi_2(\hat{x}_2) - \Phi_1(\hat{x}_2)| \\ &\leq \|\Psi_1\|_{W^{1,\infty}(\Omega_1)}\, \|\Phi_1 - \Phi_2\|_{L^\infty(\widehat{\Omega})}. \end{aligned}$$

Hence we have with the stability estimate of Lemma 2.18

$$\|\Psi_1 - \Psi_2\|_{L^\infty(\Omega_1\cap\Omega_2)} \;\leq\; C\left(1 + \|R_1\|^2_{W^{1,\infty}(D)}\right)\, \|R_1 - R_2\|_{L^\infty(D)}.$$

Step 3: Bound on the derivative of the difference. Since the determinant is polynomial in the matrix entries, we obtain

$$\|\det D\Phi_1 - \det D\Phi_2\|_{L^\infty(\widehat{\Omega})} + \left\|\widetilde{D\Phi_1} - \widetilde{D\Phi_2}\right\|_{L^\infty(\widehat{\Omega})} \leq C \, \|\Phi_1 - \Phi_2\|_{W^{1,\infty}(\widehat{\Omega})}$$

with constant C depending on $\|\Phi_1\|_{W^{1,\infty}(\widehat{\Omega})}$ and $\|\Phi_2\|_{W^{1,\infty}(\widehat{\Omega})}$. The representation of the inverse using adjugate matrices, the lower bound on the determinant and the estimates of Lemma 2.18 imply

$$\left\|D\Phi_1^{-1} - D\Phi_2^{-1}\right\|_{L^\infty(\widehat{\Omega})} \leq C \left(\|R_1\|_{W^{1,\infty}(D)}, \|R_2\|_{W^{1,\infty}(D)}\right) \|R_1 - R_2\|_{W^{1,\infty}(D)} .$$

Similar arguments for $R_1 \in \mathcal{C}^3(\overline{D})$ imply

$$\left\|D\Phi_1^{-1}\right\|_{W^{2,\infty}(\widehat{\Omega})} \leq C \left(\|R_1\|_{W^{3,\infty}(\widehat{\Omega})}\right).$$

The assertion follows by

$$\begin{aligned}
&\|D\Psi_1 - D\Psi_2\|_{L^\infty(\Omega_1\cap\Omega_2)} \\
&= \left\|D\Phi_1^{-1} \circ \Psi_1 - D\Phi_2^{-1} \circ \Psi_2\right\|_{L^\infty(\Omega_1\cap\Omega_2)} \\
&\leq \left\|D\Phi_1^{-1} \circ \Psi_1 - D\Phi_1^{-1} \circ \Psi_2\right\|_{L^\infty(\Omega_1\cap\Omega_2)} + \left\|D\Phi_1^{-1} \circ \Psi_2 - D\Phi_2^{-1} \circ \Psi_2\right\|_{L^\infty(\Omega_1\cap\Omega_2)} \\
&\leq \left\|D\Phi_1^{-1}\right\|_{W^{1,\infty}(\widehat{\Omega})} \|\Psi_1 - \Psi_2\|_{L^\infty(\Omega_1\cap\Omega_2)} + \left\|D\Phi_1^{-1} - D\Phi_2^{-1}\right\|_{L^\infty(\widehat{\Omega})} \\
&\leq C \left(\|R_1\|_{W^{3,\infty}(D)}, \|R_2\|_{W^{1,\infty}(D)}\right) \|R_1 - R_2\|_{W^{1,\infty}(D)} .
\end{aligned}$$

□

2.3.5 Outer Normal

The outer normal direction is analytically accessible from the parametrization. Let $R \in \mathcal{G}$ be an admissible radius function. We can map the reference surface $D = \mathcal{S}^1 \times (0,1)$ to the wall part $\Gamma_W = \Phi_R(\{1\} \times D)$ of the boundary of the physical domain Ω. At the surface, we obtain the tangential plane by differentiation and can establish the outer normal direction by the cross product of the tangential directions and normalization.

The surface mapping is given by restricting the domain transformation $\phi(R)$ to $r = 1$

$$\Gamma : D \to \partial\Omega, \quad \Gamma(\varphi, s) = \Phi(1, \varphi, s) = \gamma(s) + R(\varphi, s) e_r(\varphi, s),$$

where the local directions e_r, e_φ are defined in (2.32). Differentiation with respect to φ and s yields the circumferential and axial tangential direction. For ease of presentation we omit the dependence on φ and s and obtain pointwise

$$\begin{aligned}
\tau_\varphi &= \partial_\varphi \Gamma = \partial_\varphi R \, e_r + R \, e_\varphi, \\
\tau_s &= \partial_s \Gamma = \partial_s R \, e_r + R \langle \partial_s e_r, e_\varphi \rangle \, e_\varphi + (L + R\langle \partial_s e_r, t \rangle) \, t.
\end{aligned}$$

The normal direction is defined by the cross-product

$$\tau_\varphi \times \tau_s \;=\; R\,(L + R\langle \partial_s e_r, t\rangle)\, e_r - \partial_\varphi R\,(L + R\langle \partial_s e_r, t\rangle)\, e_\varphi + R\,(\partial_\varphi R\langle \partial_s e_r, e_\varphi\rangle - \partial_s R)\, t.$$

Note that the direction is well defined, since

$$|\tau_\varphi \times \tau_s| \;\geq\; \langle \tau_\varphi \times \tau_s, e_r\rangle \;=\; R\,(L + R\langle \partial_s e_r, t\rangle) \;\geq\; \min_{\varphi,s}\,(R_{\min})\; C(\gamma) \;>\; 0. \tag{2.39}$$

By normalization and the simplification for the two-dimensional case using the extension argument, we obtain the following proposition.

Proposition 2.21. *Let $R \in \mathcal{G}$. Then the outer normal to the wall part Γ_W of the boundary, given as a function on the reference domain D, is in the two-dimensional case*

$$n_{2D} \;=\; \frac{Re_r - \partial_\varphi R e_\varphi}{\sqrt{R^2 + (\partial_\varphi R)^2}}$$

and in the three-dimensional case

$$n_{3D} \;=\; \frac{R\,(L + R\langle \partial_s e_r, t\rangle)\, e_r - \partial_\varphi R\,(L + R\langle \partial_s e_r, t\rangle)\, e_\varphi + R\,(\partial_\varphi R\langle \partial_s e_r, e_\varphi\rangle - \partial_s R)\, t}{\sqrt{[R\,(L + R\langle \partial_s e_r, t\rangle)]^2 + [\partial_\varphi R\,(L + R\langle \partial_s e_r, t\rangle)]^2 + [R\,(\partial_\varphi R\langle \partial_s e_r, e_\varphi\rangle - \partial_s R)]^2}}.$$

We conclude the preliminaries on the parametrization with the following stability result.

Lemma 2.22. *Let $R_1, R_2 \in \mathcal{G}$ and let n_1, n_2 denote the outer normal vectors associated with the domains $\Omega(R_1)$ and $\Omega(R_2)$, parametrized over the reference domain D. Then*

$$\|n_1 - n_2\|_{L^\infty(D)} \;\leq\; C\; \|R_1 - R_2\|_{W^{1,\infty}(D)}\,,$$

where $C = C(\gamma)\left(1 + \|R_1\|_{W^{1,\infty}(D)} + \|R_2\|_{W^{1,\infty}(D)}\right)$.

Proof. For the non normalized tangential directions we obtain pointwise for $i = 1, 2$

$$\left|\tau_\varphi^{(i)}\right|^2 \;=\; |R_i|^2 + |\partial_\varphi R_i|^2 \;\leq\; \|R_i\|^2_{W^{1,\infty}(D)}$$

and for the axial tangential

$$\begin{aligned}\left|\tau_s^{(i)}\right|^2 &= |\partial_s R_i|^2 + R_i^2\,|\partial_s e_r|^2 + L^2 + 2LR_i\langle \partial_s e_r, t\rangle \\ &\leq C(\gamma)\left(\|R_i\|^2_{W^{1,\infty}(D)} + 1\right).\end{aligned}$$

Due to the affinity of the tangential directions with respect to R, the estimate transfers to the differences

$$\left|\tau_\varphi^{(1)} - \tau_\varphi^{(1)}\right|^2 + \left|\tau_s^{(1)} - \tau_s^{(2)}\right|^2 \leq C(\gamma)\,\|R_1 - R_2\|^2_{W^{1,\infty}(D)}\,.$$

Therefore, we obtain for the differences of the non normalized outer directions

$$\begin{aligned}|\tilde{n}_1 - \tilde{n}_2| &\leq \left|\tau_\varphi^{(1)} \times \left(\tau_s^{(1)} - \tau_s^{(2)}\right)\right| + \left|\left(\tau_\varphi^{(1)} - \tau_\varphi^{(2)}\right) \times \tau_s^{(2)}\right| \\ &\leq C(\gamma)\left(1 + \|R_1\|_{W^{1,\infty}(D)} + \|R_2\|_{W^{1,\infty}(D)}\right)\|R_1 - R_2\|_{W^{1,\infty}(D)}\,.\end{aligned}$$

Finally, we obtain with the reverse triangle inequality and the estimate (2.39)

$$\begin{aligned}|n_1 - n_2| = \left|\frac{\tilde{n}_1}{|\tilde{n}_1|} - \frac{\tilde{n}_2}{|\tilde{n}_2|}\right| &\leq \frac{|\tilde{n}_1 - \tilde{n}_2|}{|\tilde{n}_1|} + |\tilde{n}_2|\left|\frac{1}{|\tilde{n}_1|} - \frac{1}{|\tilde{n}_2|}\right| \\ &= \frac{1}{|\tilde{n}_1|}\left(|\tilde{n}_1 - \tilde{n}_2| + |\,|\tilde{n}_2| - |\tilde{n}_1|\,|\right) \leq \frac{2}{|\tilde{n}_1|}|\tilde{n}_1 - \tilde{n}_2| \\ &\leq C(\gamma)\left(1 + \|R_1\|_{W^{1,\infty}(D)} + \|R_2\|_{W^{1,\infty}(D)}\right)\|R_1 - R_2\|_{W^{1,\infty}(D)}\,.\end{aligned}$$

□

This estimate is required for bounding the wall shear stress estimation error.

2.4 Continuous Analysis

In the final section of this chapter, we formally introduce and analyze the wall shear stress reconstruction strategy consisting of the three sub-problems:

(i) geometry reconstruction,

(ii) velocity approximation and

(iii) wall shear stress estimation.

For the stable solution of (i) and (ii) we utilize Tikhonov regularization. With some auxiliary results regarding the parametrization from Section 2.3 we formulate the problems in the framework of Section 2.2 and verify the conditional stability estimate. Finally, we combine the results to prove convergence rates of the wall shear stress estimate (iii) with respect to the data errors.

2.4.1 Geometry Reconstruction

We investigate the problem of reconstructing an approximation of the exact parametrization $R^\dagger$ with associated exact flow geometry $\Omega^\dagger$. For this purpose we utilize data $m^\delta \in L^2(\Omega_{\mathrm{FOV}})$ from magnetic resonance imaging. With χ denoting the characterstic function, the data are interpreted as

$$m^\delta \approx m := \chi_{\Omega^\dagger} = \begin{cases} 1 & \text{in } \Omega^\dagger, \\ 0 & \text{in } \Omega_{\mathrm{FOV}} \setminus \Omega^\dagger. \end{cases} \tag{2.40}$$

The corresponding geometry forward operator is

$$F : \mathcal{D}(F) \subset L^2(D) \to L^2(\Omega_{\mathrm{FOV}}), \quad F(R) \mapsto \chi_{\Omega(R)}, \tag{2.41}$$

where $\Omega(R)$ is the flow domain associated with geometry parameter R. To cast the problem in the framework of Subsection 2.2.3, we observe that $X = L^2(D)$, $Y = L^2(\Omega_{\mathrm{FOV}})$. For the domain $\mathcal{D}(F)$, we recall the parameter domain $D = \mathbb{S}^1$ (2D) respective $D = \mathbb{S}^1 \times (0,1)$ (3D) and the set of adimissible parameters $\mathcal{G} \subset \mathcal{C}^1(\overline{D})$ in (2.29) respective (2.36). We observe that $H^3(D) \hookrightarrow \mathcal{C}^1(D)$. With the bounds $0 < R_{\min} \leq R_{\max} \in \mathcal{C}(\overline{D})$ and some arbitrary constant $C > 0$ we introduce the domain

$$\mathcal{D}(F) := \left\{ R \in H^3(D) \mid R_{\max} \geq R \geq R_{\min} \right\}. \tag{2.42}$$

We summarize some important properties of F in the following lemma.

Lemma 2.23. *The operator F, defined in (2.41) and (2.42), is Hölder continuous with $\alpha = 1/2$, non-differentiable and satisfies the conditional stability estimate*

$$\|R_1 - R_2\|_{L^2(D)} \leq C \, \|F(R_1) - F(R_2)\|_{L^2(\Omega_{\mathrm{FOV}})} \quad \forall R_1, R_2 \in \mathcal{D}(F). \tag{2.43}$$

Proof. Hölder continuity follows directly from Lemma 2.14 by

$$\|F(R_1) - F(R_2)\|_{L^2(\Omega_{\mathrm{FOV}})} = \|\chi_1 - \chi_2\|^{1/2}_{L^1(\Omega_{\mathrm{FOV}})} \leq C \|R_1 - R_2\|^{1/2}_{L^1(D)} \leq C \|R_1 - R_2\|^{1/2}_{L^2(D)}.$$

This estimate is optimal, in the sense that for $R \in \mathcal{G}$ and $t > 0$

$$\|F(R+t) - F(R)\|_{L^2(\Omega_{\mathrm{FOV}})} = \|\chi_{\Omega(R+t)} - \chi_{\Omega(R)}\|^{1/2}_{L^1(\Omega_{\mathrm{FOV}})} \geq C \, t^{1/2}.$$

This reveals, that F is nowhere differentiable. However, we have by Lemma 2.15 for arbitrary $R_1, R_2 \in \mathcal{D}(F)$

$$\|F(R_1) - F(R_2)\|_{L^2(\Omega_{\mathrm{FOV}})} = \|\chi_1 - \chi_2\|^{1/2}_{L^1(\Omega_{\mathrm{FOV}})} \geq C \|R_1 - R_2\|_{L^2(D)}.$$

Hence, F satisfies the announced conditional stability estimate. □

Lemma 2.23 establishes Assumption 2.5, which was the crucial ingredient for our analsys of Tikhonov regularization in Subsection 2.2.3. For the solution of the inverse problem

$$\text{Find } R \in \mathcal{D}(F) \text{ with } F(R) = m^\delta \tag{2.44}$$

we utilize Tikhonov regularization with the functional

$$\mathcal{T}^\delta_\alpha(R) := \left\| F(R) - m^\delta \right\|^2_{L^2(\Omega_{\mathrm{FOV}})} + \alpha \, |R|^2_{H^3(D)}$$

and consider $R^\delta_\alpha \in \mathcal{M}^\delta_\alpha := \{R \in \mathcal{D}(F) \mid \mathcal{T}^\delta_\alpha(R) \leq \inf_{\tilde{R} \in \mathcal{D}(F)} \mathcal{T}^\delta_\alpha(\tilde{R})\}$. By application of Theorem 2.8 we immediately obtain the following result.

Theorem 2.24. *Let $R^\dagger \in \mathcal{D}(F)$, $m^\delta \in Y$ with $\|m^\delta - F(R^\dagger)\|_Y \leq \delta$. Let $R_\alpha^\delta \in \mathcal{M}_\alpha^\delta$ be an approximate Tikhonov minimizer for $\alpha(\delta) = \delta^2/M^2$ with some $M \geq |R^\dagger|_{H^3(D)}$. Then*

$$\left\|R_\alpha^\delta - R^\dagger\right\|_{H^s(D)} \leq C\,\delta^{1-s/3}\,(\delta + M)^{s/3} \quad \forall\, 0 \leq s \leq 3.$$

The same estimate with $M := \max\{|R^\dagger|_{H^3(D)}, \delta/\sqrt{\alpha_{\max}}\}$ holds for the a posteriori choice $\alpha = \alpha(\delta, m^\delta)$ given by the discrepancy principle (2.27).

Remark 2.25. Since F is not differentiable, the standard result about convergence rates for Tikhonov regularization, given in Proposition 2.2, is not applicable. However, the conditional stability approach by Cheng and Yamamoto yields convergence of the reconstruction with a certain rate with respect to the data error. The conditional stability estimate is valid and $R^\dagger \in \mathcal{D}(F)$ is reasonable, since it poses only mild assumptions on the exact geometry. Additional source conditions ore non-linearity conditions are not required. Compared to regularization in the full norm $\|\cdot\|_{H^3(D)}$, the regularization in the seminorm pays off for nearly circular (2D) and cylindrical (3D) geometries with roughly constant geometry parameter $R^\dagger$: For $|R^\dagger|_{H^3(D)} \leq \delta$ we obtain $\|R_\alpha^\delta - R^\dagger\|_{H^3(D)} \leq C\delta$ without additional bias.

2.4.2 Velocity Approximation

Now we turn to sub-problem (ii), the approximation of the flow velocity. Magnetic resonance velocimetry provides spatially resolved measurements u^ε of the exact flow velocity $u^\dagger$. However, the estimation of wall shear stress requires approximations of the velocity derivatives at the boundary of the flow domain. While this amounts to a standard ill-posed problem [29], there is an additional difficulty: The velocity outside the flow domain is zero, resulting in a discontinuous derivative. Hence, we have to introduce a novel framework for the approximation of the flow velocity, taking into account, that only approximations R^δ on the flow geometry with geometry parameter $R^\dagger$ are available. The framework is based on the extension of the parametrization R of the boundary to domain transformations Φ_R, mapping a reference flow domain $\widehat{\Omega}$ to the flow domain Ω_R, that were introduced in Subsection 2.3.4.

We cast the velocity approximation problem in the setting of Subsection 2.2.3: The available velocity data $u^\varepsilon \in L^2(\Omega_{\mathrm{FOV}})$ are interpreted as

$$u^\varepsilon \approx \begin{cases} u^\dagger & \text{in } \Omega^\dagger, \\ 0 & \text{in } \Omega_{\mathrm{FOV}} \setminus \Omega^\dagger, \end{cases} \tag{2.45}$$

where $u^\dagger$ is the velocity in the physical flow domain. We can associate a function $u : \Omega \to \mathbb{R}^d$ on the physical domain, parametrized by $R \in \mathcal{G}$ as defined in (2.29) respective (2.36), with a function $v : \widehat{\Omega} \to \mathbb{R}^d$ on the reference domain by composition with the corresponding domain transformation $\Phi_R : \widehat{\Omega} \to \Omega$. We aim for an approximation of the mapped exact flow velocity

$$v^\dagger := u^\dagger \circ \Phi^\dagger.$$

With the approximate geometry parameter R we introduce the velocity measurement operator

$$T : \mathcal{D}(T) \subset L^2(\widehat{\Omega}) \to L^2(\Omega_{\mathrm{FOV}}), \quad Tv := E_R(v \circ \Psi_R),$$

where $E_R : L^2(\Omega_R) \to L^2(\Omega_{\mathrm{FOV}})$ is the extension by zero and $\Psi_R : \Omega_R \to \widehat{\Omega}$ the inverse transformation associated with R. Note that $T = T_R$ depends on the geometry parameter, where we use the notation T_R only, when it matters. We require stable evaluation of the normal derivative, therefore we introduce

$$\mathcal{D}(T) := \left\{ v \in H^2(\widehat{\Omega}) \mid v = 0 \text{ on } \widehat{\Gamma}_W = \{1\} \times \mathcal{S}^1 \times (0,1) \right\}. \tag{2.46}$$

This corresponds to the setting of Subsection 2.2.3 with $X = L^2(\widehat{\Omega})$, $\mathcal{D}(T) \subseteq H^2(\widehat{\Omega})$ and $Y = L^2(\Omega_{\mathrm{FOV}})$. Concerning the dependence on the geometry parametrization, we have the following stability result.

Lemma 2.26. *Let $v \in \mathcal{D}(F) \cap \mathcal{C}^1(\overline{\widehat{\Omega}})$ and let $R_1, R_2 \in \mathcal{G}$. Let T_1, T_2 denote the velocity measurement operators associated with R_1, R_2. Then*

$$\|T_1(v) - T_2(v)\|_{L^2(\Omega_{\mathrm{FOV}})} \leq C \, \|v\|_{W^{1,\infty}(\widehat{\Omega})} \, \|R_1 - R_2\|_{L^\infty(D)}$$

with constant C depending only on $\|R_1\|_{W^{1,\infty}(D)}$ and $\|R_2\|_{W^{1,\infty}(D)}$.

Proof. We divide the error $e := T_1(v) - T_2(v)$ into the contributions

$$\|e\|_Y \leq \|e\|_{L^2(\Omega_1 \cap \Omega_2)} + \|e\|_{L^2(\Omega_1 \setminus \Omega_2)} + \|e\|_{L^2(\Omega_2 \setminus \Omega_1)} + \|e\|_{L^2(\Omega_{\mathrm{FOV}} \setminus (\Omega_1 \cup \Omega_2))}.$$

With the associated inverse transformations Ψ_1 and Ψ_2, the first contribution on the shared domain is estimated using Lemma 2.20

$$\begin{aligned} \|T_1(v) - T_2(v)\|_{L^2(\Omega_1 \cap \Omega_2)} &= \|v \circ \Psi_1 - v \circ \Psi_2\|_{L^2(\Omega_1 \cap \Omega_2)} \\ &\leq \|v\|_{W^{1,\infty}(\widehat{\Omega})} \, \|\Psi_1 - \Psi_2\|_{L^\infty(\Omega_1 \cap \Omega_2)} \, |\Omega_1 \cap \Omega_2|^{1/2} \\ &\leq C \, \|v\|_{W^{1,\infty}(\widehat{\Omega})} \, \|R_1 - R_2\|_{L^\infty(D)}. \end{aligned}$$

For the second part let $x \in \Omega_1 \setminus \Omega_2$. Switching to the parametric representation we have $x = \gamma(s) + r e_r(\varphi, s)$ with $R_2(\varphi, s) \leq r < R_1(\varphi, s)$. Set $x_b = \gamma(s) + R_1(\varphi, s) e_r(\varphi, s)$. Then $\Psi_1(x_b) \in \widehat{\Gamma}_W$ and since $v \in \mathcal{D}(F) \cap \mathcal{C}^1(\overline{\widehat{\Omega}})$

$$\begin{aligned} |(v \circ \Psi_1)(x)| &= |(v \circ \Psi_1)(x) - (v \circ \Psi_1)(x_b)| \\ &= \left| \int_0^1 \partial_r (v \circ \Psi_1)(x_b + \xi(x - x_b)) \, (R(\varphi, s) - r) \, \mathrm{d}\xi \right| \\ &\leq \|v\|_{W^{1,\infty}(\widehat{\Omega})} \, \|\Psi_1\|_{W^{1,\infty}(\Omega_1)} \, |R_1(\varphi, s) - R_2(\varphi, s)|. \end{aligned}$$

Finally, we estimate the second part by Lemma 2.14 and Lemma 2.20

$$\begin{aligned}\|T_1(v) - T_2(v)\|_{L^2(\Omega_1 \setminus \Omega_2)} &= \|v \circ \Psi_1\|_{L^2(\Omega_1 \setminus \Omega_2)} \\ &\leq C_R \|v\|_{W^{1,\infty}(\widehat{\Omega})} \|R_1 - R_2\|_{L^\infty(D)} \, |\Omega_1 \setminus \Omega_2|^{1/2} \\ &\leq C_R \|v\|_{W^{1,\infty}(\widehat{\Omega})} \|R_1 - R_2\|^{3/2}_{L^\infty(D)}.\end{aligned}$$

The estimation of the third part follows analogously by swapping the roles of R_1 and R_2. The assertion follows, since both images are zero on the last part. □

Let $R \in \mathcal{G}$, where $\mathcal{G}$ is given by (2.29) respective (2.36), be an approximation of the exact geometry parameter $R^\dagger \in \mathcal{G}$. For the solution of the inverse problem

$$\text{Find } v \in \mathcal{D}(T) \text{ with } Tv = u^\varepsilon \tag{2.47}$$

we utilize Tikhonov regularization with the functional

$$\mathcal{T}^\varepsilon_\beta(v) \;:=\; \|Tv - u^\varepsilon\|^2_{L^2(\Omega_{\mathrm{FOV}})} \;+\; \beta \; |v|^2_{H^2(\widehat{\Omega})}$$

and consider $v^\varepsilon_\beta \in \mathcal{M}^\varepsilon_\beta = \{v \in \mathcal{D}(F) \mid \mathcal{T}^\varepsilon_\beta(v) \leq \inf_{\tilde{v} \in \mathcal{D}(F)} \mathcal{T}^\varepsilon_\beta(\tilde{v})\}$. Applying auxiliary results about the parameterization with the stability result of Lemma 2.26, we obtain a bound on the data error with perturbed forward operator. The combination with the theory about Tikhonov regularization finally leads to a convergent velocity approximation.

Proposition 2.27. *Let $R \in \mathcal{G}$ and $R^\dagger \in \mathcal{G} \cap \mathcal{C}^3(\overline{D})$ with $\delta_R := \|R^\dagger - R^*\|_{L^\infty(D)}$. Let $u^\dagger \in H^3(\Omega^\dagger)$ with $u^\dagger = 0$ on $\Gamma^\dagger_W$. Let $u^\varepsilon \in L^2(\Omega_{FOV})$ with $\|E^\dagger u^\dagger - u^\varepsilon\|_{L^2(\Omega_{\mathrm{FOV}})} \leq \varepsilon$. Then $v^\dagger := u^\dagger \circ \Phi^\dagger \in \mathcal{D}(F) \cap \mathcal{C}^1(\overline{\widehat{\Omega}})$ and*

$$\left\|Tv^\dagger - u^\varepsilon\right\|_{L^2(\Omega_{\mathrm{FOV}})} \leq C \, \delta_R \, \|v^\dagger\|_{W^{1,\infty}(\widehat{\Omega})} + \varepsilon =: \varepsilon_U$$

with constant C depending only on $\|R\|_{W^{1,\infty}(D)}$ and $\|R^\dagger\|_{W^{1,\infty}(D)}$.
Further, let $v^\varepsilon_\beta \in \mathcal{M}^\varepsilon_\beta$ be an approximate Tikhonov minimizer for $\beta(\varepsilon_U) = \varepsilon_U^2/M^2$ with some $M \geq |v^\dagger|_{H^2(\widehat{\Omega})}$. Then

$$\left\|v^\varepsilon_\beta - v^\dagger\right\|_{H^s(D)} \;\leq\; C \, \varepsilon_U^{1-s/2} \; (\varepsilon_U + M)^{s/2} \quad \forall \, 0 \leq s \leq 2.$$

The same estimate with $M := \max\{|v^\dagger|_{H^2(\widehat{\Omega})}, \varepsilon_U/\sqrt{\beta_{\max}}\}$ holds for the a posteriori choice $\beta = \beta(\varepsilon_U, u^\varepsilon)$ given by the discrepancy principle (2.27).

Proof. We split the proof in 3 steps.

Step 1: Admissibility and regularity of $v^\dagger$. For any composition $h = f \circ g$ of smooth functions f and g, we have $Dh = (Df \circ g)Dg$. By elementary calculus using the chain and product rule, we estimate pointwise

$$\left\|D^k h\right\|(x) \leq C \left(\|g\|_{W^{k,\infty}} + \|g\|^k_{W^{k,\infty}}\right) \sum_{l=1}^{k} \left\|D^l f \circ g\right\|(x).$$

Applying $v^\dagger = u^\dagger \circ \Phi^\dagger$ with $\Phi^\dagger \in W^{3,\infty}(\widehat{\Omega})$ according to Lemma 2.18 yields for $k \leq 3$ with some constant C depending on $\|\Phi^\dagger\|_{W^{3,\infty}(\widehat{\Omega})}$ that

$$\begin{aligned}\int_{\widehat{\Omega}} \|D^k v^\dagger\|^2 \,\mathrm{d}\hat{x} &\leq C \int_{\widehat{\Omega}} \sum_{l=1}^{k} \left\|D^l u^\dagger \circ \Phi^\dagger\right\|^2 \,\mathrm{d}\hat{x} \\ &= C \int_{\Omega^\dagger} \det(D\Psi^\dagger) \sum_{l=1}^{k} \left\|D^l u^\dagger\right\|^2 \,\mathrm{d}x \\ &\leq C \left\|u^\dagger\right\|^2_{H^3(\Omega^\dagger)}.\end{aligned}$$

Since $\Phi^\dagger(\widehat{\Gamma}_W) = \Gamma_W^\dagger$, we have $v^\dagger = 0$ on $\widehat{\Gamma}_W$ and therefore $v^\dagger \in \mathcal{D}(T)$ for sufficiently large upper bound.

Step 2: Estimating the data error. We verify using Lemma 2.26

$$\begin{aligned}\left\|Tv^\dagger - u^\varepsilon\right\|_Y &\leq \left\|T_R v^\dagger - T^\dagger v^\dagger\right\|_Y + \left\|T^\dagger v^\dagger - u^\varepsilon\right\|_Y \\ &\leq C \left\|v^\dagger\right\|_{W^{1,\infty}(\widehat{\Omega})} \|R - R^\dagger\|_{L^\infty(D)} + \left\|E^\dagger u^\dagger - u^\varepsilon\right\|_Y \\ &= C \left\|v^\dagger\right\|_{W^{1,\infty}(\widehat{\Omega})} \delta_R + \varepsilon \\ &= \varepsilon_U.\end{aligned}$$

Step 3: Conditional stability estimate. T fulfills a conditional stability estimate, since with $v_1, v_2 \in \mathcal{D}(T)$ we have

$$\begin{aligned}\|Tv_1 - Fv_2\|_Y^2 &= \int_{\Omega^*} |v_1 \circ \Psi^* - v_2 \circ \Psi^*|^2 \,\mathrm{d}x \\ &= \int_{\widehat{\Omega}} |\det(D\Phi^*)| \, |v_1 - v_2|^2 \,\mathrm{d}\hat{x} \\ &\geq C \|v_1 - v_2\|_{L^2(\widehat{\Omega})}.\end{aligned}$$

Thus, the assertions follow by applying Theorem 2.8. □

Combining these results with the geometry reconstruction from the previous section, we arrive at the following conclusions.

Theorem 2.28. *Let $v_{\alpha,\beta}^{\delta,\varepsilon} \in \mathcal{D}(\mathcal{F})$ be the velocity approximation according to Proposition 2.27 based on the geometry reconstruction $R^* = R_\alpha^\delta \in \mathcal{G}$ according to Remark 2.25. Then we have*

$$\left\|v_{\alpha,\beta}^{\delta,\varepsilon} - v^\dagger\right\|_{H^s(\widehat{\Omega})} \leq C_U \left[C \left\|u^\dagger\right\|_{W^{1,\infty}(\Omega^\dagger)} \delta + \varepsilon\right]^{1-s/2} \quad \forall 0 \leq s \leq 2,$$

with constant C depending only on $\|R^\dagger\|_{W^{3,\infty}(D)}$ and constant C_U depending on $\|u^\dagger\|_{H^3(\Omega^\dagger)}$.

Before we close this subsection about the velocity approximation, let us briefly make some comments on the main results of our analysis so far.

Remark 2.29. As for the geometry reconstruction, we have derived convergence with a certain rate under the reasonable assumption, that the velocity $u^\dagger$ is smooth and satisfies the no-slip condition. The computation of the error ε_U, that is needed for the reconstruction, requires knowledge of the size $\|v^\dagger\|_{W^{1,\infty}(\widehat{\Omega})}$ of the true velocity field, the velocity data error and the geometry reconstruction error. Since the forward operator is linear with respect to the velocity variable, similar results are obtainable from the standard theory [29].
Let us note that the derived convergence rate is not optimal. An enhanced result can be derived in the linear theory [29] or alternatively in the conditional stability analysis in Hilbert scales [23]. However, the enhancement is based on additional source conditions, i.e. artificial boundary conditions on $v^\dagger$, that are only satisfied in a limited degree [25, 64]. In contrast to the radius function $R^\dagger$, the velocity field $u^\dagger$ and consequently $v^\dagger$ exhibits high derivatives due to the presence of boundary layers. Therefore, we mark the dependence on $\|u^\dagger\|_{H^m(\Omega^\dagger)}$. The mismatch in the geometry δ_R highly affects the data error ε_U, since the mismatch is amplified with $\|v^\dagger\|_{W^{1,\infty}(\widehat{\Omega})}$.

2.4.3 Wall Shear Stress Estimation

As a final step of our reconstruction process, we now present the estimation of wall shear stress from the geometry reconstruction and the velocity approximation. Finally, we prove the stability of the estimate with respect to the previously considered reconstruction norms.

The true wall shear stress $\tau^\dagger : \Gamma^\dagger \to \mathbb{R}^d$ is defined on the boundary $\Gamma^\dagger$ of the exact physical domain, which is parametrized by $R^\dagger$. The straightforward reconstruction $\tau : \Gamma \to \mathbb{R}^d$ is defined on the boundary of the reconstructed domain, which is parametzied by R. To allow for a comparison of both estimates, we map the wall shear stress on the wall part $\widehat{\Gamma}_W$ of the surface of the reference domain. Like it was already used for the outer normal in Subsection 2.3.5, we may identify $\widehat{\Gamma}_W$ with $D = \mathcal{S}^1 \times (0,1)$. Hence, we obtain the mapped exact wall shear stress

$$\widehat{\tau}^\dagger : D \to \mathbb{R}^d, \quad \widehat{\tau}^\dagger \;=\; \tau^\dagger \circ \Phi^\dagger \;=\; -\mu\, Dv^\dagger\, (D\Phi^\dagger)^{-1}\, n^\dagger. \tag{2.48}$$

The mapped estimated wall shear stress, that is obtained from geometry parameter R and approximate velocity v, is given by

$$\widehat{\tau} : D \to \mathbb{R}^d, \quad \widehat{\tau} \;=\; \tau \circ \Phi \;=\; -\,\mu\, Dv\, (D\Phi)^{-1}\, n, \tag{2.49}$$

where Φ and n are the geometry transformation respective outer normal corresponding to R. Regarding the difference, we obtain the following stability result.

Proposition 2.30. *Let $R^\dagger, R \in \mathcal{G}$ with $\|R^\dagger - R\|_{W^{1,\infty}(D)} \leq \delta$. Let $v^\dagger, v \in H^s(\widehat{\Omega})$ with $\|v^\dagger - v\|_{H^s(\widehat{\Omega})} \leq \varepsilon$ and $u^\dagger = v^\dagger \circ \Psi^\dagger \in H^s(\Omega^\dagger)$ for some $s > 3/2$. Then the corresponding mapped wall shear stress estimates given by (2.48) and (2.49) satisfy*

$$\|\widehat{\tau}^\dagger - \widehat{\tau}\|_{L^2(D)} \;\leq\; C\, \left(\|u^\dagger\|_{H^s(\Omega^\dagger)}\, \delta + \varepsilon \right)$$

with constant C depending only on μ and the norms of R^* and $R^\dagger$.

Proof. We split

$$\begin{aligned}
\left\|\widehat{\tau} - \widehat{\tau}^\dagger\right\|_{L^2(D)} &= \mu \left\| Dv \left(D\Phi\right)^{-1} n \,-\, Dv^\dagger \left(D\Phi^\dagger\right)^{-1} n^\dagger \right\|_{L^2(D)} \\
&= \mu \left\| Dv \left(D\Phi\right)^{-1} n \,-\, Dv^\dagger \left(D\Phi^\dagger\right)^{-1} n^\dagger \right\|_{L^2(D)} \\
&\leq \mu \left\| Dv^\dagger \left(D\Phi^\dagger\right)^{-1} \left[n - n^\dagger\right] \right\|_{L^2(D)} \\
&\quad + \mu \left\| Dv^\dagger \left[\left(D\Phi\right)^{-1} - \left(D\Phi^\dagger\right)^{-1} \right] n \right\|_{L^2(D)} \\
&\quad + \mu \left\| \left[Dv - Dv^\dagger\right] \left(D\Phi\right)^{-1} n \right\|_{L^2(D)} \\
&= (i) + (ii) + (iii).
\end{aligned}$$

For the first term, we obtain using the regularity of $v^\dagger$, Lemma 2.20 and the error estimate for the normal direction of Lemma 2.22

$$\begin{aligned}
(i) &\leq \mu \left\|Dv^\dagger\right\|_{L^2(D)} \left\| \left(D\Phi^\dagger\right)^{-1} \right\|_{L^\infty(D)} \left\|n - n^\dagger\right\|_{L^\infty(D)} \\
&\leq C \left\|v^\dagger\right\|_{H^s(\widehat{\Omega})} \left\|R^\dagger\right\|_{W^{1,\infty}(D)} \left\|R - R^\dagger\right\|_{W^{1,\infty}(D)} \\
&\leq C \left\|u^\dagger\right\|_{H^s(\Omega^\dagger)} \delta.
\end{aligned}$$

Using the error estimate for the inverse Jacobians of Lemma 2.20, we obtain

$$\begin{aligned}
(ii) &\leq \mu \left\|Dv^\dagger\right\|_{L^2(D)} \left\| \left(D\Phi\right)^{-1} - \left(D\Phi^\dagger\right)^{-1} \right\|_{L^\infty(D)} \|n\|_{L^\infty(D)} \\
&\leq C \left\|v^\dagger\right\|_{H^s(\widehat{\Omega})} \left\|R - R^\dagger\right\|_{W^{1,\infty}(D)} \\
&\leq C \left\|u^\dagger\right\|_{H^s(\Omega^\dagger)} \delta.
\end{aligned}$$

Finally we estimate the velocity mismatch term

$$\begin{aligned}
(iv) &\leq \mu \left\|Dv - Dv^\dagger\right\|_{L^2(D)} \left\|\left(D\Phi\right)^{-1}\right\|_{L^\infty(D)} \|n\|_{L^\infty(D)} \\
&\leq C \left\|v - v^\dagger\right\|_{H^s(\widehat{\Omega})} \|R\|_{W^{1,\infty}(D)} \\
&\leq C\,\varepsilon.
\end{aligned}$$

□

If the wall shear stress is reconstructed sequentially using the previously introduced geometry reconstruction and velocity approximation, we can combine the estimates of the reconstruction errors and obtain the following main result.

Theorem 2.31. *Let $v_{\alpha,\beta}^{\delta,\varepsilon} \in H^2(\widehat{\Omega})$ be the velocity approximation according to Theorem 2.28, based on the geometry reconstruction $R_\alpha^\delta \in \mathcal{G}$ according to Remark 2.25, computed from*

geometry and velocity measurements with errors δ and ε, respectively. Let $\tau_{\alpha,\beta}^{\delta,\varepsilon}$ be the associated wall shear stress estimator. Then we have

$$\left\|\widehat{\tau}_{\alpha,\beta}^{\delta,\varepsilon} - \widehat{\tau}^{\dagger}\right\|_{L^2(D)} \leq C \left\|u^{\dagger}\right\|_{H^2(\Omega^{\dagger})} \delta + C_U \left[\left\|u^{\dagger}\right\|_{W^{1,\infty}(\Omega^{\dagger})} \delta + \varepsilon\right]^s$$

for every $s < 1/4$ with constant C depending only on $\|R^{\dagger}\|_{W^{3,\infty}(D)}$ and the viscosity μ and constant C_U additionally depending on $\|u^{\dagger}\|_{H^3(\Omega^{\dagger})}$.

Summary: We have derived a purely data driven wall shear stress estimator, that is applicable to various flows satisfying some basic fluid dynamical properties. We take advantage of the *a priori* knowledge about the topology of the flow domain, to introduce a parametric representation of the geometry. This enables to formulate the reconstruction of the necessary ingredients, the flow geometry from the magnitude data and the flow velocity from the velocity data, as inverse problems posed in a Hilbert space setting. Unfortunately, the forward operator of the geometry reconstruction problem renders non-differentiable, preventing an analysis of the inverse problem by standard techniques. However, a modification of an alternative approach using a conditional stability estimate proved to be applicable and allows for a convergence analysis of the reconstruction purely on reasonable smoothness assumptions. Combining these results allows for quantifying the wall shear stress estimation error in terms of the measurement errors, setting this method apart from the other data driven wall shear stress estimators.

Although the concrete convergence rate may be of minor importance, since the measurement errors cannot be arbitrarily reduced, it guarantees robustness of the estimators. Furthermore, the analysis reveals, that errors of the geometry registration are amplified with norms of derivatives of the velocity field, that are considerably large due to the presence of boundary layers in the investigated flow regimes. Consequently, the data driven wall shear stress estimation relys on a highly accurate geometry reconstruction.

In the following chapter, we consider a more detailed model of the discrete measurement operator, to reduce the data error and consequently reconstruction errors, and apply the method to several relevant flow regimes.

Chapter 3

Numerical Realization and Validation

In the previous chapter, we have developed a purely data based technique to estimate the wall shear stress. The method sequentially solves the sub-problems:

(i) reconstruction of the flow geometry $\Omega^\dagger$,

(ii) approximation of the flow velocity $u^\dagger$ and

(iii) calculation of the wall shear stress $\tau^\dagger$.

A parametric representation was used in all steps and for the stable solution of (i) and (ii) we utilized Tikhonov regularization. Based on a conditional stability estimate, that could be verified for the forward operators of (i) and (ii), we proved error estimates for the reconstruction in terms of the data errors. For the theoretical analysis of this approach, we investigated an idealized measurement operator with infinite data resolution. However, for the clinical application with only limited data resolution, the data acquisition process becomes more complicated. Therefore, in Section 3.1 we present a more detailed modelling of the data and derive corresponding bounds on the data error in terms of accessible quantities.

Subsequently, we present the numerical realization of the method. The straightforward discretization of the geometry and velocity measurement operators would lead to forward operators that are inconsistent with the previously derived data model and even non-differentiable in case of the geometry measurement, preventing an efficient numerical solution of the associated Tikhonov minimization problem. Hence, we introduce suitable modifications of the forward operators in Section 3.2. With these modifications we arrive at a fully discrete method and expect to obtain

- stable reconstructions with the approximation errors bounded in terms of the data error, since in view of Proposition 2.10 the computed solutions are approximate Tikhonov minimizers of the idealized measurement operator, provided the modification is sufficiently small, and

- reasonable reconstructions for the practically feasible, but considerably low data resolution, since the modified forward operators are conforming with the data model.

For the verification of these expectations, in Section 3.3 we perform a comprehensive validation by applying the method to several measurements *in silico* with simulated data and measurements *in vitro* with physical data, acquired from a highly controlled experimental flow. Since for these measurements *ground truth*, i.e. exact data $\Omega^\dagger$, $u^\dagger$ and $\tau^\dagger$, is available, we can compute the reconstruction errors, allowing for assessing the performance of our method. We conclude the chapter with illustrative applications to more complex problems, where we only check plausibility in lack of accurate reference values.

This chapter is based on our collaborative work with the project partners, in particular with the Department of Radiology in Freiburg, and major results are published in [86].

3.1 The Discrete Measurement

Although the interpretation of the data used in the previous chapter represents the limit of infinite data resolution, in the discrete case we should use an adapted data model. In the following subsection, we postulate the model and corresponding error bounds. A detailed derivation including the necessary pre-processing techniques is presented subsequently.

3.1.1 Modelling of the Discrete Measurements

Phase contrast magnetic resonance imaging allows to obtain spatially and possibly temporally resolved measurements of flow geometries and velocities. The data provided by magnetic resonance imaging or velocimetry are given on a regular grid $(V_i)_{i=1,\dots,N_V}$ of the field of view Ω_{FOV}. The N_V voxels V_i are assumed to be squares (2D) or cubes (3D) of the same length $h > 0$. The MR measurements of magnitudes m^δ and velocities u^ε can be interpreted as piecewise constant functions in $L^2(\Omega_{\mathrm{FOV}})$, defined by

$$m^\delta = \sum_{i=1}^{N_V} m_i^\delta \, \chi_{V_i}(x), \quad u^\varepsilon = \sum_{i=1}^{N_V} u_i^\varepsilon \chi_{V_i}(x).$$

Let us now comment in a bit more detail on the actual information content of the data. We postulate that the magnitude data are the fraction of the voxel occupied by the flow domain $\Omega^\dagger \subset \Omega_{\mathrm{FOV}}$

$$m_i^\delta \;=\; \frac{\left|\Omega^\dagger \cap V_i\right|}{|V_i|} + \nu_i^\delta \tag{3.1}$$

with data error $\nu^\delta = \sum_i \nu_i^\delta \chi_{V_i}$. In a similar manner, we assume that the exact velocity field $u^\dagger \in W^{1,\infty}(\Omega_{\mathrm{FOV}})$ leads to measurments

$$u_i^\varepsilon \;=\; \frac{1}{|V_i|} \int\limits_{V_i \cap \Omega^\dagger} u^\dagger(x)\,\mathrm{d}x + \nu_i^\varepsilon \tag{3.2}$$

with data error $\nu^\varepsilon = \sum_i \nu_i^\varepsilon \chi_{V_i}$. Assume that the measurement process is fast in comparison to changes in the physical fields and hence the data can be understood as snapshots of the physical fields on a uniform grid in time.

To quantify the data errors, we introduce some quantities: Let SNR and CNR denote the *signal-to-noise ratio* and *contrast-to-noise ratio*, respectively, that are approximately accessible from the data [60]. Let v_{enc} denote the velocity encoding - a controllable parameter of the data acquisition process. Then for sufficiently high data resolution h we have the estimate

$$\|\nu^\delta\|_{L^2(\Omega_{\text{FOV}})} \leq C \frac{\sqrt{h}}{\text{CNR}} \left(1 + \frac{|u^\dagger|^2_{W^{1,\infty}(\Omega^\dagger)}}{v_{\text{enc}}^2} h \,\text{SNR}\right). \tag{3.3}$$

For the velocity data it holds

$$\|\nu^\varepsilon\|_{L^2(\Omega_{\text{FOV}})} \leq C\, v_{\text{enc}} \left(\frac{1}{\text{SNR}} + \frac{|u^\dagger|_{W^{1,\infty}(\Omega^\dagger)}}{v_{\text{enc}}} h^{3/2}\right). \tag{3.4}$$

Note that the geometry error vanishes for increasingly high data resolution, while the velocity error saturates at $v_{\text{enc}}/\text{SNR}$.

In the following subsection, we give an overview of the physical principles underlying the measurement technique and derive a mathematical model for the raw data. The data m^δ and u^ε are normalized data that are obtained after a pre-processing from the raw data. The pre-processing is outlined in Subsection 3.1.3, finally justifying the proposed estimates (3.3) and (3.4) of the data errors.

3.1.2 A Model for the Raw Data of Phase Contrast Magnetic Resonance Imaging

Here, we present a brief overview of the physics of phase contrast magnetic resonance imaging, for details we refer to [15]. Magnetic resonance imaging is based on the following principle: using a homogeneous static magnetic field and varying secondary magnetic fields, one generates Larmor precession of the magnetic spins associated with hydrogen atoms, i.e. protons. Special velocity encoding gradients are applied to obtain a phase shift of the moving spins which is proportional to the local flow velocity. The velocity encoding parameter v_{enc} controls this proportionality and its values for every direction are manually chosen before the measurement. The precessing magnetization becomes observable by inducing an alternating electric field in a receiver coil with the characteristic Larmor frequency. In fact, the measured data are the first modes of the spatial Fourier transformation in a cross-section (k-space), which are conducted sequentially line by line, one line at every pulse sequence repetition.

One can conduct measurements of one, two or all three velocity components, of only a single 2D rectangle or a 3D cuboid, and of a stationary or a non-stationary regime. Feasibile times for acquiring a single line in the k-space, the so called repetition time, are

about $10 - 50$ms [8]. Note that for temporally resolved measurements, the flow regime is assumed to be periodic and the scanner requires a trigger signal at the start of each period.

Let $u^\dagger$ denote a velocity component that we want to measure. Recapitulating the physical principles, we have the following imagination of the magnetic signal in the field of view:

$$c : \Omega_{\mathrm{FOV}} \to \mathbb{C}, \quad c(x) = \rho(x)\, e^{i\pi u^\dagger(x)/v_{\mathrm{enc}}}.$$

Here, ρ is the possibly discontinuous signal density that depends, amongst others, on the proton density, the relaxation time and the niveau of magnetic saturation. After transformation to the physical space, this amounts to a convolution of the signal with a smoothing sinc-kernel. We make the commonly used assumption [3] that the data are obtained with a rectangular kernel, hence

$$c_i \;=\; \frac{1}{|V_i|} \int\limits_{V_i} c(x)\,\mathrm{d}x + \nu_i^c, \quad i = 1, ..., N_V, \tag{3.5}$$

where V_i are the individual voxels and $\nu^c \in L^2(\Omega_{\mathrm{FOV}}; \mathcal{C})$ is the measurement noise. The magnetic resonance raw data, consisting of the raw magnitude $\overline{m}_i^\delta$ and the raw velocity $\overline{u}_i^\varepsilon$, are obtained by computing the polar representation of the complex data c_i:

$$\overline{m}_i^\delta \;:=\; |c_i|\,, \quad \overline{u}_i^\varepsilon \;:=\; \frac{v_{\mathrm{enc}}}{\pi}\, \arg(c_i), \qquad i = 1, ..., N_V.$$

Note that here and in the following, we associate a vector f_i with a piecewise constant function $f = \sum_i f_i \chi_{V_i} \in L^2(\Omega_{\mathrm{FOV}})$. To simplify the model of the measurement process, we introduce the following idealizations $\overline{m}$ and $\overline{u}$ for the magnitude and velocity data, respectively:

$$\overline{m}_i \;:=\; \frac{1}{|V_i|} \int\limits_{V_i} \rho(x)\,\mathrm{d}x \text{ and } \overline{u}_i \;:=\; \frac{1}{\int\limits_{V_i} \rho(x)\,\mathrm{d}x} \int\limits_{V_i} \rho(x) u^\dagger(x)\,\mathrm{d}x. \tag{3.6}$$

Since $u^\dagger \in W^{1,\infty}(\Omega_{\mathrm{FOV}})$ and obviously $\min_{x\in V_i} u^\dagger(x) \le \overline{u}_i \le \max_{x\in V_i} u^\dagger(x)$, there is $\xi_i \in V_i$ with $u^\dagger(\xi_i) = \overline{u}_i$ by the intermediate value theorem. For voxel size h, we thus obtain

$$\left\| u^\dagger - \overline{u}_i \right\|_{L^\infty(V_i)} \;\le\; C\, \left| u^\dagger \right|_{W^{1,\infty}(\Omega_{\mathrm{FOV}})}\, h. \tag{3.7}$$

For the following computations we assume that the voxel size is sufficiently small. Before we quantify the errors for the raw data model, we recall the *signal-to-noise ratio* (SNR), that plays an important role in the estimation of data accuracy. We define

$$\mathrm{SNR}_i \;:=\; \overline{m}_i / |\nu_i^c|.$$

In the following analysis we will assume sufficiently large SNR, i.e. sufficiently small noise. For the error of the raw magnitude, we have the following estimate.

Lemma 3.1. *Let $\overline{\nu}_i^\delta = \overline{m}_i - \overline{m}_i^\delta$ be the error of the raw magnitude. Then*

$$\left|\overline{\nu}_i^\delta\right| \leq C\,\overline{m}_i \left(\frac{\left|u^\dagger\right|_{W^{1,\infty}(\Omega_{\mathrm{FOV}})}\, h}{v_{\mathrm{enc}}} + \frac{1}{\mathrm{SNR}_i} \right).$$

Proof. Using the inverse triangle inequality and the estimate (3.7) for the velocity deviation from the weighted mean, we obtain

$$\begin{aligned}
\left|\overline{m}_i^\delta - \overline{m}_i\right| &= \left|\left|\overline{m}_i^\delta\right| - \left|e^{i\pi\overline{u}_i/v_{\mathrm{enc}}}\overline{m}_i\right|\right| \\
&\leq \frac{1}{|V_i|}\int_{V_i} \rho(x)\left|e^{i\pi u^\dagger(x)/v_{\mathrm{enc}}} - e^{i\pi\overline{u}_i/v_{\mathrm{enc}}}\right| \mathrm{d}x + |\nu_i^c| \\
&\leq \frac{1}{|V_i|}\int_{V_i} \rho(x)\frac{\pi}{v_{\mathrm{enc}}}\left|u^\dagger(x) - \overline{u}_i\right| \mathrm{d}x + |\nu_i^c| \\
&\leq \frac{\pi}{v_{\mathrm{enc}}}\left\|u^\dagger - \overline{u}_i\right\|_{L^\infty(V_i)} \overline{m}_i \;+\; |\nu_i^c| \\
&\leq C\,\overline{m}_i \left(\frac{\left|u^\dagger\right|_{W^{1,\infty}(\Omega_{\mathrm{FOV}})}\, h}{v_{\mathrm{enc}}} + \frac{1}{\mathrm{SNR}_i} \right).
\end{aligned}$$

□

In a similar manner, we can estimate the deviation of the raw velocity $\overline{u}_i^\varepsilon$ from the modelled velocity $\overline{u}_i$ by the following estimate.

Lemma 3.2. *Let $\overline{\nu}_{u,i} = \overline{u}_i - \overline{u}_i^\varepsilon$ be the error of the raw velocity data. Let SNR_i be sufficiently large and the data resolution h be sufficiently high. Then the velocity error satisfies*

$$|\overline{\nu}_i^\varepsilon| \leq C \left(\frac{\left|u^\dagger\right|^3_{W^{1,\infty}(\Omega_{\mathrm{FOV}})}\, h^3}{v_{\mathrm{enc}}^2} \;+\; \frac{\left|u^\dagger\right|^2_{W^{1,\infty}(\Omega_{\mathrm{FOV}})}\, h^2}{v_{\mathrm{enc}}}\,\frac{1}{\mathrm{SNR}_i} \;+\; \frac{v_{\mathrm{enc}}}{\mathrm{SNR}_i} \right).$$

Proof. Elementary calculations lead to

$$\begin{aligned}
|\overline{\nu}_i^\varepsilon| &= \tfrac{v_{\mathrm{enc}}}{\pi}\left|\arg(c_i) - \arg\left(e^{i\pi\overline{u}_i/v_{\mathrm{enc}}}\right)\right| &&= \tfrac{v_{\mathrm{enc}}}{\pi}\left|\arg\left(c_i\, e^{-i\pi\overline{u}_i/v_{\mathrm{enc}}}\right)\right| \\
&= \tfrac{v_{\mathrm{enc}}}{\pi}\left|\arctan\left(\frac{\mathrm{Im}\left(c_i\, e^{-i\pi\overline{u}_i/v_{\mathrm{enc}}}\right)}{\mathrm{Re}\left(c_i\, e^{-i\pi\overline{u}_i/v_{\mathrm{enc}}}\right)}\right)\right| &&\leq \tfrac{v_{\mathrm{enc}}}{\pi}\left|\frac{\mathrm{Im}\left(c_i\, e^{-i\pi\overline{u}_i/v_{\mathrm{enc}}}\right)}{\mathrm{Re}\left(c_i\, e^{-i\pi\overline{u}_i/v_{\mathrm{enc}}}\right)}\right|.
\end{aligned}$$

Let us consider the numerator. Using a Taylor explansion for the sinus, estimate (3.7) and

the definition of $\overline{u}_i$, we estimate

$$\begin{aligned}
\left|\mathrm{Im}\left(c_i\, e^{-i\pi\overline{u}_i/v_{\mathrm{enc}}}\right)\right| &= \left|\frac{1}{|V_i|}\int_{V_i}\rho(x)\sin\left(\pi\frac{u^\dagger(x)-\overline{u}_i}{v_{\mathrm{enc}}}\right)\,\mathrm{d}x + \mathrm{Im}\left(\nu_i^c\, e^{-i\pi\overline{u}_i/v_{\mathrm{enc}}}\right)\right| \\
&\leq \left|\frac{1}{|V_i|}\int_{V_i}\rho(x)\left(\pi\frac{u^\dagger(x)-\overline{u}_i}{v_{\mathrm{enc}}}+\mathcal{O}\left(\left(\pi\frac{u^\dagger(x)-\overline{u}_i}{v_{\mathrm{enc}}}\right)^3\right)\right)\,\mathrm{d}x\right| + |\nu_i^c| \\
&= \left|\frac{1}{|V_i|}\int_{V_i}\rho(x)\mathcal{O}\left(\left(\pi\frac{u^\dagger(x)-\overline{u}_i}{v_{\mathrm{enc}}}\right)^3\right)\,\mathrm{d}x\right| + |\nu_i^c| \\
&\leq C\,\overline{m}_i\left(\frac{\left|u^\dagger\right|^3_{W^{1,\infty}(\Omega_{\mathrm{FOV}})}\,h^3}{v_{\mathrm{enc}}^3}+\frac{1}{\mathrm{SNR}_i}\right).
\end{aligned}$$

For the denominator, we compute with similar arguments

$$\begin{aligned}
\left|\mathrm{Re}\left(c_i\, e^{-i\pi\overline{u}_i/v_{\mathrm{enc}}}\right)\right| &= \left|\frac{1}{|V_i|}\int_{V_i}\rho(x)\cos\left(\pi\frac{u^\dagger(x)-\overline{u}_i}{v_{\mathrm{enc}}}\right)\,\mathrm{d}x + \mathrm{Re}\left(\nu_i^c\, e^{-i\pi\overline{u}_i/v_{\mathrm{enc}}}\right)\right| \\
&\geq \left|\frac{1}{|V_i|}\int_{V_i}\rho(x)\left(1+\mathcal{O}\left(\left(\pi\frac{u^\dagger(x)-\overline{u}_i}{v_{\mathrm{enc}}}\right)^2\right)\right)\,\mathrm{d}x\right| - |\nu_i^c| \\
&\geq \overline{m}_i\left(1\;-\;C\,\frac{\left|u^\dagger\right|^2_{W^{1,\infty}(\Omega_{\mathrm{FOV}})}\,h^2}{v_{\mathrm{enc}}^2}-\frac{1}{\mathrm{SNR}_i}\right).
\end{aligned}$$

Since we assumed sufficiently high resolution and large SNR, the term $\overline{m}_i$ dominates the denominator. Elementary computations reveal that

$$\begin{aligned}
|\overline{\nu}_{u,i}| &\leq \frac{v_{\mathrm{enc}}}{\pi}\left|\frac{\mathrm{Im}\left(c_i\, e^{-i\pi\overline{u}_i/v_{\mathrm{enc}}}\right)}{\mathrm{Re}\left(c_i\, e^{-i\pi\overline{u}_i/v_{\mathrm{enc}}}\right)}\right| \\
&\leq \frac{v_{\mathrm{enc}}}{\pi}\,\frac{C\,\overline{m}_i\,\left(\left|u^\dagger\right|^3_{W^{1,\infty}(\Omega_{\mathrm{FOV}})}\,h^3\,v_{\mathrm{enc}}^{-3}+\mathrm{SNR}_i^{-1}\right)}{\overline{m}_i\left(1\;-\;C\;|u^\dagger|^2_{W^{1,\infty}(\Omega_{\mathrm{FOV}})}\,h^2\,v_{\mathrm{enc}}^{-2}-\mathrm{SNR}_i^{-1}\right)} \\
&\leq C\,\left(\frac{\left|u^\dagger\right|^3_{W^{1,\infty}(\Omega_{\mathrm{FOV}})}\,h^3}{v_{\mathrm{enc}}^2}\;+\;\frac{\left|u^\dagger\right|^2_{W^{1,\infty}(\Omega_{\mathrm{FOV}})}\,h^2}{v_{\mathrm{enc}}}\,\frac{1}{\mathrm{SNR}_i}\;+\;\frac{v_{\mathrm{enc}}}{\mathrm{SNR}_i}\right).
\end{aligned}$$

□

We summarize our observation from the derived estimates in the following remark.

Remark 3.3. The noise for the raw magnitudes remains controlled by the *signal-to-noise ratio*. For the raw velocities, the noise amplification is controlled by the velocity encoding v_{enc} as it is reported in the literature [34]. Based on our assumption on the physical data acquisition, we introduced an additional model error. Due to the second order approximation, it usually has only minor impact on the raw velocity error, in contrast to a nodal interpretation of the measurement errors that is widely used [53, 88, 100]. However, the corruption of the raw magnitudes is of first order and may become substantial, as it is the case for signal loss in turbulent flow regimes that are characterized by large velocity gradients.

3.1.3 Pre-Processing of the Raw Data

From a magnetic resonance measurement, we obtain the raw data $\overline{m}^\delta$ and $\overline{u}^\varepsilon$. Although the raw data are appropriatly modelled, their direct use has a serious drawback: instead of explicit information about the flow domain $\Omega^\dagger$, the models for the raw magnitude $\overline{m}^\delta$ and raw velocity $\overline{u}^\varepsilon$, contain the signal density ρ according to (3.6). Since we do not want to approximate the signal density, we have to transform the information about the signal density to information about the flow domain and eliminate ρ from the models.

Data model. The model for magnitude and velocity, given by (3.1) and (3.2), is

$$m_i := \frac{\left|\Omega^\dagger \cap V_i\right|}{|V_i|} \text{ and } u_i := \frac{1}{|V_i|} \int\limits_{V_i} u^\dagger(x)\,\mathrm{d}x.$$

Assumption on the signal density. The elimination of the signal density ρ is based on the assumption that the signal density ρ is at least locally almost constant in every material: Let ω_i denote the $(2n+1)^d$-patch centered around the voxel V_i. Then for every voxel V_i we have characteristic signal densities $\rho_{f,i}$ and $\rho_{e,i}$ for the flow and exterior domain, respectively, such that

$$\nu_{\rho,i,n} := \left\|\rho - \left(\rho_{f,i}\chi_{\Omega^\dagger} + \rho_{e,i}\left(1 - \chi_{\Omega^\dagger}\right)\right)\right\|_{L^\infty(\omega(i))} \leq C\left|\nu_i^c\right|. \tag{3.8}$$

Hence, the perturbations from the ideal material-wise constant signal density are negligably small compared to the measurement noise or occur on a substantially larger geometric scale compared to the voxel size. Based on a pre-segmentation, we can approximate the characteristic signal densities.

Pre-segmentation. By standard methods, one can perform a rough pre-segmentation of the flow domain $\Omega^\dagger$ and characterize voxels as interior, boundary or exterior voxels. The segmentation must guarantee that interior voxels lie fully in the flow domain $\Omega^\dagger$ and exterior voxels lie fully outside. The remaining voxels are labelled as boundary voxels and a certain patch around them contains both, interior and exterior voxels. A good pre-segmentation labels only few voxels as boundary voxels, resulting in rather small patches.

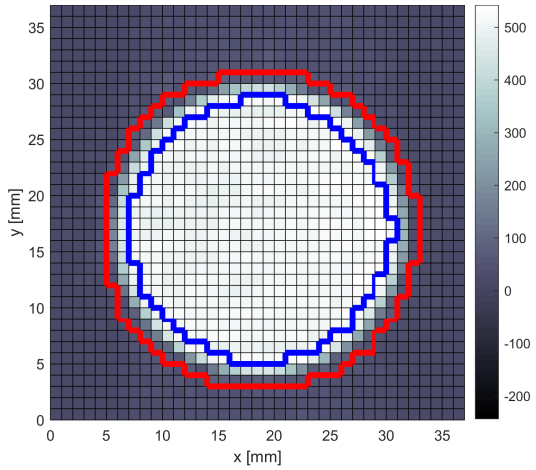

Figure 3.1: Magnitude raw data $\overline{m}_i^\delta$ with resolution $h = 1$mm and homogeneous pre-segmentation with interior-boundary interface (blue) and boundary-exterior interface (red).

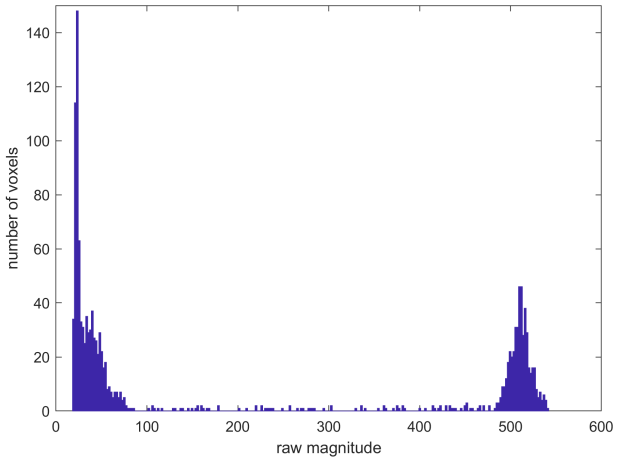

Figure 3.2: Histogram of magnitude raw data $\overline{m}_i^\delta$ from the measurement depicted left. The peaks at 22 and 509 define the characteristic signal densities $\rho_{e,i}^\delta$ and $\rho_{f,i}^\delta$.

Pre-segmentation algorithm, homogeneous case. For homogeneous exterior material and signal reception, the characteristic signal densities are globally constant. This applies to 2D measurements of flow phantoms, as it is illustrated in Figure 3.1. In this case, we consider the histogram of the raw magnitude values $\overline{m}_i^\delta$. The histogram exhibits a typical structure consisting of two peaks, a larger peak at a lower number and a smaller peak at a higher number, see Figure 3.2. Typically, the exterior domain in the field of view is larger than the flow domain and the fluid produces a higher signal than the exterior material due to the high proton density. Due to their small portion on the field of view and the high magnitude variance the voxels in the boundary region are negligible in the histogram. Hence, we define globally constant approximations $\rho_{f,i}^\delta$ and $\rho_{e,i}^\delta$ of the characteristic densities $\rho_{f,i}$ and $\rho_{e,i}$ as positions of the peaks associated with the fluid and exterior material, respectively. We define a cutoff raw magnitude as average of the two peaks. If all raw magnitudes in a 3^d-patch centered around a certain voxel are below or above the cutoff level, than the corresponding voxel is labelled exterior respective interior. The remaining voxels are boundary voxels.

Pre-segmentation algorithm, inhomogeneous case. Due to the positioning of the receiver coils, 3D measurements reveal a substantial loss in the signal reception towards the boundary of the field of view Ω_{FOV}. *In vivo* measurements of the aorta show different types of neighboured tissue, producing a varying signal density. In these inhomogeneous cases, we cannot find constant characteristic signal densities. Instead, we have to define characteristic signal densities locally: in a first step, we perform the pre-segmentation. Since the exterior domain may be complex and consist of several different tissues, we segment the flow domain only, select a safety-region as boundary region and label the remaining voxels

as exterior. In practice, we used a region growing segmentation algorithm [71]. Seeded with the voxels with maximal raw magnitude, the set of interior voxels is iteratively enlarged by checking the neighboured voxels of the previously selected voxels for satisfying a selection criterion until the iteration stagnates. As selection function we use a manually weighted difference of the raw magnitude and the absolute value of a Laplacian edge detector. Voxels are accepted, if the selection function is larger than a manually chosen cutoff value. Other voxels, that are contained in a manually defined patch around some interior voxel, are labelled as boundary voxels. The remaining voxels are labelled as exterior voxels. For a boundary voxel we sequentially enlarge a patch around this voxel, until it contains an interior voxel. The mean of the raw magnitude values $\overline{m}_j^\delta$ of the interior voxels V_j contained in the patch is used as $\rho_{f,i}^\delta$ and $\rho_{e,i}^\delta$ is defined analogously. We may assume that the approximations satisfy

$$\left|\rho_{f,i} - \rho_{f,i}^\delta\right| + \left|\rho_{e,i} - \rho_{e,i}^\delta\right| \leq C \left|\overline{\nu}_i^\delta\right|,$$

since the definition of the local characteristic density levels is based on the available raw magnitude.

Normalization of the raw data. Given the raw magnitude data $\overline{m}_i^\delta$ and the approximate characteristic signal densities $\rho_{f,i}^\delta$ and $\rho_{e,i}^\delta$ for the boundary voxels, we define the following approximation m_i^δ of the normalized magnitude m_i:

$$m_i^\delta := \begin{cases} 1 & \text{for interior voxel } V_i, \\ \left(\overline{m}_i^\delta - \rho_{e,i}^\delta\right) / \left(\rho_{f,i}^\delta - \rho_{e,i}^\delta\right) & \text{for boundary voxel } V_i, \\ 0 & \text{for exterior voxel } V_i. \end{cases} \tag{3.9}$$

Given the raw velocity data $\overline{u}_i^\varepsilon$, we define the approximation u_i^ε of the velocity u_i by

$$u_i^\varepsilon := \begin{cases} \overline{u}_i^\varepsilon & \text{for interior voxel } V_i, \\ \left(\overline{m}_i^\delta / \rho_{f,i}^\delta\right) \overline{u}_i^\varepsilon & \text{for boundary voxel } V_i, \\ 0 & \text{for exterior voxel } V_i. \end{cases} \tag{3.10}$$

Now, we can investigate the overall errors of the pre-processed data.

Estimating the errors. To assess the approximation accuracy of the magnitude, for boundary voxels V_i we introduce the *contrast-to-noise ratio*

$$\mathrm{CNR}_i := \frac{|\rho_{f,i} - \rho_{e,i}|}{|\nu_i^c|}. \tag{3.11}$$

For the following considerations, we assume sufficiently large CNR.

Proposition 3.4. *Let $\nu_i^\delta = m_i - m_i^\delta$ be the measurement error of the pre-processed magnitude data. For interior or exterior voxel V_i, we have $\nu_i^\delta = 0$. For any boundary voxel V_i*

$$|\nu_i^\delta| \leq C \left(\frac{1}{\mathrm{CNR}_i} + \frac{\mathrm{SNR}_i}{\mathrm{CNR}_i} \frac{\left|u^\dagger\right|_{W^{1,\infty}(V_i)} h}{v_{\mathrm{enc}}} \right).$$

Proof. For interior or exterior voxels, the assertion follows by the assumption on the pre-segmentation. We consider a boundary voxel V_i and split the error in a model error and an error amplification

$$\left|\nu_i^\delta\right| \leq \left| m_i - \frac{\overline{m}_i - \rho_{e,i}}{\rho_{f,i} - \rho_{e,i}} \right| + \left| \frac{\overline{m}_i - \rho_{e,i}}{\rho_{f,i} - \rho_{e,i}} - \frac{\overline{m}_i^\delta - \rho_{e,i}^\delta}{\rho_{f,i}^\delta - \rho_{e,i}^\delta} \right| = (i) + (ii).$$

We observe, using the assumption (3.8), that

$$\begin{aligned} |\overline{m}_i - (\rho_{f,i}\, m_i + \rho_{e,i}(1 - m_i))| &= \frac{1}{|V_i|} \int_{V_i} |\rho(x) - (\rho_{f,i}\chi_{\Omega^\dagger}(x) + \rho_{e,i}\,(1 - \chi_{\Omega^\dagger}(x)))|\, \mathrm{d}x \\ &\leq \frac{1}{|V_i|} \int_{V_i} \nu_{\rho,i,n}\, \mathrm{d}x \;\leq\; C\,|\nu_i^c|\,. \end{aligned}$$

Then for the model error we obtain

$$\begin{aligned} (i) &\leq \left| m_i - \frac{\rho_{f,i} m_i + \rho_{e,i}(1 - m_i) - \rho_{e,i}}{\rho_{f,i} - \rho_{e,i}} \right| + \left| \frac{C\nu_i^c}{\rho_{f,i} - \rho_{e,i}} \right| \\ &= C \frac{|\nu_i^c|}{|\rho_{f,i} - \rho_{e,i}|} \;\leq\; C\, \frac{1}{\mathrm{CNR}_i}. \end{aligned}$$

Using Lemma 3.1, for the amplification of the raw magnitude errors and the characteristic density errors we obtain

$$\begin{aligned} (ii) &\leq \left| \frac{\left(\overline{m}_i - \overline{m}_i^\delta\right) - \left(\rho_{e,i} - \rho_{e,i}^\delta\right)}{\rho_{f,i} - \rho_{e,i}} \right| + C \left| \frac{\overline{m}_i^\delta - \rho_{e,i}^\delta}{\rho_{f,i} - \rho_{e,i}} \right| \left| \frac{\left(\rho_{f,i} - \rho_{f,i}^\delta\right) - \left(\rho_{e,i} - \rho_{e,i}^\delta\right)}{\rho_{f,i} - \rho_{e,i}} \right| \\ &\leq C \left| \frac{\overline{\nu}_i^\delta}{\rho_{f,i} - \rho_{e,i}} \right| \;\leq\; C \left(\left| \frac{\nu_i^c}{\rho_{f,i} - \rho_{e,i}} \right| + \left| \frac{\overline{m}_i}{\rho_{f,i} - \rho_{e,i}} \frac{\left|u^\dagger\right|_{W^{1,\infty}(V_i)}\, h}{v_{\mathrm{enc}}} \right| \right) \\ &= C \left(\frac{1}{\mathrm{CNR}_i} + \frac{\mathrm{SNR}_i}{\mathrm{CNR}_i} \frac{\left|u^\dagger\right|_{W^{1,\infty}(V_i)}\, h}{v_{\mathrm{enc}}} \right). \end{aligned}$$

Combining the estimates for (i) and (ii) yields the assertion. □

For the velocity data we obtain also errors inside the domain.

Proposition 3.5. *Let $\nu_i^\varepsilon = u_i - u_i^\varepsilon$ be the error of the pre-processed velocity data and let the previously made assumptions hold. For an exterior voxel V_i, we then have $\nu_i^\varepsilon = 0$. For an interior voxel V_i, on the other hand, there holds*

$$|\nu_i^\varepsilon| \leq C \left(\frac{\left|u^\dagger\right|_{W^{1,\infty}(V_i)}^3\, h^3}{v_{\mathrm{enc}}^2} + \frac{\left|u^\dagger\right|_{W^{1,\infty}(V_i)}^2\, h^2}{v_{\mathrm{enc}}} \frac{1}{\mathrm{SNR}_i} + \frac{v_{\mathrm{enc}}}{\mathrm{SNR}_i} \right).$$

Finally, for any boundary voxel V_i, we have

$$|\nu_i^\varepsilon| \leq C \left(\frac{\left|u^\dagger\right|_{W^{1,\infty}(V_i)}^3 h^3}{v_{\mathrm{enc}}^2} + \frac{\left|u^\dagger\right|_{W^{1,\infty}(V_i)} h}{v_{\mathrm{enc}}} \left\|u^\dagger\right\|_{L^\infty(V_i)} + \frac{\left|u^\dagger\right|_{W^{1,\infty}(V_i)}^2 h^2}{v_{\mathrm{enc}}} \frac{1}{\mathrm{SNR}_i} + \frac{v_{\mathrm{enc}}}{\mathrm{SNR}_i} \right).$$

Proof. For an exterior voxel, the assertion follows by the assumption on the pre-segmentation. For an interior voxel, we split the error in a modelling error and the raw data error

$$|\nu_i^\varepsilon| \leq |u_i - \overline{u}_i| + |\overline{u}_i - \overline{u}_i^\varepsilon| = |u_i - \overline{u}_i| + |\overline{\nu}_i^\varepsilon| \,.$$

Note that u_i is the averaged velocity and $\overline{u}_i$ is the averaged velocity with the density ρ serving as weighting function. Using the estimate (3.8) and the estimation of the velocity by the velocity encoding, for the modelling error $u_i - \overline{u}_i$, we compute

$$\begin{aligned} |u_i - \overline{u}_i| &= \frac{1}{|V_i|\ \overline{m}_i} \left| \int_{V_i} u^\dagger(x) \left(\overline{m}_i - \rho(x)\right) \mathrm{d}x \right| \leq \left\|u^\dagger\right\|_{L^\infty(V_i)} \frac{\|\overline{m}_i - \rho\|_{L^\infty(V_i)}}{\overline{m}_i} \\ &\leq C, \left\|u^\dagger\right\|_{L^\infty(V_i)} \frac{|\nu_i^c|}{\overline{m}_i} \leq C\, v_{\mathrm{enc}} \frac{1}{\mathrm{SNR}_i}. \end{aligned}$$

Absorbing this estimate in the estimate for $|\overline{\nu}_i^\varepsilon|$ yields the assertion.
Let us finally turn to the boundary voxel. Again, we split the error into a modelling error and amplifications of raw data errors by

$$|\nu_i^\varepsilon| \leq \left| u_i - \frac{\overline{m}_i}{\rho_{f,i}} \overline{u}_i \right| + \left| \left(\frac{\overline{m}_i}{\rho_{f,i}} - \frac{\overline{m}_i^\delta}{\rho_{f,i}^\delta} \right) \overline{u}_i \right| + \left| \frac{\overline{m}_i^\delta}{\rho_{f,i}^\delta} \left(\overline{u}_i - \overline{u}_i^\varepsilon\right) \right| = (i) + (ii) + (iii).$$

For the modelling error we similarly obtain

$$\begin{aligned} (i) = \left| u_i - \frac{\overline{m}_i}{\rho_{f,i}} \overline{u}_i \right| &= \left| \frac{1}{|V_i|} \int_{V_i} u^\dagger(x) \left(1 - \frac{\rho(x)}{\rho_{f,i}}\right) \mathrm{d}x \right| \\ &= \frac{\overline{m}_i}{\rho_{f,i}} \left| \frac{1}{|V_i|} \int_{\Omega^\dagger \cap V_i} u^\dagger(x) \frac{\rho_{f,i} - \rho(x)}{\overline{m}_i} \mathrm{d}x \right| \\ &\leq \frac{\overline{m}_i}{\rho_{f,i}} \left\|u^\dagger\right\|_{L^\infty(V_i)} \frac{\|\rho_{f,i} - \rho\|_{L^\infty(V_i \cap \Omega^\dagger)}}{\overline{m}_i} \leq C\, v_{\mathrm{enc}} \frac{1}{\mathrm{SNR}_i}. \end{aligned}$$

The propagation of the error in the raw magnitude and the characteristic signal densities amounts to

$$\begin{aligned} (ii) &= \left| \left(\frac{\overline{m}_i}{\rho_{f,i}} - \frac{\overline{m}_i^\delta}{\rho_{f,i}^\delta} \right) \overline{u}_i \right| \leq \left(\frac{\overline{m}_i}{\rho_{f,i}} \frac{|\overline{\nu}_i^\delta|}{\overline{m}_i} + C \frac{\overline{m}_i\, \overline{m}_i^\delta}{\rho_{f,i}^2} \frac{|\rho_{f,i} - \rho_{f,i}^\delta|}{\overline{m}_i} \right) |\overline{u}_i| \\ &\leq C \frac{|\overline{\nu}_i^\delta|}{\overline{m}_i} \left\|u^\dagger\right\|_{L^\infty(V_i)} \leq C \left(\frac{v_{\mathrm{enc}}}{\mathrm{SNR}_i} + \frac{\left|u^\dagger\right|_{W^{1,\infty}(V_i)} h}{v_{\mathrm{enc}}} \left\|u^\dagger\right\|_{L^\infty(V_i)} \right). \end{aligned}$$

The assertion follows by estimating the propagated raw velocity error

$$(iii) = \frac{\overline{m}_i^\delta}{\rho_{f,i}^\delta} \, |\overline{\nu}_i^\varepsilon| \leq C \left(\frac{\left|u^\dagger\right|_{W^{1,\infty}(V_i)}^3 h^3}{v_{\mathrm{enc}}^2} + \frac{\left|u^\dagger\right|_{W^{1,\infty}(V_i)}^2 h^2}{v_{\mathrm{enc}}} \frac{1}{\mathrm{SNR}_i} + \frac{v_{\mathrm{enc}}}{\mathrm{SNR}_i} \right).$$

Absorbing some terms using $\left\|u^\dagger\right\|_{L^\infty(V_i)} \leq C v_{\mathrm{enc}}$ yields the assertion. □

Before we proceed, let us briefly summarize our observations.

Remark 3.6. Provided, that the pre-segmentation detects the boundary with accuracy h, we may assume that the domain Ω_b, obtained by the union of all boundary voxels, has volume h. Therefore, from Proposition 3.4 we obtain the results already stated in (3.3)

$$\|\nu^\delta\|_{L^2(\Omega_{\mathrm{FOV}})} = \|\nu^\delta\|_{L^2(\Omega_b)} \leq C \frac{\sqrt{h}}{\mathrm{CNR}} \left(1 + \frac{|u^\dagger|_{W^{1,\infty}(\Omega^\dagger)}^2}{v_{\mathrm{enc}}^2} \, h \, \mathrm{SNR} \right).$$

Furthermore, we assume, that the boundary layer is resolved, containing the highest derivatives, and hence

$$\|u^\dagger\|_{W^{1,\infty}(\Omega^\dagger)} \, h \leq \|u\|_{L^\infty(\Omega^\dagger)} \leq v_{\mathrm{enc}}.$$

Therefore the contribution of all interior voxel, spanning Ω_i, to the velocity error is

$$\|\nu^\varepsilon\|_{L^2(\Omega_i)} \leq C \frac{v_{\mathrm{enc}}}{\mathrm{SNR}},$$

while the contribution of all boundary voxel amounts to

$$\|\nu^\varepsilon\|_{L^2(\Omega_b)} \leq C \sqrt{h} \, v_{\mathrm{enc}} \left(\frac{\|u^\dagger\|_{W^{1,\infty}(\Omega^\dagger)}}{v_{\mathrm{enc}}} \, h + \frac{1}{\mathrm{SNR}} \right).$$

Summarizing the contributions, we obtain the proposed estimate (3.4).

Finally, let us comment on a detail regarding our previous works.

Remark 3.7. In previous works [25, 86], we used the velocity model

$$\widetilde{u}_i = \frac{1}{|\Omega^\dagger \cap V_i|} \int\limits_{\Omega^\dagger \cap V_i} u^\dagger(x) \, \mathrm{d}x$$

instead of (3.2). This leads to an approximation by

$$\widetilde{u}_i^\varepsilon = \frac{\overline{m}_i^\delta}{\rho_{f,i}^\delta \, m_i^\delta} \, \overline{u}_i^\varepsilon.$$

This is not a stable approximation, since $1/m_i^\delta$ is not bounded and might amplify errors. The subsequent algorithm incorporated an integration over the flow domain, formally eliminating the factor $1/m_i^\delta$. However, for the integration another approximation of m_i was used, causing instabilities. Here, we incorporate an integration over the full field of view, leading to the model (3.2) and preventing these instabilities.

3.2 Numerical Realization

For limited data resolution the derived voxelized data model (3.1) and (3.2) considerably deviates from the idealized data model (2.40) and (2.45). To obtain an accurate reconstruction, we introduce modified forward operators for the geometry and velocity measurement that are conforming with the voxelized data model. By using an appropriate discretization of the underlying spaces for the geometry parameter and the velocity, the Tikhonov minimization problems are cast in finite-dimensional optimization problems that are solved by standard methods. In the case of the geometry reconstruction, a differentiable modification of the non-differentiable forward is introduced for the purpose of applying gradient methods for the minimization. Finally, we show that the theory of the previous chapter translates to the fully discrete problems.

Note that the wall shear stress estimate is analytically obtained from the reconstructed geometry parameter and velocity. Hence, with given reconstructed geometry parameter and velocity the numerical realization is straightforward.

3.2.1 Discrete Geometry Reconstruction

Let us recall that we parametrize the flow domain around some central point (2D) or around a centerline (3D), respectively. These anchor points are easily obtained by standard methods from the pre-processed and pre-segmented magnitude data $m^\delta \in L^2(\Omega_{\mathrm{FOV}})$. In the two-dimensional case, the origin is shifted to this central point.

Modification of the forward operator. Let us recall that for the parameter domain $D = \mathcal{S}^1$ (2D) or $D = \mathcal{S}^1 \times (0,1)$ (3D) the domain of the geometry forward operator is given by

$$\mathcal{D}(F) \;=\; \left\{ R \in H^3(D) \;\middle|\; R_{\max} \geq R \geq R_{\min} \right\}$$

for some upper and lower bounds $R_{\max}, R_{\min} \in \mathcal{C}(\overline{D})$. Using the generalized cylindrical coordinates and the transformation (2.33), we have the forward operator

$$F : \mathcal{D}(F) \subset L^2(D) \to L^2(\Omega_{\mathrm{FOV}}), \quad F(R) \;=\; \chi_{\Omega(R)} \;=\; H((R(\varphi(x), s(x)) - r(x)),$$

where $H = \chi_{(0,\infty)}$ denotes the Heaviside function. The voxelized modification conforming with the discrete data model (2.2) reads

$$F_h : \mathcal{D}(F) \subset L^2(D) \to L^2(\Omega_{\mathrm{FOV}}),\; F_h(R) \;:=\; \sum_{i=1}^{N_V} \chi_{V_i} \frac{1}{|V_i|} \int\limits_{V_i} H(R(\varphi(x), s(x)) - r(x))\,\mathrm{d}x.$$

However, this operator is not differentiable due to non-smoothnes of the Heaviside function. Therefore, we introduce

$$F_{h,\gamma} : \mathcal{D}(F) \subset L^2(D) \to L^2(\Omega_{\mathrm{FOV}}), F_{h,\gamma}(R) := \sum_{i=1}^{N_V} \chi_{V_i} \frac{1}{|V_i|} \int\limits_{V_i} H_\gamma(R(\varphi(x), s(x)) - r(x))\,\mathrm{d}x,$$

where $H_\gamma(x) = \arctan(x/\gamma)/\pi + 1/2$ is a smooth approximation of H with approximation error controlled by $\gamma > 0$. Analytical differentiation in direction $\tilde{R} \in H^3(D)$ yields

$$DF_{h,\gamma}(R)\tilde{R} = \sum_{i=1}^{N_V} \chi_{V_i} \frac{1}{|V_i|} \int_{V_i} H'_\gamma(R(\varphi(x), s(x)) - r(x))\tilde{R}(\varphi(x), s(x))\,\mathrm{d}x, \tag{3.12}$$

i.e. $F_{h,\gamma}$ is indeed differentiable. We even have Lipschitz continuity of the derivative. We finally introduce the associated Tikhonov functional

$$\mathcal{T}^\delta_{\alpha,h} : \mathcal{D}(F) \to \mathbb{R}, \quad \mathcal{T}^\delta_{\alpha,h}(R) := \left\| F_{h,\gamma}(R) - m^\delta \right\|^2_{L^2(\Omega_{\mathrm{FOV}})} + \alpha\, |R|^2_{H^3(D)}\,. \tag{3.13}$$

We use $\gamma = h/10$ and observe that this leads to a suitable approximation.

Remark 3.8. Approximate Tikhonov minimizers of $\mathcal{T}^\delta_{\alpha,h}$ may be treated as approximate Tikhonov minimizers of $\mathcal{T}^\delta_\alpha$. Let $R \in \mathcal{D}(F)$ with $\|R\|_{H^3(\Omega)} \le C$: Since $\|\nabla R\|_{L^\infty(D)} < C$, one can show that $\partial\Omega(R)$ intersects with at most C/h (2D) or C/h^2 (3D) voxel. We conclude that

$$\|F_h(R) - F(R)\|_{L^2(\Omega_{\mathrm{FOV}})} \le C\, h^{1/2}.$$

Furthermore, elementary calculations with $\gamma = h/10$ reveal that

$$\|F_h(R) - F_{h,\gamma}(R)\|_{L^2(\Omega_{\mathrm{FOV}})} \le C\, \gamma^{1/2} \le C\, h^{1/2}.$$

In view of Proposition 2.10 and the expectation $\delta \approx Ch^{1/2}$ on the data error from (3.3), we can replace the idealized operator with the differentiable voxelized version.

Discretization. In the two-dimensional case, we utilize a spectral discretization

$$X_N := \left\{ a_0 + \sum_{n=1}^{N} a_n \cos(n\,\cdot) + b_n \sin(n\,\cdot) \;\middle|\; a_0, \dots, a_N, b_1, \dots, b_N \in \mathbb{R} \right\} \subset H^3(D).$$

In the three-dimensional case, we have $D = \mathcal{S}^1 \times (0,1)$ and utilize a spline discretization

$$X_N := Q^3(D_N) \subset H^3(D),$$

where $Q^3(D_N)$ denotes the H^3-conforming bi-cubic splines on an $N \times N$ regular grid of D. Note that this choice includes periodic boundary conditions in the polar direction, while no boundary conditions in the axial direction are imposed. In practice, we use $N = 20$.

The constraints $R_{\min} \le R \le R_{\max}$ for $R \in \mathcal{D}(F)$ would lead to a variational inequality. These are technical constraints that are necessary for the analysis, but no limitation for reasonable approximations of the geometry. Hence, we neglect the constraints for the optimization and consider the discrete minimization problem

$$\min_{R_N \in X_N} \frac{1}{|\Omega_{\mathrm{FOV}}|} \|F_{h,\gamma}(R_N) - m^\delta\|^2_{L^2(\Omega_{\mathrm{FOV}})} + \alpha\, \frac{1}{\overline{R}^2} |R_N|^2_{H^3(D)}. \tag{3.14}$$

For standardization of the regularization parameter α, we normalized the data error and the regularization term with the volume of the field of view and an approximation $\overline{R} > 0$ of the mean of the geometry parameter. This only amounts to a rescaling of the regularization parameter. For sufficiently large N, i.e. for high discretization, the theory from Section 2.4 transfers to the fully discrete scheme.

Remark 3.9. Using the continuity of $F_{h,\gamma}$ and basic results on interpolation errors, one can show, cf. the proof of Proposition 2.10, that approximate Tikhonov minimizers of the discrete Tikhonov functional are approximate Tikhonov minimizers of the originate functional.

Minimization of the discrete Tikhonov functional. The solution of (3.14) requires the definition of an initial value and subsequently a non-linear iteration.

Step 1: Definition of the initial reconstruction R^0. We interprete the magnitude data m^δ as perturbed level set function for the flow domain, where the boundary is defined implicitly as preimage of $m^\delta = 1/2$. To get samples for boundary points, we smooth the magnitude data m^δ to allow for stable nodal evaluation. This is efficiently done by an FFT. Afterwards, we consider all edges on the regular grid with nodal values below $1/2$ on one node and above $1/2$ on the other, and use the position of the linear interpolation taking $1/2$ as sample point of the boundary. $R^0 \in X_N$ is obtained by fitting a parametrization to the samples.

Step 2: Non-linear iteration. We utilize the iteratively regularized Gauss-Newton method that is a standard technique for problems with Lipschitz continuous derivative [11]. Let $R^k \in X_N$ be the previous iterate. With regularization parameter α_k and using the representation (3.12) of $DF_{h,\gamma}$, we solve the quadratic minimization problem

$$\min_{R^{k+1}\in X_N} \frac{1}{|\Omega_{\mathrm{FOV}}|} \left\| F_{h,\gamma}(R^k) + DF_{h,\gamma}(R^k)(R^{k+1} - R^k) - m^\delta \right\|^2_{L^2(\Omega_{\mathrm{FOV}})} + \alpha_k \frac{1}{\overline{R_0}^2} \left| R^{k+1} \right|^2_{H^3(D)}.$$

The resulting optimality condition is a linear system and solved with a direct solver due to its low dimensionality. Finally, we have to define α_k and the stopping criterion at $k = K$. For the discrepancy principle, we use $\alpha_k = \alpha_{\max}/2^{k-1}$ and stop the iteration if $\|F_{h,\gamma}(R^K) - m^\delta\|_{L^2(\Omega_{\mathrm{FOV}})} < 2\delta$. If $\alpha = \alpha(\delta)$ is chosen *a priori*, then we use $\alpha_k = \max\{\alpha, \alpha_{\max}/2^{k-1}\}$ and stop the iteration if $\alpha_K = \alpha$ and $\|\nabla \mathcal{T}^\delta_{\alpha,h}(R^K)\|_Q \leq \mathrm{tol}$, where the Tikhonov gradient is measured in

$$S_1 Q S_2 := \frac{1}{|\Omega_{\mathrm{FOV}}|} (DF_{\gamma,h}(R^K)S_1, DF_{\gamma,h}(R^K)S_2)_{L^2(\Omega_{\mathrm{FOV}})} + \frac{\alpha}{\overline{R}^2} (D^3 S_1, D^3 S_2)_{L^2(D)}.$$

Here, all derivatives are discrete derivatives with respect to $R \in X_N$. The previous remarks and the construction of R^K reveals the following result.

Proposition 3.10. *For sufficiently high data resolution, discretization N and small tolerance, the final iterate $R^K \in X_N$ is an approximate Tikhonov minimizer of $\mathcal{T}^\delta_\alpha$. Hence, the derived error bounds in Subsection 2.4.1 transfer to the discrete solution.*

3.2.2 Discrete Velocity Approximation

Again, we provide a discrete velocity approximation algorithm that conforms with the voxelized velocity data model and computes approximate Tikhonov minimizers of the velocity approximation Tikhonov functional. However, the linearity of the forward simplifies the considerations. For simplicity, we consider the 3D case and just comment on the 2D case where it matters.

Modification of the forward operator. Let us recall that the velocity reference domain is $\widehat{\Omega} = (0,1) \times \mathcal{S}^1 \times (0,1)$ for the local and $\widehat{\Omega} = \mathcal{B}^2 \times (0,1)$ for the global velocity approximation. Then we investigate the space

$$\mathcal{D}(T) \;=\; \{v \in H^2(\widehat{\Omega}) \;\mid\; v = 0 \text{ on } \{1\} \times D\}.$$

Let R be the approximate geometry parameter, defining the flow geometry $\Omega = \Omega(R)$. With the inverse transformation $\Psi_R := \Omega \to \widehat{\Omega}$, the velocity forward operator is given by

$$T : \mathcal{D}(T) \to L^2(\Omega_{\mathrm{FOV}}), \quad Tv \;=\; T_R v \;=\; E_R(v \circ \Psi_R),$$

where E_R denotes the extension by zero. The voxelized modification is defined as

$$T_h : \mathcal{D}(T) \to L^2(\Omega_{\mathrm{FOV}}), \quad T_h v \;:=\; \sum_{i=1}^{N_V} \chi_{V_i} \frac{1}{|V_i|} \int\limits_{V_i \cap \Omega(R)} v(\Psi_R(x))\,\mathrm{d}x.$$

This leads to the corresponding Tikhonov functional

$$\mathcal{T}^{\varepsilon}_{\beta,h} : \mathcal{D}(T) \to \mathbb{R}, \quad \mathcal{T}^{\delta}_{\beta,h} \;:=\; \|T_h v - u^{\varepsilon}\|^2_{L^2(\Omega_{\mathrm{FOV}})} \;+\; \beta\,|v|^2_{H^2(\widehat{\Omega})}.$$

For $\|v\|_{H^2(\widehat{\Omega})} \leq C$, one can show that $\|Tv - T_h v\|_{L^2(\Omega_{\mathrm{FOV}})} \leq Ch^{1/2}$. Since we expect from (3.4) that $\varepsilon \approx C v_{\mathrm{enc}}/\mathrm{SNR}$, we observe the following from Proposition 2.10.

Remark 3.11. For sufficiently high data resolution, approximate Tikhonov minimizers of $\mathcal{T}^{\varepsilon}_{\beta,h}$ are approximate Tikhonov minimizers of the idealized functional $\mathcal{T}^{\varepsilon}_{\beta}$.

Discretization. The choice of the velocity discretization is of high importance in practice, since the computation of the velocity is the computational limiter of the technique. A low dimensional discretization that allows for a good reconstruction of the velocity, is favorable. Furthermore, local support and smoothness of the basis functions allows for fast assembling of the integral terms by high order quadrature rules. We utilize a tensor product discretization based on the coordinate splitting (r, φ, s), where radial and polar coordinate are connected due to smoothness issues at $r = 0$.

In the radial and angular coordinate, we introduce the space $X_N^r = Q^3(I_N) \subset H^3(0,1)$, containing cubic splines on a grid I_N of $(0,1)$, and define

$$\begin{aligned} X_N^{r,\varphi} := \operatorname{span}\{\, \Re(e^{in\varphi})\, v_R(r) \;\; | n \in \{0,1,\dots,N\},\, v_R \in X_N^r,\, v_R(1) = 0, \\ \text{for } n = 0:\; v_R'(0) = 0, \\ \text{for } n = 1:\; v_R(0) = v_R''(0) = 0, \\ \text{for } n = 2:\; v_R(0) = v_R'(0) = 0, \\ \text{for } n > 2:\; v_R(0) = v_R'(0) = v_R''(0) = 0 \,\}. \end{aligned}$$

Note that the boundary conditions ensure smoothness and conformity with $\mathcal{D}(T)$. We aim for approximating functions with large radial derivatives at the boundary. Therefore, we utilize an anisotropic spacing for I_N that is inspired by the localized estimate on the H^2-error of a cubic spline interpolation [21]:

$$\mathrm{ERR}(r) \;=\; h(r)^4\, D_4(r)^2\, r, \quad r \in (0,1).$$

We use $D_4 = 1$ for $r < 0.8$, $D4 = 20$ for $r > 0.9$ and in between the linear interpolation and choose implicitly a grid, such that with the corresponding spacing h the error function ERR becomes constant. In the axial coordinate, we utilize $X_N^s = Q^3(I_N) \subset H^3(0,1)$ on a regular N-grid I_N of $(0,1)$ without any boundary conditions and set

$$X_N \;:=\; X_N^{r,\varphi} \,\times X_N^s \;\subset \mathcal{D}(T) \cap H^2(\widehat{\Omega}).$$

For our computations, we use $N = 10$. The discrete velocity approximation problem reads

$$\min_{v_N \in X_N} \frac{1}{|\Omega_{\mathrm{FOV}}|}\, \|T_h v_N - u^\varepsilon\|^2_{L^2(\Omega_{\mathrm{FOV}})} \;+\; \beta\, |v_N|^2_{H^2(\widehat{\Omega})}. \tag{3.15}$$

Again, the data term is normalized to standardize the regularization parameter. Using the continuity of T_h, basic results on interpolation errors and similar arguments to the proof of Proposition 2.10 we make the following observation.

Proposition 3.12. *For sufficiently high discretization and data resolution, the minimizer of (3.15) is an approximate minimizer of the original Tikhonov functional. Hence, the derived error bounds in Subsection 2.4.2 transfer to the discrete solution.*

The optimality condition of the minimization problem (3.15) yields a linear equation that is solved by a direct solver due to its moderate dimensionality.

Summary: The proposed numerical realization yields a fully discrete reconstruction technique for the flow geometry and velocity. The technique is computationally cheap - the limitting factor is usually the assembling of the velocity forward operator T_h, which takes times of up to a minute. On the other hand, for sufficiently high data resolution and discretization we may expect that the theory of Section 2.4 transfers to the discrete approximations. Furthermore, we can expect accurate reconstructions for low data resolutions, since the voxelized model of Section 3.1 is included into the reconstruction process.

3.3 Validation

Now we consider the application of the method to measurements. The overall goal is to validate our expectations.

- The technique provides reasonable wall shear stress estimates for considerably low data resolutions that are feasible in the medical practice.
- The computed reconstructions of the geometry parameter and the flow velocity are for sufficiently high data resolution Tikhonov minimizers of the corresponding idealized reconstruction problems that were introduced in Section 2.4. Hence, the reconstruction errors satisfy the announced bounds in terms of the data error.

For this purpose, we consider several measurements, where *ground truth*, i.e. highly reliable reference values for the flow geometry, velocity and the wall shear stress are accessible. The investigated measurements share major flow features, in particular the formation of boundary layers and the Reynolds number Re, with typical flow regimes in the human aorta. Furthermore, the measurement conditions and parameters, in particular, the data resolution, are feasible for *in vivo* investigations as well.

The three investigated validating measurement series focus on different aspects of the reconstruction and are of increasing difficulty.

(I) In the first example, we consider *in vitro* measurements of a simple stationary flow in a simple geometry. The goal is to confirm the applicability of the technique to real magnetic resonance data.

(II) In the second example, we consider *in vitro* measurements of a more realistic flow in a simple geometry. The focus lies in the investigation, to what extent our method can deal with these complex flow conditions.

(III) The last example are *in silico* measurements of a stationary flow in a moderately deformed geometry in order to determine the stability of the reconstruction method against errors in the geometry reconstruction.

This allows for a comprehensive performance check of the proposed data driven method in regard to its capability to provide accurate wall shear stress estimates under *in vivo* conditions.

Finally we present illustrative applications to a 3D *in silico* measurement and an *in vivo* measurement of the ascending human aorta, where no *ground truth* is available.

3.3.1 Validation I: Stationary Flow in a Circular Geometry

In our first study, we investigate *in vitro* measurements of a flow with temporally constant volume flow rate $\dot{V}$ in a rigid pipe. In a cross-section of the pipe, we acquired data with four different resolutions between $h = 1.5$mm and $h = 0.3$mm, resembling the spectrum of feasible resolutions for *in vivo* applications.

The measurements were carried out in collaboration with our project partners on a whole-body 3T magnetic resonance imaging scanner (Prisma, Siemens Healthcare, Erlangen) at the University Medical Center Freiburg. An accurately controlled flow supply unit generated the water flow in the phantom, a glass pipe of sufficient length to allow the flow to become fully developed. For details about the experimental setup, we refer the reader to our more experiment-oriented publication [8].

Reference values. For pipe flows the Reynolds number is usually defined as

$$\mathrm{Re} := \frac{v\,L}{\nu},$$

where $\nu = \mu/\rho$ is the kinematic viscosity with density ρ and the dynamic μ viscosity, $L = 2R^\dagger$ is the pipe diameter and $v = 4\dot{V}/(\pi d^2)$ is the bulk velocity. It is known, that for $\mathrm{Re} < 2300$ we have a Hagen Poiseuille flow with analytically known velocity profile [79]. We consider the case $\mathrm{Re} = 5300$, that is beyond the critical Reynolds number $\mathrm{Re} = 2300$, leading to a turbulent pipe flow with no analytically known velocity profile. In fact, the flow is only statistically steady with varying time-dependent fluctuations. Hence, at a fixed time the flow is unique and not reproducable. However, magnetic resonance imaging incorporates some filtering and our major concern is to estimate the mean wall shear stress.

For the validation we fall back on a direct numerical simulation [52]. Thereby, a time dependent flow was simulated with constant volume flow rate. At the inflow, an obstacle created a perturbation and generated the turbulence. Behind this obstacle there was a sufficiently long inflow section to allow the flow to becomes fully developed. Downstream of this section, the flow was averaged in time and space to obtain the mean velocity profile. In fluid mechanics, an available direct numerical simulation is the gold standard and, hence, it serves as reference for our investigations.

Geometry registration. For all considered measurements, we reconstruct the geometry with 5 different *a priori* choices of the regularization parameter $\alpha = 1 \cdot 10^{-3} - 8 \cdot 10^{-3}$ and $\alpha = 10^3$. We will comment on the parameter choice by the discrepancy principle later on. First, we apply the pre-processing according to (3.9), where we use the homogeneous presegmentation algorithm. The iteratively regularized Gauss-Newton method, minimizing the Tikhonov functional, converges in few (< 5) iterations, where the previously computed stronger regularized reconstruction serves as initial value. To quantify the performance, we compute the $L^\infty(D)$ and $W^{1,\infty}(D)$ norms of the reconstruction errors $R_\alpha^\delta - R^\dagger$, where the reference pipe diameter is $R^\dagger = 12.94$mm. Note that according to the proposed analysis in Theorems 2.28 and 2.31 the former, amplified with the velocity derivative, contributes to the velocity error, while the $W^{1,\infty}(D)$ error contributes directly to the wall shear stress error.

The results are given in Table 3.1. In all cases, the reconstruction error is far below the resolution and hence, sub-voxel resolution is achieved. Regarding the data resolution, from the data error estimate $\delta \approx Ch^{1/2}$ according to (3.3) and the error estimate in Remark 2.25 we expect a convergence rate $h^{1/2}$. Indeed, the observed convergence with increasing

	$\alpha = 1 \cdot 10^3$	$\alpha = 8 \cdot 10^{-3}$	$\alpha = 4 \cdot 10^{-3}$	$\alpha = 2 \cdot 10^{-3}$	$\alpha = 1 \cdot 10^{-3}$
$h = 1.50$mm	**0.0380**	0.0644	0.0989	0.1320	0.1606
	0.0380	0.1213	0.2661	0.4274	0.5918
$h = 1.00$mm	**0.0138**	0.0371	0.0420	0.0469	0.0542
	0.0138	0.0850	0.1408	0.2003	0.2697
$h = 0.50$mm	**0.0088**	0.0387	0.0408	0.0412	0.0427
	0.0088	0.0967	0.1280	0.1562	0.1875
$h = 0.30$mm	**0.0018**	0.0154	0.0185	0.0215	0.0243
	0.0018	0.0464	0.0774	0.1109	0.1506

Table 3.1: Norms $\|R_\alpha^\delta - R^\dagger\|_{L^\infty(D)}$ (above) and $\|R_\alpha^\delta - R^\dagger\|_{W^{1,\infty}(D)}$ (below) of the geometry reconstruction error in [mm].

data resolution is roughly linear.

Remark 3.13. For an explanation, note that the $h^{1/2}$ factor in the data error was generated by the $L^2(\Omega_{\text{FOV}})$ norm. If we consider the $L^1(\Omega_{\text{FOV}})$ norm, than we would obtain $\delta \approx Ch$ for the noise level. Since, the approach of Cheng and Yamamoto [19] includes Banach spaces such as $L^1(\Omega_{\text{FOV}})$, one can expect reconstruction errors in the size of Ch by replacing the data space $Y = L^2(\Omega_{\text{FOV}})$ with $Y = L^1(\Omega_{\text{FOV}})$. Apparently, in practice we obtain similar results by treating the data in $Y = L^2(\Omega_{\text{FOV}})$.

Since the geometry is a circle, the radius function is constant and we are in the case $|R^\dagger|_k = 0$. Since we regularize with the seminorm, there is no bias due to over-smoothing for large regularization parameter α. According to Theorem 2.24, high regularization parameters are favored. This is confirmed from the numerical results. While the *a priori* choice $\alpha = 10^3$ amounts to *a priori* imposing the geometry to be circular with a constant parametrization R, the discrepancy principle choses a large regularization parameter without this knowledge, as can be observed from the low $L^\infty(D)$ reconstruction errors and the continuity of the forward operator.

Velocity approximation. For all considered measurements, we approximate the velocity with four different regularization parameters $\beta = 1 \cdot 10^{-8} - 6.4 \cdot 10^{-7}$. Thereby, we utilize the best geometry reconstruction R_α^δ with regularization parameter $\alpha = 10^3$. The velocity raw data are pre-processed according to (3.10), where we use the enhanced estimate $\overline{m}_i^\delta = \rho_{f,i}^\delta m_i^\delta + \rho_{e,i}^\delta (1 - m_i^\delta)$ for the raw magnitude with the fraction m_i^δ of the voxel contained in the reconstructed geometry.

The pre-processed velocity data for the measurement with the rather coarse resolution $h = 1$mm is depicted in Figure 3.3. The underlying velocity profile exhibits a boundary layer as illustrated in Figure 3.5. In Figures 3.4 and 3.6 we present velocity approximations, obtained with different regularization parameters. At first glance, the reconstruction with the higher regularization parameter is a good approximation in the flow domain, whereas the regularization with the lower regularization parameter seems to fit the data noise in the center. However, considering the distance between the isolines, the lower regularized

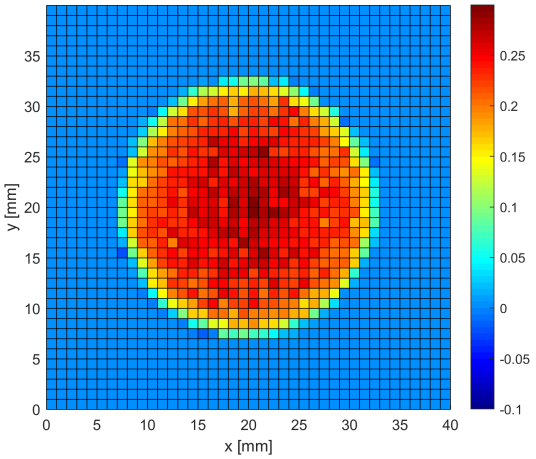

Figure 3.3: Pre-processed velocity data u^{ε} in the field of view Ω_{FOV}.

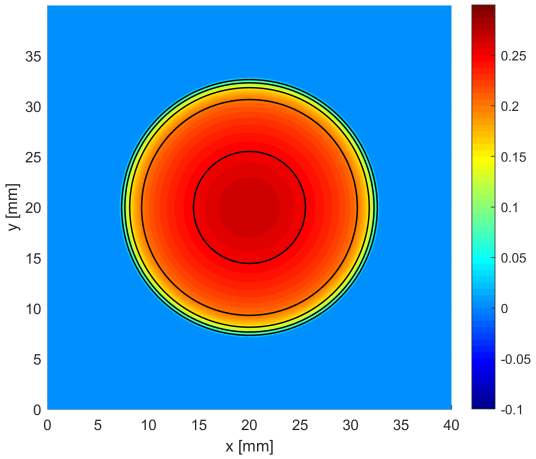

Figure 3.5: Reference velocity $u^{\dagger}$ from DNS in Ω_{FOV} with isolines.

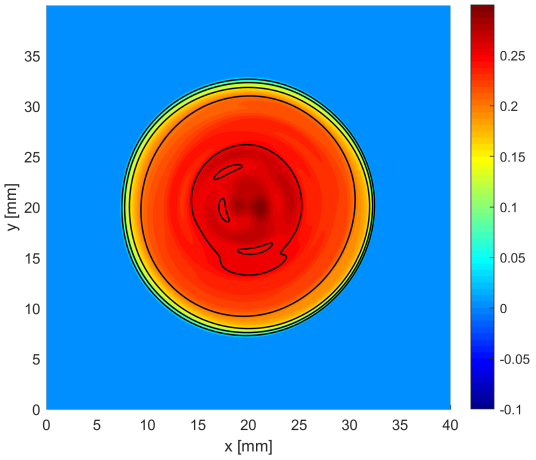

Figure 3.4: Velocity approximation $u_{\alpha,\beta}^{\delta,\varepsilon}$ for $\beta = 4 \cdot 10^{-8}$ in Ω_{FOV} with isolines.

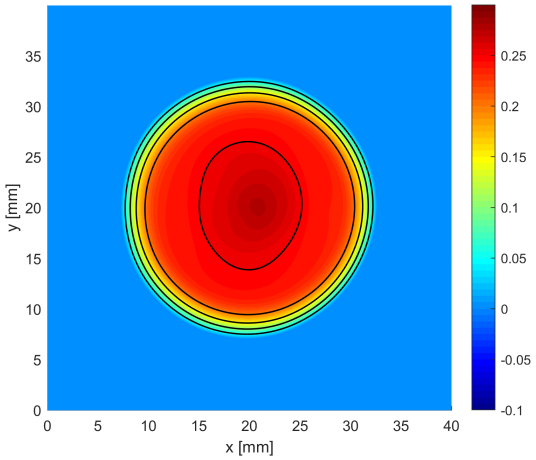

Figure 3.6: Velocity approximation $u_{\alpha,\beta}^{\delta,\varepsilon}$ for $\beta = 1 \cdot 10^{-5}$ in Ω_{FOV} with isolines.

	$\beta = 6.4 \cdot 10^{-7}$	$\beta = 1.6 \cdot 10^{-7}$	$\beta = 4 \cdot 10^{-8}$	$\beta = 1 \cdot 10^{-8}$
$h = 1.5$mm	0.0480	**0.0412**	0.0424	0.0479
	0.4898	**0.2893**	0.3773	0.8448
$h = 1.0$mm	0.0524	0.0458	**0.0448**	0.0464
	0.4792	0.2845	**0.2786**	0.7265
$h = 0.5$mm	0.0461	0.0417	**0.0415**	0.0421
	0.4239	0.2375	**0.2336**	0.5222
$h = 0.3$mm	0.0453	**0.0408**	0.0408	0.0413
	0.3996	0.1973	**0.1559**	0.3062

Table 3.2: Relative errors $E_{L^2}(v^{\delta,\varepsilon}_{\alpha,\beta})$ (above) and $E_{H^2}(v^{\delta,\varepsilon}_{\alpha,\beta})$ (below) of the velocity approximation.

$h = 1.5$mm	$h = 1.0$mm	$h = 0.5$mm	$h = 0.3$mm
0.0930	0.0009	0.0079	0.0108
0.1141	0.0365	0.0449	0.0290

Table 3.3: Relative errors $E_{\text{mean}}(\widehat{\tau}^{\delta,\varepsilon}_{\alpha,\beta})$ (above) and $E_{L^2}(\widehat{\tau}^{\delta,\varepsilon}_{\alpha,\beta})$ (below) of wall shear stress estimates.

approximation seems to be a far better approximation at the boundary. In fact, the depicted approximation with $\beta = 4 \cdot 10^{-8}$ is the best approximation obtainable.

To quantify the accuracy of a velocity approximation v, we introduce the relative errors

$$\begin{aligned} E_{L^2}(v) &:= \left\|v^\dagger - v\right\|_{L^2(\widehat{\Omega})} \,/\, \left\|v^\dagger\right\|_{L^2(\widehat{\Omega})}, \\ E_{H^2}(v) &:= \left\|v^\dagger - v\right\|_{H^2(\widehat{\Omega})} \,/\, \left\|v^\dagger\right\|_{H^2(\widehat{\Omega})}, \end{aligned} \tag{3.16}$$

where the reference velocity $v^\dagger$ is given by the direct numerical simulation [52]. The resulting approximation errors are listed in Table 3.2. The best approximation errors decrease only slightly with increasing data resolution h, while the optimal regularization parameter $\beta \approx 4 \cdot 10^{-8}$ is nearly independent of h. Note that the velocity noise level ε, estimated in (3.4), does not vanish for infinite data resolution. Beside the physical measurement error, there might be fluctuative deviations from the mean flow $v^\dagger$ that do not vanish in average over the relatively short data acquisition times.

Although the approximation errors are quite large, we can hope for good approximations of the wall shear stress, since a major contribution to the velocity error originates from interior fluctuations, while the approximation in the boundary layer seems accurate in Figure 3.4.

Wall shear stress estimation. The wall shear stress estimate τ is computed from the best geometry reconstruction R and the best velocity approximation v. For the quantification of errors, we consider the mapped estimated wall shear stress $\widehat{\tau}$ according to (2.49), the mapped reference wall shear stress $\widehat{\tau}^\dagger$ according to (2.48), and introduce the relative

errors

$$\begin{aligned} E_{\text{mean}}(\widehat{\tau}) &:= \left|\int_D \widehat{\tau}^\dagger - \widehat{\tau}\,\mathrm{d}(\varphi,s)\right| \left|\int_D \widehat{\tau}^\dagger\,\mathrm{d}(\varphi,s)\right|^{-1}, \\ E_{L^2}(\widehat{\tau}) &:= \|\widehat{\tau}^\dagger - \widehat{\tau}\|_{L^2(D)} \,/\, \|\widehat{\tau}^\dagger\|_{L^2(D)}. \end{aligned} \tag{3.17}$$

The results are listed in Table 3.3. As the nearly vanishing mean error for $h = 1$mm reveals, there is no structural under- or overestimation, respectively. The method produces reliable estimates with relative deviations below 10% for feasible data resolutions.

Comparison with a specialized wall shear stress estimator. Beside the direct numerical simulation, there are experimental laws for estimating the wall shear stress. The most famous is the friction factor formula of Moody [61]

$$\tau \;=\; \frac{1}{8}\,\lambda\,\rho\,v^2,$$

where the Darcy friction factor λ depends on the roughness of the wall and slightly on the Reynolds number [79].

A second example of experimental laws for wall shear stress estimation in fully developed turbulent shear flows is the Clauser method [20]. We introduce the friction velocity $u_\tau = \sqrt{\tau/\rho}$, where τ is the wall shear stress and ρ the mass density. With the distance to the wall y we define the logarithmic part of the boundary layer

$$30\,\frac{\nu}{u_\tau} \;\le\; y \;\le\; 100\,\frac{\nu}{u_\tau}.$$

Inside the logarithmic part of the boundary layer the velocity satisfies the logarithmic law of the wall [79]

$$u(y) \;=\; \frac{1}{\kappa}\,\log\left(\frac{u_\tau}{\nu}\,y\right)\,u_\tau \;+\; B\,u_\tau,$$

where κ and B are some constants. We have developed a generic non-linear regression method based on this principle that obtains a stable and accurate wall shear stress estimation from fitting the friction velocity to the magnetic resonance data [85]. By incorporating only data from a sector of the flow domain, this method is capable of producing localized estimates.

In Figure 3.7 we again present the pre-processed velocity data for the measurement with resolution $h = 1$mm. Alongside the wall shear stress estimate $\widehat{\tau}^{\delta,\varepsilon}_{\alpha,\beta}$ we display the distribution of the estimate $\widehat{\tau}_{\mathrm{C}}$ based on the Clauser method in Figure 3.8. Note that the Clauser method is based on the values of the logarithmic boundary layer, which is - for our investigation - roughly between $2-5$mm away from the boundary, while our estimate is based on the behaviour at the boundary. In this view, the velocity data reflect the distributions of the estimates. At this point, we emphasize that the estimated mean wall shear stress is in good accordance with the reference $\widehat{\tau}^\dagger = 0.1853$Pa and both estimates reveal a comparable variation: the proposed method is in no way inferior to a highly accurate specialized wall shear stress estimator.

Let us summarize our observation from this test in the following remark.

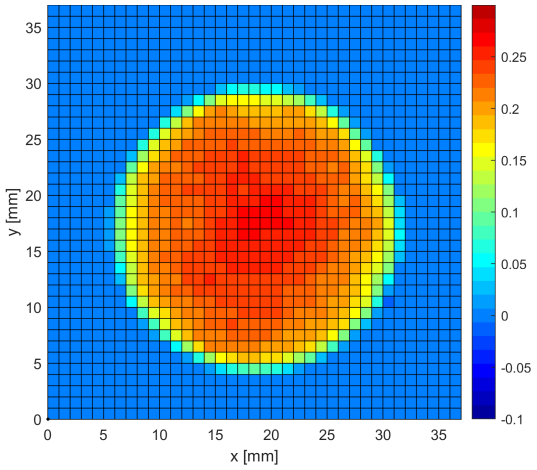

Figure 3.7: Pre-processed velocity [m/s], stationary flow, *in vitro*, resolution $h = 1\text{mm}$.

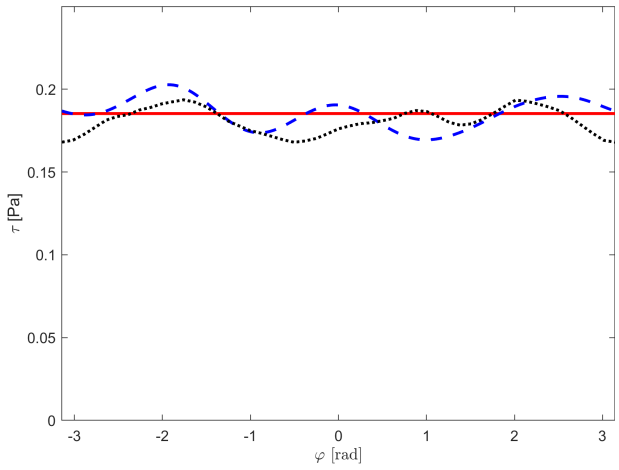

Figure 3.8: Wall shear stress in D: reference $\widehat{\tau}^{\dagger}$ (red), Clauser estimate $\widehat{\tau}_{\mathrm{C}}$ (black, dotted) and our estimate $\widehat{\tau}^{\delta,\varepsilon}_{\alpha,\beta}$ (blue, dashed).

Remark 3.14. The proposed data driven reconstruction method is able to identify a simple flow geometry with highest accuracy from magnetic resonance imaging data with feasible resolution. For simple velocity profiles, the proposed velocity approximation method is able to provide approximations of high accuracy in particular at the boundary, leading to nearly optimal wall shear stress estimates. Although the method benefits from high data resolution, it provides reliable wall shear stress estimators even for considerably low data resolution.

3.3.2 Validation II: Pulsating Flow in a Circular Geometry

Like in the previous example, we consider *in vitro* measurements of a flow in a rigid pipe. For a more application-oriented case, we consider an instationary periodic pipe flow, imitating the flow rate in the human aorta during the cardiac cycle with periode T. The temporal evoluation of the flow rate, which is adapted from [77], is depicted in Figure 3.9. We consider two sub-cases:

- $\mathrm{Re}_{\max} \approx 4000$, representing resting conditions, and
- $\mathrm{Re}_{\max} \approx 8000$, representing exercising conditions.

Additionally to the Reynolds number, instationary pulsating flows are characterized by the Womersley number that is usually defined by

$$\mathrm{Wo} := L\sqrt{\frac{2\pi}{T\,\nu}}$$

with kinematic viscosity ν and pipe diameter L. We use $\mathrm{Wo} \approx 20$, leading - apart from the flow geometry - to dynamic similarity with the aorta. Again, we consider four different

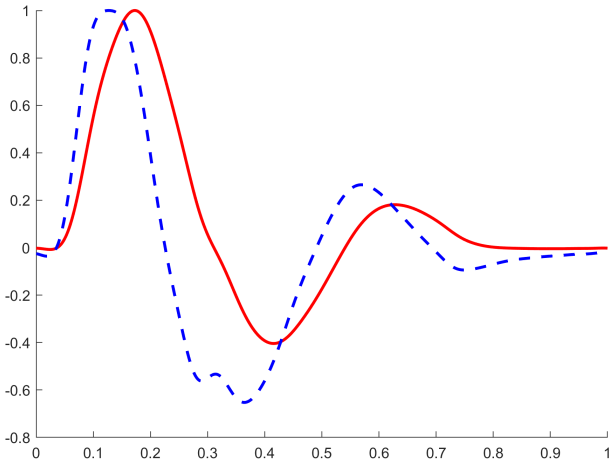

Figure 3.9: Normalized flow rate (red) and resulting wall shear stress (blue, dashed) over the cycle.

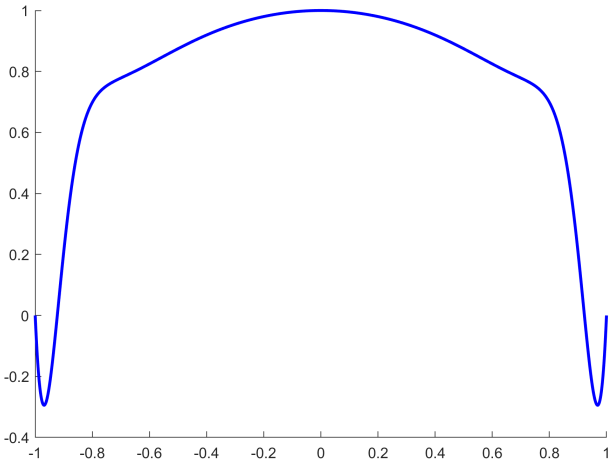

Figure 3.10: Normalized axial velocity $u(\cdot, t_0)$ at time $t_0 = 0.27T$ over the normalized diameter.

data resolutions. For details about the experimental setup, we refer the reader to our more experiment-oriented publication [8].

Reference values. For the computation of reference values, we will utilize an anaytical solution. Let us briefly present the solution, which was proposed by Womersley [98], and comment on its applicability.

The basic assumption is a laminar flow with vanishing fluctuations. From the symmetry assumption, the non-axial components of the velocity vanish and we have the following temporal Fourier series for the axial velocity u and the pressure p

$$\begin{aligned} u(x,y,z,t) &= \sum_{k\in\mathbb{Z}} e^{2\pi kt/Ti}\, u_k(x,y), \\ p(x,y,z,t) &= \sum_{k\in\mathbb{Z}} e^{2\pi kt/Ti}\, P_k\, z. \end{aligned}$$

With kinematic viscosity ν the flow governing Navier-Stokes equations (see Section 4.1) substantially simplify: the system becomes linear, allowing for separation of the temporal modes. Under normalization of the pressure gradient, the equation for mode $k \in \mathbb{Z}$ reads

$$\begin{cases} ikU_k - \nu\Delta U_k &= -1 \quad \text{in } \Omega_2, \\ U_k &= 0 \quad \text{on } \partial\Omega_2, \end{cases}$$

where Ω_2 is the cross-sectional circle. This linear Schrödinger equation has a unique analytical solution U_k [98] and we have the representation

$$u(x,y,z,t) = \sum_{k\in\mathbb{Z}} e^{kti}\, P_k\, U_k(x,y),$$

with $P_k \in \mathbb{Z}$ the only unknown. Integration over the cross-section yields the volume flow rate $\dot{V}(t)$. Hence, the coefficients P_k can be obtained from a Fourier transformation of the volume flow rate.

	$\beta = 1.6 \cdot 10^{-8}$	$\beta = 4 \cdot 10^{-9}$	$\beta = 1 \cdot 10^{-9}$	$\beta = 5 \cdot 10^{-10}$
$h = 1.6$mm	**0.0316**	0.0352	0.0474	0.0672
resting	0.7202	**0.6733**	0.7449	1.0551
$h = 0.8$mm	0.0247	**0.0237**	0.0260	0.0311
resting	0.6561	0.6038	**0.5842**	1.0146
$h = 0.5$mm	0.0243	**0.0233**	0.0236	0.0254
resting	0.6190	0.5641	**0.5323**	0.4982
$h = 0.3$mm	0.0252	**0.0246**	0.0254	0.0844
resting	0.5974	0.5243	**0.5132**	0.6845
$h = 1.6$mm	**0.0409**	0.0412	0.0507	0.0708
exercising	0.7377	**0.6896**	0.7605	1.1027
$h = 0.8$mm	0.0313	**0.0305**	0.0311	0.0350
exercising	0.6658	0.5727	**0.5699**	0.9777
$h = 0.5$mm	0.0299	**0.0297**	0.0303	0.0310
exercising	0.6230	0.5570	**0.5245**	0.8277
$h = 0.3$mm	0.0305	**0.0298**	0.0299	0.0306
exercising	0.5866	0.5104	**0.4744**	0.5964

Table 3.4: Relative errors $E_{L^2}(v^{\delta,\varepsilon}_{\alpha,\beta})$ (above) and $E_{H^2}(v^{\delta,\varepsilon}_{\alpha,\beta})$ (below) of the velocity approximation for physiologically pulsating flow.

Due to perturbations in the flow supply system, the real flow rates in the experiment differ. Hence, we utilize the integration of the data u^ε to obtain stable reconstructions of the flow rate. Using the Womersley solution, this unlocks access to the whole velocity profile and consequently the wall shear stress.

Let us finally remark on the accuracy of the reference value: although the peak Reynolds numbers would amount to a turbulent flow under steady conditions, the acceleration of the fluid leads to a laminarization. Using highly resolved laser Doppler velocimetry our project partners observed that the analytical solution is in good accordance with the physical flow [8] and can be treated as *ground truth*.

Geometry reconstruction. Regarding the geometry reconstruction, we refer to the previous subsection, since the geometry and the measurement technique remain the same, leading to similar results.

Velocity approximation. The velocity approximation was carried out as described in the previous subsection, however with four different regularization parameters $\beta = 5 \cdot 10^{-10} - 1.6 \cdot 10^{-8}$. Since the flow is instationary, the measurement is temporally resolved and the data is taken as snapshots of the velocity at phases $t_i = i \cdot \Delta t$ with $T/\Delta t \approx 40$ under resting conditions and $T/\Delta t \approx 80$ under exercising conditions.

To quantify the accuracy of a velocity reconstruction, in this subsection we modify the

introduced relative errors

$$\begin{aligned} E_{L^2}(v) &:= \max_{t_i} \left\| v^\dagger(t_i) - v\big(t_i\big) \right\|_{L^2(\widehat{\Omega})} / \left(\max_{t_i} \left\| v^\dagger(t_i) \right\|_{L^2(\widehat{\Omega})}\right), \\ E_{H^2}(v) &:= \max_{t_i} \left\| v^\dagger(t_i) - v\big(t_i\big) \right\|_{H^2(\widehat{\Omega})} / \left(\max_{t_i} \left\| v^\dagger(t_i) \right\|_{H^2(\widehat{\Omega})}\right). \end{aligned}$$

The results are listed in Table 3.4. Unsurprisingly, we observe similar results for resting and the rescaled exercising conditions, since the analytical solution and the numerical approximation are linear.

Regarding the regularization parameter, we obtain optimality for $\beta \approx 10^{-9}$, which is below the optimal regularization parameter in the previous subsection. As we can observe from the estimate in Proposition 2.27 under negligable error of the geometry reconstruction, this indicates a higher H^2 norm of the solution, i.e. the velocity profile exhibits considerably steeper boundary layers.

Considering the different resolutions, we obtain - apart from the coarsest resolution - similar results. While the L^2 errors are nearly optimal, the H^2 errors reveal large deviations. This indicates that the velocity profile is reasonably approximated in the interior of the flow domain, but the approximations exhibit large deviations at the boundary, which we should observe in the investigation of the wall shear stress.

Wall shear stress estimation. Again, we compute the wall shear stress estimate τ by the representation (2.49) using the best geometry reconstruction and velocity approximation. Since the wall shear stress is time-dependent, we modify

$$\begin{aligned} E_{\text{mean}}(\widehat{\tau}) &:= \max_{t_i} \left| \textstyle\int_D \widehat{\tau}^\dagger(t_i) - \widehat{\tau}(t_i)\, \mathrm{d}(\varphi, s) \right| \left(\max_{t_i} \left| \textstyle\int_D \widehat{\tau}^\dagger(t_i)\, \mathrm{d}(\varphi, s) \right| \right)^{-1}, \\ E_{L^2}(\widehat{\tau}) &:= \max_{t_i} \|\widehat{\tau}^\dagger(t_i) - \widehat{\tau}(t_i)\|_{L^2(D)} \,/\, \max_{t_i} \|\widehat{\tau}^\dagger(t_i)\|_{L^2(D)}. \end{aligned}$$

	$h = 1.5$mm	$h = 1.0$mm	$h = 0.5$mm	$h = 0.3$mm
resting conditions	0.3164	0.2416	0.2049	0.1955
	0.3258	0.2483	0.2138	0.1986
exercising conditions	0.3218	0.2222	0.2102	0.1980
	0.3328	0.2321	0.2182	0.2046

Table 3.5: Relative errors $E_{\text{mean}}(\widehat{\tau}^{\delta,\varepsilon}_{\alpha,\beta})$ (above) and $E_{L^2}(\widehat{\tau}^{\delta,\varepsilon}_{\alpha,\beta})$ (below) of the wall shear stress estimate for physilogically pulsating flow.

The wall shear stress estimates, listed in Table 3.5, reveal a serious deviation from the reference. Note that the mean values reveal a high error E_{mean} as well, which is different to the results of the previous section: we are faced with a systematic estimation error. The data resolution is - except from the lowest resolution - only of minor importance.

For an explanation of this deviation, we consider the temporal evoluation of the spatially averaged wall shear stress in Figure 3.11. Apparently, there is a phase difference between

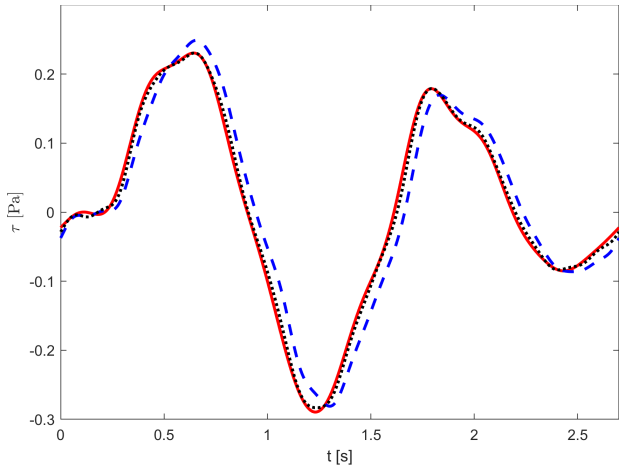

Figure 3.11: Temporal evolution of spatially averaged wall shear stress for physiologically pulsating flow: reference $\overline{\tau}^{\dagger}$ (red), LDA measurement $\overline{\tau}_{\mathrm{LDA}}$ (black, dotted) and estimate $\overline{\tau}^{\delta,\varepsilon}_{\alpha,\beta}$ (blue, dashed).

the analytical value $\overline{\tau}^{\dagger}$ (red) that is in high accordance with the highly resolved laser Doppler anemometry estimate $\overline{\tau}_{\mathrm{LDA}}$ (black, dotted), and the spatially averaged wall shear stress estimate $\overline{\tau}^{\delta,\varepsilon}_{\alpha,\beta}$.

For an explanation of this effect, consider the temporal evoluation of the volume flow rate and wall shear stress as illustrated in Figure 3.9. There is a phase difference between the wall shear stress and the trailing bulk velocity that can be physically explained with inertia effects [8]. As illustrated in Figure 3.10, the wall shear stress can already be negative, while the bulk velocity is clearly positive, leading to sharp boundary layers. Regarding the phase difference of the data driven estimate, we conclude that the spatial resolution of the data is too low: the voxelwise averaging incorporates too much interior data, causing the phase difference of the estimate.

In many practical applications, the phase difference is of minor importance and the wall shear stress estimates are much more reliable than the proposed error estimates imply. Concluding, we draw the following summarizing remark.

Remark 3.15. In a flow regime, that is dynamic similar to the flow in the human aorta, the proposed data based technique provides reasonable wall shear stress estimates, in particular for resolutions $h \leq 1\mathrm{mm}$. However, the considerably low data resolution causes a phase inaccuracy that remains present in the case of the highest possible data resolution.

3.3.3 Validation III: Stationary Flow in a Deformed Circle

As a last validating example, we consider a deformed geometry. For this purpose we fall back to *in silico* data, i.e. virtually generated data. Inspired from a reconstruction of a real human aorta, we define the exact geometry parameter

$$R^{\dagger}(\varphi) := \overline{R}^{\dagger}, (1 - 0.038\cos(2\varphi) - 0.061\sin(2\varphi) + 0.038\cos(3\varphi) + 0.023\sin(3\varphi)),$$

where the mean is given from our standard pipe radius $\overline{R}^{\dagger} = 12.94$mm. Note that by appropriate choice of the central point, the first mode of the perturbation vanishes. For the mapped velocity in the reference domain $v^{\dagger}$, we use the DNS velocity profile [52] that served already as reference in Subsection 3.3.1. The virtual data were acquired according to our model (3.5).

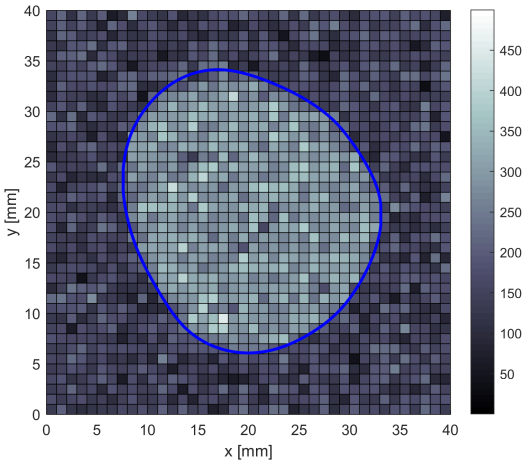

Figure 3.12: Magnitude raw data $\overline{m}_i^{\delta}$ with reconstructed flow geometry $\Omega(R_{\alpha}^{\delta})$ for the setup *in silico aorta* and resolution $h = 1$mm.

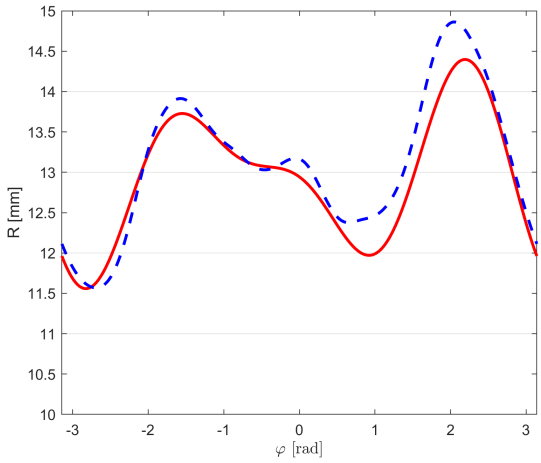

Figure 3.13: Exact parametrization $R^{\dagger}$ (red) and best reconsturction R_{α}^{δ} (blue, dashed) in D, horizontal lines correspond to $h = 1$mm.

Regarding the signal densities we consider two different setups, based on our experience about characteristic values of the magnitude data for real measurements *in vitro* and *in vivo*. The setup *in silico phantom* orients itself on measurements in flow phantoms that were considered in the previous subsections, the setup *in silico aorta* on measurements in the human aorta. The values are presented in Table 3.6. For both setups, we perform measurements with the same four different resolutions like in Subsection 3.3.1.

setup	ρ_f	ρ_e	noise level	SNR	CNR
in silico phantom	500	1	20	25	25
in silico aorta	300	150	40	7.5	3.75

Table 3.6: Parameter setups for the *in silico* measurements.

Geometry reconstruction. For all considered measurements, we reconstruct the flow geometry as outlined in Subsection 3.3.1. Since the geometry is not circular, we consider only four regularization parameters $\alpha = 1 \cdot 10^{-3} - 8 \cdot 10^{-3}$. The magnitude raw data of the *in silico aorta* measurement with resolution $h = 1$mm together with the reconstructed flow domain $\Omega(R_{\alpha}^{\delta})$, computed with optimal regularization parameter $\alpha = 4 \cdot 10^{-3}$, is illustrated in Figure 3.12. Optically, the boundary of the domain is well defined. A comparison between exact and reconstructed parametrization is displayed in Figure 3.13. The maximum error taken at $\varphi \approx 1$ is clearly below the voxel size and the mean registration error is far lower.

	$\alpha = 8 \cdot 10^{-3}$	$\alpha = 4 \cdot 10^{-3}$	$\alpha = 2 \cdot 10^{-3}$	$\alpha = 1 \cdot 10^{-3}$
$h = 1.5$mm	0.4340	0.2228	**0.1734**	0.1889
in silico phantom	0.9661	0.3120	**0.3023**	0.4581
$h = 1.0$mm	0.3373	0.1339	**0.1201**	0.1314
in silico phantom	0.7946	0.2315	**0.2020**	0.2666
$h = 0.5$mm	0.1022	**0.0332**	0.0414	0.0424
in silico phantom	0.2963	**0.0919**	0.1423	0.1602
$h = 0.3$mm	0.0486	**0.0163**	0.0165	0.0171
in silico phantom	0.1697	**0.0735**	0.0745	0.0799
$h = 1.5$mm	1.1218	0.9234	**0.8837**	0.9140
in silico aorta	1.6296	**1.1529**	1.2941	1.6644
$h = 1.0$mm	**0.3299**	0.3576	0.3984	0.4569
in silico aorta	**1.0807**	1.2772	1.5383	1.8986
$h = 0.5$mm	0.1808	**0.1061**	0.1347	0.1417
in silico aorta	0.5582	**0.3481**	0.4771	0.7057
$h = 0.3$mm	0.1064	0.0499	**0.0443**	0.0484
in silico aorta	0.4185	0.2685	**0.2197**	0.2946

Table 3.7: Norms $\|R_\alpha^\delta - R^\dagger\|_{L^\infty(D)}$ (above) and $\|R_\alpha^\delta - R^\dagger\|_{W^{1,\infty}(D)}$ (below) in [mm] of the geometry reconstruction error for the deformed circle.

Regarding the quantitative reconstruction errors, the results are given in Table 3.7. For different regularization parameters α, we observe the typical pattern: over-regularized solutions with large absolute errors and high deviations in the derivative for large regularization parameters and noisy reconstructions with large errors of the derivative for small regularization parameters. The optimal parameter is around $\alpha = 4 \cdot 10^{-3}$ and should be chosen by the discrepancy principle due to the behavior of the absolute errors and the continuity of the forward operator. Concerning the resolution, we observe for the setup *in silico phantom* roughly linear convergence and achieve considerable sub-voxel resolution, the maximum absolute errors are about 10% of the voxel size. For the setup *in silico aorta*, the reconstruction benefits even more from higher data resolution than under better measurement condtions.

Velocity approximation. The velocity approximation is carried out like in Subsection 3.3.1, using the best possible geometry reconstruction and five different regularization parameters β. For the quantification of approximation errors, we utilize the relative errors E_{L^2} and E_{H_2}, introduced in (3.16). Although we consider an unphysical flow, the velocity profile satisfies the no-slip condition, hence $v^\dagger \in \mathcal{D}(T)$ and we expect the results of Theorem 2.28 to hold.

The reconstruction errors are given in Table 3.8. Again, we observe the typical pattern: high regularized approximations show large errors due to over-smoothing, observed in the $L^2(\widehat{\Omega})$ and the $H^2(\widehat{\Omega})$ metric, whereas too low regularized noisy solutions suffer from large

$\beta = \cdots$	$6.4 \cdot 10^{-7}$	$1.6 \cdot 10^{-7}$	$4 \cdot 10^{-8}$	$1 \cdot 10^{-8}$	$2.5 \cdot 10^{-9}$
$h = 1.5$mm	0.0228	**0.0161**	0.0191	0.0222	0.0259
in silico phantom	0.4452	0.2768	**0.2450**	0.3792	0.7564
$h = 1.0$mm	0.0209	0.0093	**0.0092**	0.0126	0.0158
in silico phantom	0.4167	0.2164	**0.1789**	0.4107	0.7386
$h = 0.5$mm	0.0218	0.0089	**0.0042**	0.0042	0.0049
in silico phantom	0.4207	0.2392	**0.1315**	0.1689	0.2898
$h = 0.3$mm	0.0217	0.0089	0.0034	**0.0025**	0.0028
in silico phantom	0.4189	0.2406	0.1210	**0.1146**	0.1849
$h = 1.5$mm	**0.0393**	0.0425	0.0504	0.0592	0.0753
in silico aorta	**0.5263**	0.5336	0.7916	1.3355	2.6977
$h = 1.0$mm	0.0389	0.0309	**0.0307**	0.0364	0.0451
in silico aorta	0.5426	**0.4587**	0.5909	1.1303	2.0262
$h = 0.5$mm	0.0222	0.0126	**0.0125**	0.0146	0.0162
in silico aorta	0.4059	**0.2398**	0.2956	0.5431	0.9399
$h = 0.3$mm	0.0219	0.0104	**0.0078**	0.0085	0.0095
in silico aorta	0.4182	0.2485	**0.2148**	0.3785	0.6708

Table 3.8: Relative errors $E_{L^2}(v_{\alpha,\beta}^{\delta,\varepsilon})$ (above) and $E_{H^2}(v_{\alpha,\beta}^{\delta,\varepsilon})$ (below) of the velocity approximation in the deformed circle.

$H^2(\widehat{\Omega})$ errors. The $L^2(\widehat{\Omega})$ errors reveal that the discrepancy principle provides a nearly optimal parameter choice. At low data resolutions, the approximation benefits from higher resolution, while for the highest resolutions the gain becomes marginal, as it is expected from the estimate on the velocity data error (3.4). The reduction of the *signal-to-noise ratio* in the setup *in silico aorta* to roughly 1/4 reflects in an approximately doubled reconstruction error.

Wall shear stress estimation. Again, the wall shear stress estimators are computed from the best geometry reconstruction and velocity approximation. For both *in silico* measurements with resolution $h = 1$mm, the wall shear stress estimates are depicted in the parameter domain $D = (-\pi, \pi)$ in Figure 3.14. In particular, the reconstruction obtained from the *in silico phantom* measurement tracks the major features of the wall shear stress distribution. Note that the estimate for *in silico aorta* reveal a slight systematic underestimation. Presumably, the regularization parameter β of the velocity approximation is slightly too large, due to denoising of the interior velocity approximation.

For the assessment of the wall shear stress estimators we recall the relative error measures $E_{\text{mean}}(\widehat{\tau})$ and $E_{L^2}(\widehat{\tau})$ that were defined in (3.17). The comparison between the $L^2(D)$ error and the mean error confirm the observation that the wall shear stress is apparently underestimated. However, for the *in silico phantom* setup all measurements allowed for a reasonable wall shear stress quantification. Under difficult measurement conditions, a fine resolution of about $h = 0.5$mm is required for reasonable quantification of wall shear stress.

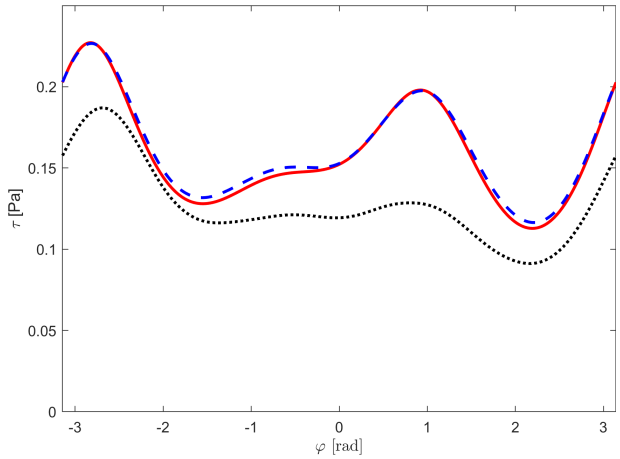

Figure 3.14: Distributed wall shear stress in parametric domain D: reference $\tau^\dagger$ (red) and estimates $\tau_{\alpha,\beta}^{\delta,\varepsilon}$ for *in silico phantom* (blue, dotted) and *in silico aorta* (black, dashed).

	$h = 1.5$mm	$h = 1.0$mm	$h = 0.5$mm	$h = 0.3$mm
in silico phantom	0.0527 0.0621	0.0374 0.0375	0.0240 0.0253	0.0033 0.0083
in silico aorta	0.1782 0.2019	0.1853 0.2097	0.0686 0.0716	0.0251 0.0331

Table 3.9: Relative errors $E_{\text{mean}}(\widehat{\tau}_{\alpha,\beta}^{\delta,\varepsilon})$ (above) and $E_{L^2}(\widehat{\tau}_{\alpha,\beta}^{\delta,\varepsilon})$ (below) of the wall shear stress estimate *in silico*.

In particular for the higher resolutions, the errors are substantially smaller than the errors of the velocity approximation and the estimators benefit in all cases like the geometry reconstruction from higher data resolution. This indicates a high impact of the geometry reconstruction on the wall shear stress estimates. Let us summarize our observations in the following remark.

Remark 3.16. Under laboratory measurement conditions, i.e. the setup *in silico phantom*, the proposed technique is able to compute reasonable wall shear stress estimates even in the case of a non-circular geometry. Under more realistic measurement conditions, the method relies upon a data resolution of at least $h = 0.5$mm to compute estimates with errors below 10%.

Sensitivity to geometry reconstruction. In our *in vitro* investigations, the underlying geometry is circular and reconstructed with high accuracy. The following results are inconspicuous with respect to geometry errors. The results *in silico* already indicated the impact of the geometry reconstruction. To verify the strong dependence of the wall shear stress estimate on the geometry reconstruction that was predicted from the theory in Theorem 2.31 and indicated from the results *in silico*, we perform a sensitivity analysis.

We consider the measurement *in silico phantom* with resolution $h = 1$mm and introduce

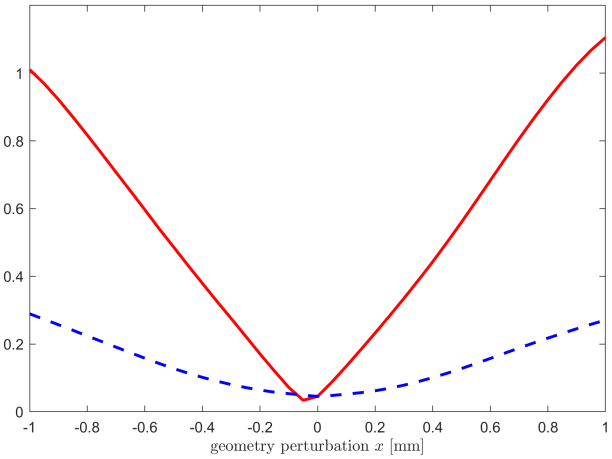

Figure 3.15: Sensitivity on the geometry: relative errors $E_{\text{mean}}(\widehat{\tau}_1)$ (red) and $E_{\text{mean}}(\widehat{\tau}_2)$ (blue, dashed) of estimates based on the perturbed parametrization R_1 respective R_2.

the perturbed reconstructed parametrizations $R_1(x)$ and $R_2(x)$ by

$$R_1(x;\varphi) \;:=\; R_\alpha^\delta(\varphi) \;+\; x, \quad R_2(x;\varphi) \;:=\; R_\alpha^\delta(\varphi) \;+\; x\,\sin(20\varphi).$$

We sample $x \in [-1\text{mm}, 1\text{mm}]$ and compute a velocity approximation with $\beta = 4{\cdot}10^{-8}$ based on the perturbed reconstruction, resulting in a wall shear stress estimate $\tau_1(x)$ or $\tau_2(x)$, respectively. The relative mean errors are depicted in Figure 3.15. While the sensitivity on the high oscillatory mode is surprisingly small, we confirm the importance of the accurate reconstruction of the lowest modes of the geometry parameter that was expected from Theorem 2.31. In this context, the regularization in the seminorm is a crucial ingredient for the performance of the reconstruction method, since the Tikhonov regularization introduces no additional bias to the mean value of the geometriy parameter. We record this observation in the following remark.

Remark 3.17. The wall shear stress estimate is highly sensitive to the geometry reconstruction and, in particular, to the lower modes of the geometry parameter. For the considered example a 0.1mm misregistration of the mean value of the geometry parameter causes a 10% error in the wall shear stress.

3.3.4 Illustration I: Aortic Aneurysm Phantom

For a representative 3D example, we apply the method to an *in silico* measurement of an aneurysm in the aortic arc. We used the *in silico phantom* setup with the resolution $h = 1\text{mm}$ for the data acquisition. In Figure 3.16, we present the reconstructed geometry that is optically hardly distinguishable from the reference geometry. A detailed view on the reconstruction error $R^\dagger - R_\alpha^\delta$ in Figure 3.18 confirms the sub-voxel accuracy of the reconstruction. Note that the noise level is substantially larger than the exterior signal density. Consequently, the exterior signal density is overestimated, leading to a shrinked reconstruction, that is recognized on the mainly positive value of the reconstruction error.

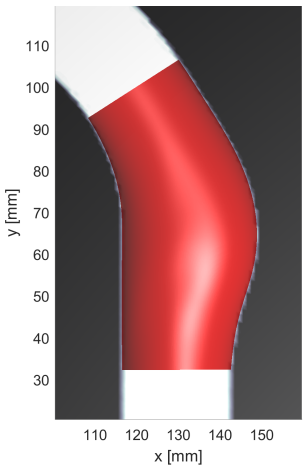

Figure 3.16: Reconstructed geometry with normalized magnitude in central slice.

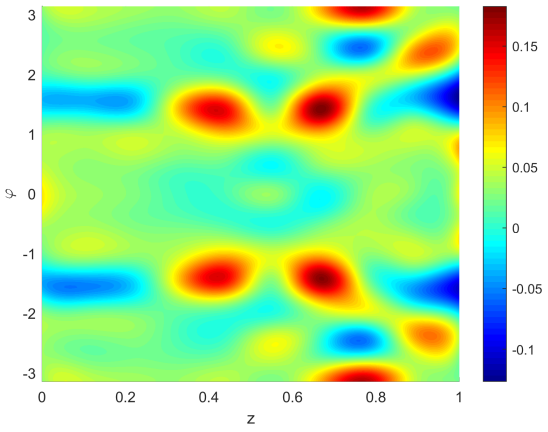

Figure 3.18: Relative geometry reconstruction error $(R^{\dagger} - R_{\alpha}^{\delta})/h$ in D.

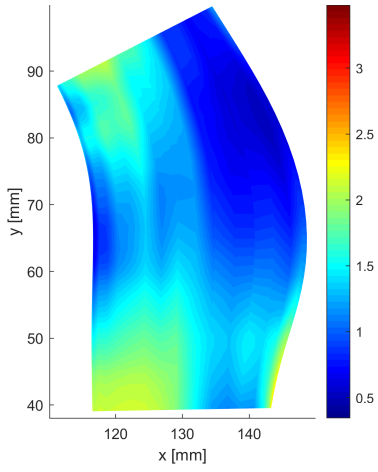

Figure 3.17: Reference wall shear stress $\tau^{\dagger}$ [Pa].

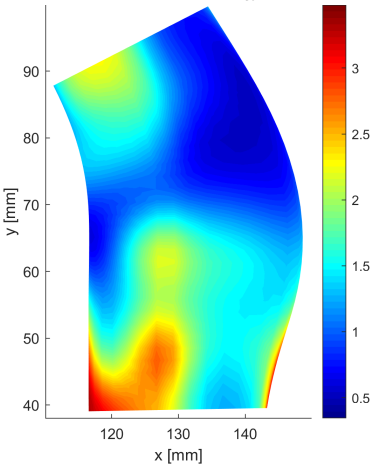

Figure 3.19: Wall shear stress estimate $\tau_{\alpha,\beta}^{\delta,\varepsilon}$ [Pa].

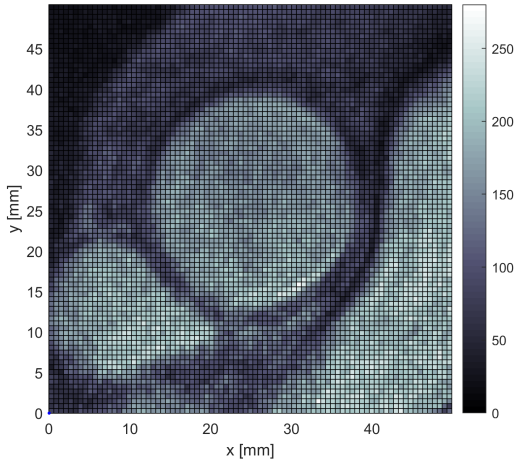

Figure 3.20: *In vivo* raw magnitude data $\overline{m}^{\delta}$ at peak systole.

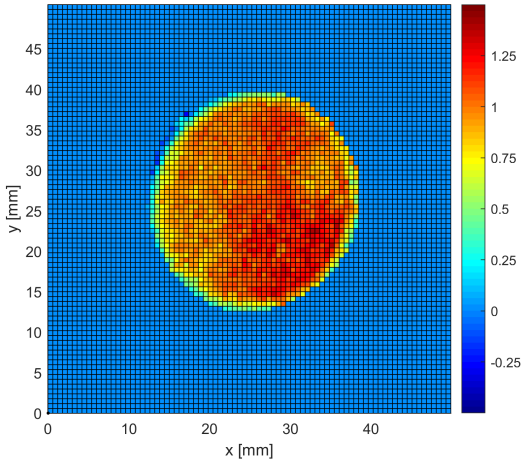

Figure 3.21: Pre-processed *in vivo* velocity data u^{ε} [m/s] at peak systole.

The underlying flow is derived from a simulation of a pulsatile flow in the whole aortic arc using the Smagorinsky turbulence model [40]. Note that due to limited resultion and applicability of the turbulence model, the validity of the simulation is questionable. Therefore, we utilize the data only for illustrative purposes. For the considered peak systolic phase, we found a mild separation of the velocity stream from the boundary at both the aneurysm wall and the inner boundary of the arc, leading to low wall shear stress $\tau^{\dagger}$ at these positions. Downstream to the aortic arc and the aneurysm we observe a reattachment of the flow, indicated by high wall shear stress $\tau^{\dagger}$. This behaviour is reproduced by the estimate $\tau^{\delta,\varepsilon}_{\alpha,\beta}$. However, we observe an over-estimation of the wall shear stress in the reattachment zones. Note that this region corresponds to high axial values in the parametric domain, where we in particular observe an underestimation of the geometry, explaining the enlarged high wall shear stress estimate in this region.

3.3.5 Illustration II: Ascending Human Aorta

Finally, we apply the method to *in vivo* data, considering a cross-sectional measurement of the ascending human aorta. The raw magnitude $\overline{m}^{\delta}$ is presented alongside the reconstructed geometry in Figure 3.20. The reconstruction R^{δ}_{α} was assessed as accurate by the radiologist Dr. Maximilian Russe (Department of Radiology, Medical Center, University of Freiburg, Germany). The reconstructed velocity in Figure 3.22, obtained with regularization parameter $\beta = 10^{-9}$, yields a reasonable approximation of the pre-processed velocity data in Figure 3.21. The wall shear stress with high values at the lower right and low values at the upper left section is depicted in Figure 3.23. The mean peak systolic wall shear stress estimate $\tau \approx 4.1$ Pa fits to the values reported in the literature [77].

Summary: We have provided a numerical realization of the reconstruction technique introduced in the previous chapter, and the continuous analysis of Section 2.4 transfers to

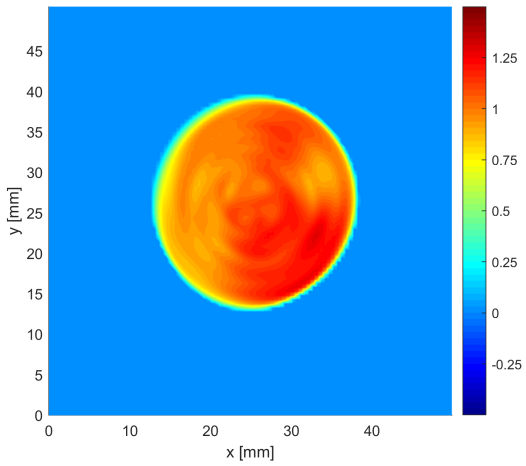

Figure 3.22: Reconstructed *in vivo* velocity $u_{\alpha,\beta}^{\delta,\varepsilon}$ [m/s] at peak systole.

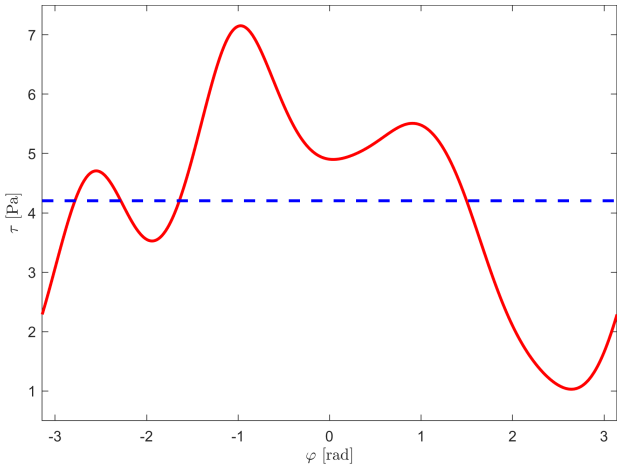

Figure 3.23: *In vivo* wall shear stress estimate $\tau_{\alpha,\beta}^{\delta,\varepsilon}$ (red) and spatial mean (blue, dashed) at peak systole.

the discrete solutions. Using a voxelized model for the actual magnetic resonance data, we were able to verify the applicability of the method for problems in the human aorta: The method provided convincing reconstructions of a simple flow with moderate boundary layer in a simple geometry from real magnetic resonance data. Under more difficult flow conditions or in a non-circular geometry, the reconstructions remain satisfactory. Even under more realistic measurement conditions, including higher noise, we obtained reliable reconstructions at least for high, but still feasible, data resolutions. The application to more complicated geometries delivers plausible results.

However, we observed two major issues. Regarding difficult but realistic flow conditions, the boundary layer was not accurately resolved due to low data resolution. The resulting wall shear stress estimates remain valuable for the most applications, but reveal a substantial phase inaccuracy. On the other hand, the method was found to rely on highly accurate reconstructions of the geometry that are accessible in our considerations due to high constrast-to-noise ratio under the experimental conditions. In the medical application the geometry reconstructions are most probably afflicted with higher inaccuracies. The subsequent chapter adresses these issues by incorporating a fluid dynamical model into the reconstruction process, while preserving the overall character of a data driven technique.

Chapter 4

Model Based Enhancement

In the previous chapters, we considered a purely data driven approach for the reconstruction of the flow geometry, velocity and wall shear stress. Apart from the general applicability of the presented approach, the examples in Section 3.3 also revealed two major issues arising in practice:

- the phase inaccuracy problem, indicating that boundary layers are not accurately resolved due to low data resolution, and
- the high sensitivity with respect to the flow geometry, in particular the lowest Fourier modes of the geometry parameter.

To avoid these issues, we incorporate additional *a priori* information about the physical laws gouverning the fluid motion that were so far neglected. Similar problems arise in the context of *data assimilation*, where measurement data are incorporated into a simulation to enhance the physical model [6]. While this leads to a model based paradigm, we suggest a more data driven approach. This strategy of enhancing a data based reconstruction by a suitable model has similarities with *physics-informed machine learning* [74].

Like in Chapter 2, we consider variational techniques to establish a mathematical formulation of the considered reconstruction problems as minimization problems. Together with the fluid dynamical model formulated as partial differential equation (PDE), this leads to PDE-constrained optimization problems, that are widely investigated [44, 91] and different techniques for their solution are available [10, 37].

In this chapter we present two specific applications of such *physics-informed* reconstruction problems, namely

- the enhancement of an initially given velocity approximation utilizing a fluid dynamical model in an accurately reconstructed flow geometry, representing the setup of Subsection 3.3.2 and
- the enhancement of the geometry approximation or the reduction of the sensitivity with respect to the geometry reconstruction utilizing the purely data based velocity approximation and a velocity approximation obtained from a fluid dynamical model.

In Section 4.1 we give a brief overview over the variational approach in data assimilation and suitable fluid dynamical models. The flow model underlying the subsequent

investigations is introduced and analyzed in Section 4.2. Afterwards we introduce a data assimilation technique for the enhancement of the initially given velocity approximation. In Section 4.3 we establish well-posedness of the technique and prove error bounds for the enhanced velocity approximation. Afterwards, we apply the proposed technique as well as some modifications to a basic flow reconstruction problem in Section 4.4. Finally, we present a model based enhancement strategy for the geometry reconstruction and reveal its basic applicability in Section 4.5.

4.1 Data Assimilation and Fluid Dynamical Models

Let us begin with a brief presentation of the existing variational approaches for data assimilation and mathematical flow models, that are suitable for the description of flow regimes arising in the human aorta.

Data Assimilation. For the presentation of the basic ideas, it suffices to consider an abstract flow model given by the operator equation

$$A(u)u \;=\; f.$$

Here u denotes the flow velocity, f the problem data, and $A(u)$ the mathematical model for the underlying physics, typically a system of partial differential equations with appropriate initial and boundary conditions. The second ingredient for the data assimilation are measurements, modelled by

$$y \;=\; M(u),$$

where M is the measurement operator. As for inverse problems, only approximations f^ε and y^ε of the model and measurement data are available in practice. The variational data assimilation approach leads to the minimization problem

$$\begin{aligned} \min_{u,f} J(u,f) \;\; := \;\; \min_{u,f} \;\; & \|M(u) - y^\varepsilon\|^2 \,+\, \alpha\, \|f - f^\varepsilon\|^2, \\ \text{s.t.} \;\; & A(u)u = f. \end{aligned} \tag{4.1}$$

The first term in (4.1) is the data misfit and ensures accordance to the measured data y^ε. The second term in (4.1) penalizes the deviation from the model. The scalar parameter $\alpha > 0$ weights between these misfits, for α large we obtain high accordance with the model. Formally, the Tikhonov regularization for the velocity approximation in Proposition 2.27 fits into this framework with $A(u)$ a smoothing operator and $f^\varepsilon = 0$. Indeed, the flow model typically exhibits smoothing properties and the data assimilation problem (4.1) can be seen and analyzed as inverse problem. Therefore, α is referred to as regularization parameter. Let us also remark, that the variational problem (4.1) is equivalent to optimal control problems. In this interpretation, the flow velocity u is manipulated by a controlled external force f to satisfy $M(u) = y^\varepsilon$.

For instationary models, one distinguishes between 3Dvar and 4Dvar, where in the former, the problems (4.1) are solved sequentially in time, while 4Dvar solves (4.1) globally in space and time [36]. Variational data assimilation techniques are widely used in the context of numerical weather prediction [6]. Beside providing some details on the realization, Foures et al. present the capabilities of variational data assimilation in the case of fairly limited measurement data and model accuracy, using a Reynolds averaged Navier-Stokes (RANS) model for the flow velocity with unknown Reynolds stresses [33]. Even the problem of reconstructing blood flow in the aorta is tackled with data assimilation techniques, where only magnetic resonance data in the interior of the aorta and away from the boundary are incorporated [54]. There are also cardiovascular applications of structurally equivalent optimal control problems, like the optimal design of a bypass configuration [58].

For the numerical solution there are various solution techniques available, for instance the Broyden–Fletcher–Goldfarb–Shanno (BFGS) algorithm [10] or sequential quadratic programming (SQP) methods [37]. In the aforementioned applications, the physical model requires high dimensional approximations of u and f, resulting in a high computational load. On the other hand we already have valuable approximations of the velocity by the purely data driven reconstruction available. Hence, we aim for incorporating these data already in the model $A(u)$ to simplify the data assimilation process.

Fluid dynamical models. In our application, we consider flows of an incompressible fluid, that is assumed to be Newtonian. The natural choice for the physical model $A(u)$ are the Navier-Stokes equations [32]

$$\partial_t u \,-\, 2\nu \operatorname{div}(Eu) \,+ \operatorname{div}(u \otimes u) \,+\, \nabla p = 0, \tag{4.2a}$$

$$\operatorname{div}(u) = 0. \tag{4.2b}$$

Here, u is the flow velocity with kinematic viscosity ν and strain rate tensor $Eu = (Du + (Du)^T)/2$ and p denotes the pressure. The first equation (4.2a) represents the balance of momentum and the second equation (4.2b) the balance of mass. The model has to be supplemented by boundary and initial conditions.

The non-linearity of the convection term $\operatorname{div}(u \otimes u)$ inflicts severe difficulties in the theory of solutions [31, 45, 56]. A linearization around an approximation w of the flow velocity - we may think about magnetic resonance data u^ε - leads to the Oseen problem, that allows for a comprehensive solution theory as we will see in the subsequent section.

Beside finite volume and finite difference methods, finite element approximations are suited for the numerical solution of (4.2). Regarding the incompressiblity constraint $\operatorname{div}(u) = 0$, so-called inf-sup-stable finite elements should be applied [39]. For high velocities, the convection term becomes dominant and suitable stabilization techniques like SUPG are indicated [14]. A further problem is the complexity of the arising flows, requiring high dimensional discretizations or turbulence models to account for unresolved energy dissipation [40, 76].

4.2 A Quasistationary Linearized Fluid Dynamical Model

Before we turn to the model informed enhancement problems, we have to introduce an appropriate flow model. We utilize an *a priori* given velocity approximation for the linearization and localization of the Navier-Stokes equations in time, ariving at a stationary Oseen problem. The model is formulated to compute a velocity update d (and a pressure p) for the initially given velocity approximation u^ε, resulting in the solution $(u,p) = (u^\varepsilon, 0) + (d,p)$. First, we introduce the Oseen problem for the velocity update, derive a weak formulation and a well-posedness result. Afterwards we define the solution (u,p) and comment on the connection to the Navier-Stokes equations.

4.2.1 Homogeneous Problem

Let Ω denote the flow domain and let $w \in L^3(\Omega)$ be an initial approximation of the flow velocity. With kinematic viscosity $\nu > 0$ we consider the system

$$\left\{ \begin{array}{rcll} -\nu\Delta d + \frac{1}{2}(w\cdot\nabla)d + \frac{1}{2}\mathrm{div}(d\otimes w) + \nabla p &=& b & \text{in } \Omega, \\ \mathrm{div}(d) &=& -g & \text{in } \Omega, \\ d &=& 0 & \text{on } \partial\Omega, \end{array} \right. \tag{4.3}$$

and assume the compatibility condition $\int\limits_\Omega g \,\mathrm{d}x = 0$.

Weak formulation. For ease of presentation, we state the weak formulation of (4.3) as operator equation. Let us introduce the diffusion operator $K \in \mathcal{L}(H^1_0(\Omega), H^{-1}(\Omega))$ by

$$\langle Kd, v\rangle \;:=\; \int\limits_\Omega \nu\,(Dd, Dv)\,\mathrm{d}x, \tag{4.4}$$

the convection operator $C \in \mathcal{L}(L^3(\Omega), \mathcal{L}(H^1_0(\Omega), H^{-1}(\Omega)))$ by

$$\langle C(w)d, v\rangle \;:=\; \frac{1}{2}\int\limits_\Omega ((w\cdot\nabla)d, v) \;-\; ((w\cdot\nabla)v, d)\;\mathrm{d}x \tag{4.5}$$

and the negative divergence $B \in \mathcal{L}(H^1_0(\Omega), L^2_0(\Omega))$ by $Bd := -\mathrm{div}(d)$. Now we can state the weak formulation of (4.3):

Problem 4.1. *Let $w \in L^3(\Omega)$, $b \in H^{-1}(\Omega)$ and $g \in L^2_0(\Omega)$. Find $(d,p) \in H^1_0(\Omega)\times L^2_0(\Omega)$ such that*

$$\begin{pmatrix} K + C(w) & B^* \\ B & 0 \end{pmatrix} \begin{pmatrix} d \\ p \end{pmatrix} = \begin{pmatrix} b \\ g \end{pmatrix} \text{ in } H^{-1}(\Omega)\times L^2_0(\Omega).$$

We verify, that Problem 4.1 is indeed a weak formulation of (4.3).

Lemma 4.2. *A strong solution $(d,p) \in H^2(\Omega)\times H^1(\Omega)\cap L^2_0(\Omega)$ of (4.3) solves Problem 4.1.*

Proof. Obviously, we have $d \in H_0^1(\Omega)$, $p \in L_0^2(\Omega)$ and $Bp = -\mathrm{div}(p) = g \in L_0^2(\Omega)$, using the compatibility condition. From integration by parts, we obtain for $v \in H_0^1(\Omega)$

$$\begin{aligned}\langle Kd + C(w)d + B^*p, v\rangle &= \int_\Omega \nu(Dd, Dv) + \tfrac{1}{2}\left[((w\cdot\nabla)d, v) - ((w\cdot\nabla)v, d)\right] - \mathrm{div}(v)p\,\mathrm{d}x \\ &= \int_\Omega \left(-\nu\Delta d + \tfrac{1}{2}(w\cdot\nabla)d + \tfrac{1}{2}\mathrm{div}(d\otimes w) + \nabla p, v\right)\,\mathrm{d}x = \langle b, v\rangle.\end{aligned}$$

□

Well-posedness of the weak formulation. Using the theory of Brezzi, we obtain a well-posedness result.

Proposition 4.3. *Problem 4.1 has a unique solution* $(u,p) \in H^1(\Omega) \times L_0^2(\Omega)$ *with*

$$\|u\|_{H^1(\Omega)} + \|p\|_{L^2(\Omega)} \le C\left(\nu + \|w\|_{L^3(\Omega)}\right)\left(\|b\|_{H^{-1}(\Omega)} + \|g\|_{L_0^2(\Omega)}\right)$$

Proof. Problem 4.1 has saddlepoint structure and we apply the theory of Brezzi with the convection diffusion operator $A = K + C(w)$.
Step 1: Continuity and ellipticity of the velocity operator. A is bounded, since

$$\begin{aligned}\langle Ad, v\rangle &= \int_\Omega \nu(Dd, Dv) + \frac{1}{2}((w\cdot\nabla)d, v) - \frac{1}{2}((w\cdot\nabla)v, d)\,\mathrm{d}x \\ &\le C\left(\nu + \|w\|_{L^3(\Omega)}\right)\|d\|_{H^1(\Omega)}\|v\|_{H^1(\Omega)}.\end{aligned}$$

Furthermore, A is elliptic, since due to the Poincare inequality and the antisymmetry of C

$$\langle Ad, d\rangle = \int_\Omega \nu(Dd, Dd)\,\mathrm{d}x \ge C\,\|d\|_{H^1(\Omega)}^2$$

Step 2: Continuity and inf-sup-condition of the operator B. Obviously we have B bounded, since $\|Bd\|_{L^2(\Omega)} = \|\mathrm{div}(d)\|_{L^2(\Omega)} \le C\|d\|_{H^1(\Omega)}$. Furthermore B satisfies

$$\inf_{q\neq 0\in L_0^2(\Omega)} \sup_{v\neq 0\in H_0^1(\Omega)} \frac{(Bv, q)}{\|v\|_{H^1(\Omega)}\,\|q\|_{L^2(\Omega)}} = \beta > 0, \tag{4.6}$$

for further details, we refer to the literature [39].
Step 3: Application of Brezzis theorem. Since A is bounded and elliptic and B is bounded and satisfies the inf-sup-condition (4.6), Brezzis theorem [13] yields the assertion. □

4.2.2 Inhomogeneous Problem

For the inhomogeneous problem, we consider initial approximations $u^\varepsilon \in H^1(\Omega)$ and $w \in L^3(\Omega)$ of the flow velocity, where u^ε defines the boundary data and w the convection. Addionally, we require model data $f \in H^{-1}(\Omega)$. Now we define a homogeneous problem

for the model update d. We introduce the right hand sides $b(u^\varepsilon, w, f) \in H^{-1}(\Omega)$ and $g(u^\varepsilon) \in L^2(\Omega)$ by

$$\begin{aligned} \langle b(u^\varepsilon, w, f), v\rangle &:= \langle f, v\rangle - \int_\Omega \nu(Du^\varepsilon, Dv) + \tfrac{1}{2}\left[((w\cdot\nabla)u^\varepsilon, v) - ((w\cdot\nabla)v, u^\varepsilon)\right] \mathrm{d}x, \\ g(u^\varepsilon) &:= \operatorname{div}(u^\varepsilon). \end{aligned} \tag{4.7}$$

If u^ε satisfies the compatibility condition, then $g(u^\varepsilon) \in L^2_0(\Omega)$ and the following flow model is well-defined.

Definition 4.4. *Let $u^\varepsilon \in H^1(\Omega)$, $w \in L^3(\Omega)$ and $f \in H^{-1}(\Omega)$ with $\int_{\partial\Omega} u^\varepsilon\, n\,\mathrm{d}s = 0$. Let (d, p) denote the solution of Problem 4.1 with $b = b(u^\varepsilon, w, f)$ and $g = g(u^\varepsilon)$ given by (4.7). The solution of the quasistationary linearized flow model is defined by*

$$u = u(u^\varepsilon, w, f) := u^\varepsilon + d. \tag{4.8}$$

We immediately obtain the following stability result.

Lemma 4.5. *Let $u_1, u_2 \in H^1(\Omega)$, $w \in L^3(\Omega)$ and $f_1, f_2 \in H^{-1}(\Omega)$ with $\int_{\partial\Omega} u_1 n\mathrm{d}s = \int_{\partial\Omega} u_2 n\mathrm{d}s = 0$. Then the corresponding solutions satisfy*

$$\|u(u_1, w, f_1) - u(u_2, w, f_2)\|_{H^1(\Omega)} \le C\left(\|tr_{\partial\Omega}(u_1 - u_2)\|_{H^{1/2}(\partial\Omega)} + \|f_1 - f_2\|_{H^{-1}(\Omega)}\right),$$

where C depends on $\|w\|_{L^3(\Omega)}$.

Proof. Let $\mathrm{tr}_{\partial\Omega}(u_1 - u_2) = 0$. Then $du = (u(u_1, w, f_1) - u(u_2, w, f_1) \in H^1_0(\Omega)$ and inserting du in the defining equations for the updates d_1 and d_2 yields $\|\nabla du\|^2 = 0$. Hence, $du = 0$. We conclude

$$u(u_1, w, f_1) - u(u_2, w, f_2) = u(u_1, w, f_1) - u(u_1 + E_0(\mathrm{tr}_{\partial\Omega}(u_2 - u_1), w, f_2),$$

where E_0 is the harmonic extension. Since b and g are linear and bounded with respect to $u^\varepsilon \in H^1(\Omega)$ and $f \in H^{-1}(\Omega)$, the assertion follows from the continuity of the harmonic extension and the well-posedness of the homogeneous Problem 4.1. □

For errors of the convective velocity, we obtain the following estimate.

Lemma 4.6. *Let $u^\varepsilon \in H^1(\Omega)$ with $\int_{\partial\Omega} u^\varepsilon n\mathrm{d}s = 0$ and $f \in H^{-1}(\Omega)$. Furthermore let $w_1, w_2 \in L^3(\Omega)$. For the associated solutions $u_i = u(u^\varepsilon, w_i, f)$ it holds*

$$\|u_1 - u_2\|_{H^1(\Omega)} \le C\left(\|u^\varepsilon\|_{H^1(\Omega)} + \|u_2\|_{H^1(\Omega)}\right)\|w_1 - w_2\|_{L^3(\Omega)}.$$

Proof. We observe, that $u_1 - u_2 = d_1 - d_2$. Subtracting the associated equations and using the fact, that C and b are linear with respect to w yields

$$\begin{pmatrix} K + C(w_1) & B^* \\ B & 0 \end{pmatrix}\begin{pmatrix} d_1 - d_2 \\ p_1 - p_2 \end{pmatrix} = \begin{pmatrix} (C(w_2 - w_1)d_2 + b(u^\varepsilon, w_1 - w_2, 0) \\ 0 \end{pmatrix}.$$

Since C and b are bounded with respect to w, we obtain

$$\|(C(w_2 - w_1)d_2 + b(u^\varepsilon, w_1 - w_2, 0)\|_{H^{-1}(\Omega)} \le C\,\|w_2 - w_1\|_{L^3(\Omega)}\left(\|d_2\|_{H^1(\Omega)} + \|u^\varepsilon\|_{H^1(\Omega)}\right).$$

The assertion follows from the estimate of Proposition 4.3. □

4.2.3 Connection with the Navier-Stokes Equations

Let us outline, in what extend solutions of the Navier-Stokes equations (4.2) are solutions of the quasistationary linearized flow model given by (4.8).

Lemma 4.7. *Let $T > t > 0$ and $(U, P) \in \mathcal{C}^1(0, T; H^2(\Omega)) \times \mathcal{C}(0, T; H^1(\Omega) \cap L_0^2(\Omega))$ denote a strong solution of the Navier-Stokes equations (4.2). Then $U(t)$ is a solution of the quasistationary linearized flow model with $f = -\partial_t U(t)$, $u^\varepsilon = U(t)$ and $w = U(t)$.*

Proof. Set $u = U(t)$. We compute for $u \in H^2(\Omega)$ with $\operatorname{div}(u) = 0$

$$2\operatorname{div}(Eu) \;=\; \operatorname{div}(Du) + \operatorname{div}((Du)^T) \;=\; \Delta u \;+\; \nabla(\operatorname{div}(u)) \;=\; \Delta u$$

and

$$\operatorname{div}(u \otimes u) \;=\; \operatorname{div}(u)\, u \;+\; (u \cdot \nabla)u \;=\; (u \cdot \nabla)u.$$

Also observe that $g(u) = \operatorname{div}(u) = 0$. Furthermore we have

$$\begin{aligned}
\langle b(u, u, f), v\rangle \;&=\; -\int_\Omega (\partial_t U(t) + \nu(Du, Dv) + \frac{1}{2}\left[((u \cdot \nabla)u, v) - (u \cdot \nabla)v, u)\right] \mathrm{d}x \\
&= -\int_\Omega (\partial_t U(t) - \nu\Delta u + \frac{1}{2}(u \cdot \nabla)u + \frac{1}{2}\operatorname{div}(u \otimes u), v)\, \mathrm{d}x \\
&= -\int_\Omega (\partial_t U(t) - 2\nu \operatorname{div}(Eu) + \operatorname{div}(u \otimes u), v)\, \mathrm{d}x \\
&= \int_\Omega (\nabla P(t), v)\, \mathrm{d}x.
\end{aligned}$$

Thus $U(t)$ is the solution of the quasistationary linearized flow model with corresponding pressure $P(t) \in L_0^2(\Omega)$. □

Let us summarize the concept of the proposed model.

Remark 4.8. The proposed fluid dynamical model in Definition 4.4 is conforming with the Navier-Stokes equations. Relying on an approximate velocity u^ε, defining the boundary data, a possible different approximation w, defining the convection, and an approximation of the negative temporal derivative f^ε, it makes the problem stationary and linear. Naturally, it allows for a spatial localization by restricting the computational domain. This leads to a significant simplification of the following reconstruction problems.

We now turn to the model informed enhancement methods.

4.3 Velocity Enhancement

For the enhancement of the velocity reconstructions u^ε obtained in Chapters 2 and 3, we now investigate a variational data assimilation approach based on the linearized quasistationary flow model in Definition 4.4. We establish well-posedness of the approach, derive error bounds for the reconstruction error and present the corresponding first order optimality system and a finite element approximation. Similar results have been obtained in [24, 81].

4.3.1 Reconstruction Method and Well-Posedness

Let Ω denote the flow geometry and u^ε an initial approximation of the flow velocity. For the enhancement of the velocity approximation we consider with regularization parameter $\alpha > 0$ the following data assimilation problem

$$\begin{aligned} \min_{d\in H_0^1(\Omega), f\in L^2(\Omega)} \quad & \|d\|^2_{L^2(\Omega)} + \alpha \, \|f - f^\varepsilon\|^2_{L^2(\Omega)} \\ \text{s.t.} \quad & \begin{cases} Kd + C(u^\varepsilon)d + B^T p &= b(u^\varepsilon, u^\varepsilon, f), \\ Bd &= g(u^\varepsilon), \end{cases} \end{aligned} \tag{4.9}$$

where b and g are given by (4.7). For $f^\varepsilon = -\partial_t u^\varepsilon$ the arising system is consistent with the Navier-Stokes equations. We observe, that this problem fits into the aforementioned framework of data assimilation, leading to a PDE-constrained minimization problem.

First, we observe the well-posedness of the reconstruction method.

Lemma 4.9. *Let $u^\varepsilon \in H^1(\Omega)$ with $\int_{\partial\Omega} u^\varepsilon n \mathrm{d}s = 0$ and let $f^\varepsilon \in L^2(\Omega)$. Then the reconstruction problem (4.9) has a unique solution $d^\varepsilon_\alpha \in H^1_0(\Omega)$ and $f^\varepsilon_\alpha \in L^2(\Omega)$.*

Proof. We establish well-posedness of the data assimilation problem by a standard argument [91]. Consider the control-to-state operator $d(f)$ solving Problem 4.1 with $b = b(u^\varepsilon, u^\varepsilon, f)$ and $g = g(u^\varepsilon)$. The reduced functional is defined by

$$J : L^2(\Omega) \to \mathbb{R}, \quad J(f) = \|d(f)\|^2_{L^2(\Omega)} + \alpha \|f - f^\varepsilon\|^2_{L^2(\Omega)}.$$

Obviously, a minimizer of J is a minimizer of (4.9) and vice versa, the control f of a minimizer of (4.9) is a minimizer of J. Since J is bounded from below by 0, there is a minimizing sequence (f_n). Since $J(f) \geq \alpha \|f - f^\varepsilon\|^2_{L^2(\Omega)}$, the sequence is bounded and a subsequence f_m converges weakly to f^ε_α. d is affine and bounded. Therefore, J is continuous, convex and consequently weakly lower semi-continuous. Hence, we have $J(f^\varepsilon_\alpha) \leq \liminf J(f_m) = \inf_{f\in L^2(\Omega)} J(f)$. Therefore, f^ε_α is a minimizer of J and the strict convexity of J ensures the uniqueness. □

4.3.2 Error Bounds for the Reconstruction Error

Let $u^\dagger \in H^1(\Omega)$ denote the exact incompressible flow velocity with associated data $f^\dagger \in L^2(\Omega)$, i.e. $u^\dagger = u(u^\dagger, u^\dagger, f^\dagger)$. Now we establish error bounds on the deviation of the model based velocity enhancement.

Proposition 4.10. *Let $u^\varepsilon \in H^1(\Omega)$ with $\int_{\partial\Omega} u^\varepsilon n \mathrm{d}s = 0$ and let $f^\varepsilon \in L^2(\Omega)$. Set $u^\varepsilon_\alpha := u^\varepsilon + d^\varepsilon_\alpha$ with d^ε_α the unique minimizer of the reconstruction problem (4.9). Then*

$$\|u^\varepsilon_\alpha - u^\dagger\|_{H^1(\Omega)} \leq C \left(\|f^\dagger - f^\varepsilon\|_{L^2(\Omega)} + \frac{1+\sqrt{\alpha}}{\sqrt{\alpha}} \varepsilon \right)$$

with $\varepsilon = \|u^\varepsilon - u^\dagger\|_{L^3(\Omega)} + \|u^\varepsilon - u^\dagger\|_{H^{1/2}(\partial\Omega)}$.

Proof. Let $u_1 = u(u^\dagger, u^\varepsilon, f^\dagger)$ denote the solution of the quasistationary linearized flow model (4.8) with convection data u^ε, boundary data $u^\dagger$ and model data $f^\dagger$. By Lemma 4.6 we obtain

$$\|u^\dagger - u_1\|_{H^1(\Omega)} \leq C \|u^\dagger\|_{H^1(\Omega)} \|u^\dagger - u^\varepsilon\|_{L^3(\Omega)} \leq C\,\varepsilon$$

Let $u_2 = u(u^\varepsilon, u^\varepsilon, f^\dagger)$ denote the solution with convection data u^ε, boundary data u^ε and model data $f^\dagger$. By Lemma 4.5 we obtain

$$\|u^\dagger - u_2\|_{H^1(\Omega)} \leq C\varepsilon + C\|u^\dagger - u^\varepsilon\|_{H^{1/2}(\partial\Omega)} \leq C\varepsilon.$$

Let $d_2 = u_2 - u^\varepsilon = u(u^\varepsilon, u^\varepsilon, f^\dagger) - u^\varepsilon$. By the definition of f^ε_α as minimizer of J, we observe

$$\alpha\|f^\varepsilon_\alpha - f^\varepsilon\|^2_{L^2(\Omega)} \leq J(f^\varepsilon_\alpha) \leq J(f^\dagger) = \|d_2\|^2_{L^2(\Omega)} + \alpha\,\|f^\dagger - f^\varepsilon\|^2_{L^2(\Omega)}.$$

Applying the estimate on the state $u_2 - u^\dagger$ yields

$$\|d_2\|_{L^2(\Omega)} \leq \|u_2 - u^\dagger\|_{L^2(\Omega)} + \|u^\dagger - u^\varepsilon\|_{L^2(\Omega)} \leq C\varepsilon.$$

Hence, we have

$$\|f^\varepsilon_\alpha - f^\varepsilon\|_{L^2(\Omega)} \leq \|f^\dagger - f^\varepsilon\|_{L^2(\Omega)} + \frac{1}{\sqrt{\alpha}} C\varepsilon.$$

With the stability estimate of Proposition 4.3 we compute

$$\|d^\varepsilon_\alpha - d_2\|_{H^1(\Omega)} \leq C\|f^\varepsilon_\alpha - f^\dagger\|_{L^2(\Omega)} \leq C\|f^\varepsilon - f^\dagger\|_{L^2(\Omega)} + \frac{1}{\sqrt{\alpha}} C\varepsilon.$$

The assertion follows from the previously obtained estimate for $u_2 - u^\dagger$. □

Let us briefly compare the data assimilation problem (4.9) with the purely data driven velocity approximation in Theorem 2.28 under the assumption of a perfect geometry reconstruction. Both results provide error bounds for the reconstruction error, measured in a stronger norm, by the absolute data error, measured in L^2 or L^3 respectively. In this regard we may interprete the data assimilation problem as regularizing filter. However, the data error was amplified with the potentially large factor $|u^\dagger|_{H^2(\Omega)}$ in the data driven reconstruction, while we expect only moderate amplification for the model informed enhancement, given a suitable approximation of $f^\dagger$ and only small absolute velocity values in a region around the boundary.

Let us finally consider the rates. If we estimate $f^\dagger = -\partial_t u^\dagger$ by a centered difference quotient with temporal spacing Δt, we may assume $\|f^\dagger - f^\varepsilon\|_{L^2(\Omega)} \leq (\Delta t)^2 + \varepsilon/\Delta t$. Furthermore, we may assume by interpolation, that $\|u^\dagger - u^\varepsilon\|_{L^3(\Omega)} \leq \varepsilon^{3/4}$. Neglecting the boundary error, we arrive for $\alpha = \mathcal{O}(1)$ at the error estimate

$$\|u_\alpha^\varepsilon - u^\dagger\|_{H^1(\Omega)} \leq C\left((\Delta t)^2 + \varepsilon/\Delta t + \varepsilon^{3/4}\right).$$

In comparison with the error estimate for the purely data driven velocity reconstruction $\|u^\varepsilon - u^\dagger\|_{H^1(\Omega)} \leq C\varepsilon^{1/2}$, we may hope for an enhancement of the reconstruction.

4.3.3 Numerical Realization

For the numerical solution of the linearized data assimilation problem (4.9), we introduce the Lagrangian function

$$\begin{aligned}\mathcal{L}(d,p,f;\lambda,\pi) := \; & \tfrac{1}{2}\|d\|^2_{L^2(\Omega)} + \tfrac{\alpha}{2}\|f - f^\varepsilon\|^2_{L^2(\Omega)} \\ & + \langle A(u^\varepsilon)d + B^*p - b(u^\varepsilon,u^\varepsilon,f),\lambda\rangle + (Bd - g(u^\varepsilon),\pi)\,.\end{aligned} \tag{4.10}$$

with convection diffusion operator $A(u^\varepsilon) = K + C(u^\varepsilon)$. Forcing the derivatives of $\mathcal{L}$ to vanish yields the Karush-Kuhn-Tucker conditions. Since the constraints are linear, the function is quadratic and strictly positive. Thus, the first order optimality condition is a necessary and sufficient condition for a minimizer [91]. The differentiation with respect to the control f leads to

$$f = f^\varepsilon + \lambda/\alpha.$$

We eliminate the control f and introduce the operator $M \in \mathcal{L}(H_0^1(\Omega), H^{-1}(\Omega))$ with $\langle Mu, v\rangle := \int_\Omega (u,v)\mathrm{d}x$. Then the optimality system reads

$$\left\{\begin{array}{rcrcrcl} Md & & + & A(u^\varepsilon)^*\lambda & + & B^*\pi & = & 0, \\ & & & B\lambda & & & = & 0, \\ A(u^\varepsilon)d & + & B^*p & - \tfrac{1}{\alpha}M\lambda & & & = & b(u^\varepsilon,u^\varepsilon,f^\varepsilon), \\ Bd & & & & & & = & g(u^\varepsilon). \end{array}\right. \tag{4.11}$$

Finite element approximation. For the numerical discretization, we utilize the $\mathcal{P}^2 - \mathcal{P}^1$ Taylor-Hood element that is known to be inf-sup stable [96]. The straightforward discretization of the KKT-system 4.11 is the optimality system of the associated discrete quadratic minimization problem, and from its strict convexity well-posedness of the discrete system follows immediately. Convergence of the discrete minimizers to the minimizer of the continuous problem (4.9) can be established [44]. Apart from applying direct solvers, the solution using MINRES is possible. Regarding preconditioners, Zulehner [101] proposed a block diagonal approximation in the case of low convection $u^\varepsilon \approx 0$, where the pressure Schur complement blocks can be approximated by explicitly computable matrices [27]. Appropriate multigrid approximations lead to an optimal and efficient solver [12]. However, the convection term brings down efficacy of the preconditioner for high Reynolds numbers.

4.4 Numerical Illustration of the Velocity Enhancement

In Subsection 3.3.2 we observed that the purely data driven reconstruction exhibits a phase inaccuracy due to low data resolution. Now, we apply model informed reconstruction techniques in order to enhance the approximation. Besides the method proposed in the previous section, we consider two modifications regarding the treatment of the non-linear convection term. In Subsection 4.4.1, we present the modifications and briefly comment on the numerical realization. In Subsection 4.4.2 the experimental setup is described, followed by an illustration of the data assimilation results in Subsection 4.4.3.

4.4.1 Velocity Enhancement Strategies

Let us recall the data assimilatin problem introduced in the previous section: Let Ω be the fixed computational domain with $u^\varepsilon \in H^1(\Omega)$ and $f^\varepsilon \in L^2(\Omega)$ initial approximations of the flow velocity and data. We consider the following strategies.

Linearized Navier-Stokes method. The previously presented enhancement strategy reads

$$\begin{aligned} \min_{d\in H_0^1(\Omega), p\in L_0^2(\Omega), f\in L^2(\Omega)} \quad & \|d\|^2_{L^2(\Omega)} + \alpha\|f - f^\varepsilon\|^2_{L^2(\Omega)} \\ s.t. \quad & \begin{cases} Kd + C(u^\varepsilon)d + B^*p &= b(u^\varepsilon, u^\varepsilon, f), \\ Bd &= g(u^\varepsilon). \end{cases} \end{aligned} \tag{4.12}$$

Let $d_\alpha^\varepsilon \in H_0^1(\Omega)$ denote the velocity enhancement, given as velocity part of the unique minimizer of (4.12). The enhanced velocity is defined by $u_\alpha^\varepsilon = u^\varepsilon + d_\alpha^\varepsilon \in H^1(\Omega)$ and we refer to this as linearized Navier-Stokes (LNS) method. In view of Proposition 4.10 we assume that u_α^ε is a better approximation than u^ε. This motivates the following strategy.

Iterated linearized Navier-Stokes. We iteratively utilize the previously computed enhanced approximation to linearize the model around the new velocity approximation. This leads to a sequence of quadratic minimization problems. The iterated linearized Navier-Stokes (INS) method reads: Set $u^0 := u^\varepsilon$ and iterate

- solving the quadratic minimization problem

$$\begin{aligned} \min_{d\in H_0^1(\Omega), p\in L_0^2(\Omega), f\in L^2(\Omega)} \quad & \|d\|^2_{L^2(\Omega)} + \alpha\|f - f^\varepsilon\|^2_{L^2(\Omega)} \\ s.t. \quad & \begin{cases} Kd + C(u^{k-1})d + B^*p &= b(u^\varepsilon, u^{k-1}, f), \\ Bd &= g(u^\varepsilon), \end{cases} \end{aligned} \tag{4.13}$$

- setting $u^k := u^{k-1} + d_\alpha^{\varepsilon,k}$ with $d_\alpha^{\varepsilon,k}$ the velocity update given by (4.13) and
- terminating, when $\|d_\alpha^{\varepsilon,k}\|_{H^1(\Omega)} < \text{tol}$.

The enhanced velocity is $u_\alpha^\varepsilon := u^k$ after achieving convergence of the iteration. In a previous investigation [24,81] the iterated method proved to be superior to the linearized (LNS) method. The iterates are solutions of linearized flow equations and the method prefers small regularization parameters α, leading to small updates $d_\alpha^{\varepsilon,k}$ for the convective velocity. In this view, the method may be seen as a generalized data driven approach.

Non-linear Navier-Stokes method. A third possibility for dealing with the non-linear convection term is to utilize $u = u^\varepsilon + d$ as convective velocity, leading to the non-linear Navier-Stokes (NNS) method. For the numerical solution, we utilize a standard approach and consider the reduced problem

$$\min_f J(f) \;:=\; \|u(f) - u^\varepsilon\|^2_{L^2(\Omega)} + \alpha \|f - f^\varepsilon\|^2_{L^2(\Omega)}, \tag{4.14}$$

where $u(f) = u^\varepsilon + d$ is the velocity part of the solution of the non-linear stationaray Navier-Stokes model given by

$$\begin{array}{rcl} Kd + C(u^\varepsilon + d)d + B^*p &=& b(u^\varepsilon, u^\varepsilon + d, f), \\ Bd &=& g(u^\varepsilon). \end{array} \tag{4.15}$$

For the minimization of (4.14) we apply a gradient method. The formal representation of the gradient requires the computation of the sensitivities $\partial u(f)/\partial f$, which is highly expensive. Using the implicit function theorem in an adjoint approach [41], the gradient can be represented by an adjoint $\lambda \in H_0^1(\Omega)$, that is defined by the linearized equation

$$\left\{ \begin{array}{rcl} K\lambda + C(u^\varepsilon + d)\lambda - \widetilde{C}(u^\varepsilon + d)^*\lambda + B^*\pi &=& d, \\ B\lambda &=& 0. \end{array} \right. \tag{4.16}$$

with the additional operator arising from differentiating $C(u^\varepsilon + d)$ and defined by

$$\langle \widetilde{C}(u)^*\lambda, w\rangle := \frac{1}{2}\int_\Omega ((w\cdot\nabla)u, \lambda) - ((w\cdot\nabla)\lambda, u)\,\mathrm{d}x, \quad \forall \lambda \in H_0^1(\Omega).$$

For the minimization we apply the BFGS algorithm that computes an approximation on the Hessian ∇J, amounting to the iteration

(i) forward solve: given f^k, compute $u(f^k)$ from (4.15),

(ii) adjoint solve: given $u(f^k)$, compute λ^k from (4.16),

(iii) update: given λ^k, set $\nabla J(f^k) = \alpha(f^k - f^\varepsilon) + \lambda$ and perform the BFGS update to obtain the new iterate f^k.

Similar non-linear methods are widely used for data assimilation purposes [33, 54, 58]. In our study, these non-linear techniques represent the model based approach for the data assimilation, since the computation benefits from a large regularization parameter α and the iterates u^k are exact solutions of non-linear flow models.

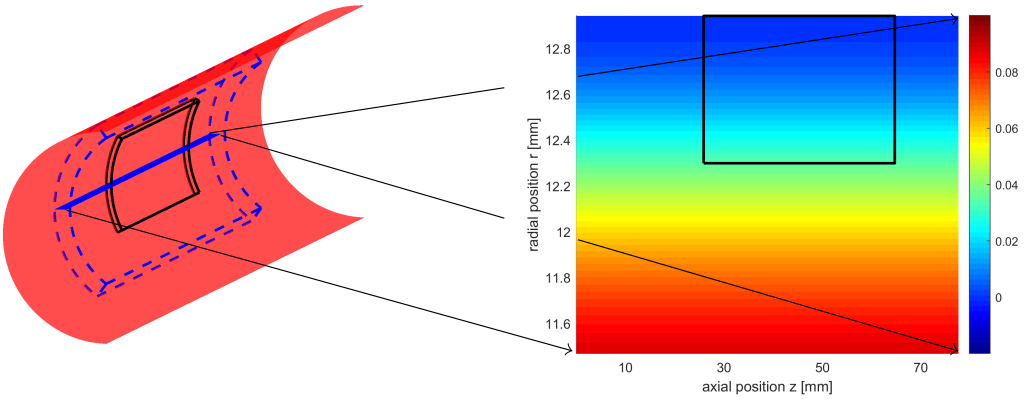

Figure 4.1: Longitudinal section (left, red) with flow direction from bottom left to top right, computational domain Ω (left, blue, dashed), the subdomain $\Omega_{\text{eval}} \subset \Omega$ (left, black) for the quantification of reconstruction errors and the slice Ω_{ill} (left, blue thin slice) used for illustrations as well as the axial component of the velocity $u^\dagger(t)$ [m/s] in the slice Ω_{ill} (right). Note the anisotropic aspect ratio. Flow direction from bottom left to top right. $\Omega_{\text{ill}} \cap \Omega_{\text{eval}}$ is the black rectangle.

4.4.2 Setup for the Velocity Enhancement

The geometric setup for the following computations is depicted in Figure 4.1. We consider a flow in a straight ideal pipe. The computational domain Ω for the data assimilation is a segment of a hollow cylinder. The overall goal is the enhancement of the wall shear stress estimates. Therefore, we introduce an evaluation domain $\Omega_{\text{eval}} \subset \Omega$ representing the inner boundary layer. To reduce the effect of the perturbed Dirichlet boundary data, the evaluation domain Ω_{eval} is located away from the artificial boundary of Ω. For illustrations of the velocity reconstructions, we display the reconstructions in a thin slice Ω_{ill} in the radial-axial plane of thickness 1.5mm and length 80mm.

Regarding the flow, we consider a physiologically pulsating Womersley flow in the pipe. As outlined in Subsection 3.3.2, the analytical solution $u^\dagger$ is computable from the temporal evolution of the volume flow rate in Figure 3.9 under knowledge of the fluid parameters (here: blood with dynamic viscosity $\mu = 0.004$ Pa s and density $\rho = 1050$ kg/m^3), the temporal periode $T = 1$s, the pipe diameter $2R^\dagger = 25.885$mm and the peak Reynolds number. We distinguish between $\text{Re}_{\max} = 1000$ and $\text{Re}_{\max} = 4000$ with the latter representing resting conditions of the cardiovascular system. For $\text{Re}_{\max} = 1000$ and evaluation phase $t = 0.23T$ the axial component of the velocity $u^\dagger(t)$ in Ω_{ill} is depicted in Figure 4.1.

We conduct virtual measurements with data resolution $h = 1$mm under the setup *in silico phantom* (see Table 3.6). We apply the purely data driven technique as outlined in Section 3.2. The geometry reconstruction yields an approximation of the geometry parameter determining the flow geometry. From the validation study, we may assume that a sufficiently accurate flow geometry Ω is available.

The purely data driven velocity approximation provides an approximation $u_i^\varepsilon \in H^1(\Omega)$ of the flow velocity $u^\dagger(t_i)$ at temporal snapshots $t_i = t + i\Delta t$. With period $T = 1$s, we used $T/\Delta t = 40$ amounting to a feasible repetition time of $\Delta t = 25$ms [8].

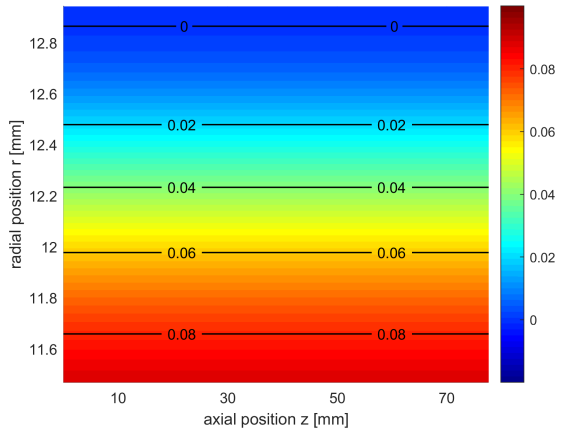

Figure 4.2: Exact axial velocity $u^\dagger(t)$ [m/s] in Ω_{ill}.

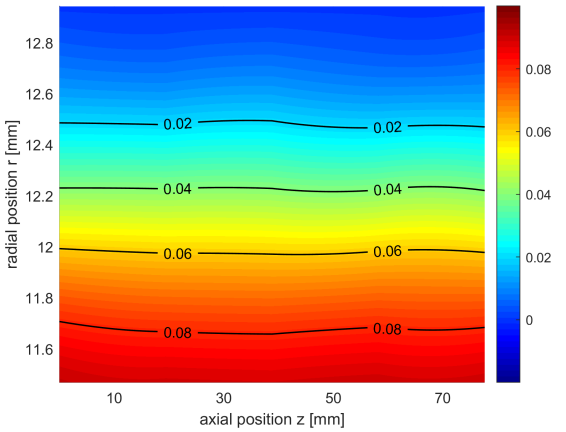

Figure 4.3: Purely data driven approximation u_0^ε [m/s] in Ω_{ill}.

The considered phase $t = 0.23T$ is short after the first zero of the wall shear stress, but before the first zero of the flow rate (see Figure 3.9). The exact axial velocity $u^\dagger(t)$ and the purely data driven approximation u_0^ε are depicted in Figures 4.2 and 4.3. As we can observe from the zero velocity isoline for the exact velocity, there is a small backflow in the inner boundary layer reflecting the negative wall shear stress, while the bulk flow is clearly positive. In overall, the corresponding purely data driven velocity approximation reproduces the velocity profile quite accurate, note in particular the nearly exact position of the $u = 0.02 - 0.08$m/s isolines and remember the fact, that the radial thickness of the presented slice is only 1.5 voxel sizes. However, the zero isoline is missing and hence, the reconstructed wall shear rate positive. This perfectly fits to the observation in Subsection 3.3.2, where the wall shear stress estimate was found to be trailing behind the exact wall shear stress.

4.4.3 Numerical Results

In order to reconstruct the backflow, we apply the three presented data assimilation techniques. The arising linearized flow models and optimality conditions are discretized using the $\mathcal{P}^2 - \mathcal{P}^1$ Taylor-Hood finite element approximation. The aspect ratio of the geometry Ω is quite high, leading to a small pressure-velocity inf-sup-constant [65]. Consequently, the spectral equivalence of the pressure Schur complement and its explicit approximations degenerates [27], making the preconditioners infeasible. Therefore, the arising linear systems were solved with a direct solver under a rather coarse resolution. To allow for an adequate resolution of the high velocity gradients in normal direction, we again utilize an anisotropic grid spacing in radial direction. To reduce errors resulting from the approximation of the geometry with rather few elements, we utilize $\mathcal{P}^2$ mapping functions to establish curved elements, a technique that is often referred to as *isoparametric finite element method* [30].

Note that the analytical solution is a solution of the Navier-Stokes equations, i.e.

$$\begin{aligned} Kd + C(u^\dagger(t))d + B^*p &= b(u^\dagger(t), u^\dagger(t), -\partial_t u^\dagger(t)), \\ Bd &= g(u^\dagger(t)) \end{aligned}$$

has the solution $d = 0$ (and $p = p^\dagger(t)$). Let $u^\varepsilon \in H^1(\Omega)$ denote the purely data driven velocity approximation of $u^\dagger(t)$. Naturally, the velocity approximation u^ε is nearly solenoidal and with a small modification in the outflow part we ensure $\int_{\partial\Omega} u^\varepsilon n \mathrm{d}s = 0$. Furthermore, we have velocity approximations u^ε_{-1} and u^ε_{+1} of the axial velocity $u^\dagger(t_{-1})$ and $u^\dagger(t_{+1})$ at the previous and following temporal snapshots. We define the approximation

$$f^\varepsilon := \frac{u^\varepsilon_{-1} - u^\varepsilon_{+1}}{2\Delta t} \tag{4.17}$$

of the model data, that may be seen as regularized approximation of the negative temporal velocity derivative $f^\dagger = -\partial_t u^\dagger(t)$. We use $\alpha = 0.001$ for the regularization parameter. Now, the methods are carried out as outlined in Subsection 4.4.1.

Linearized Navier-Stokes method. The enhanced velocities u^ε_α resulting from the linearized Navier-Stokes method are depicted in Figures 4.4 and 4.6 for the peak Reynolds numbers $\mathrm{Re}_{\max} = 1000$ and $\mathrm{Re}_{\max} = 4000$, respectively. Although the input data differ due to the linear purely data driven velocity approximation only in a parameter, the enhanced velocities substantially differ due to the convection that is quadratic in the Reynolds number. Since a linearized convection term is considered, linearization errors lead to clear perturbations in the case of the higher Reynolds number.

However, the axial perturbations are optically overated due to the anisotropic scaling of the plots. Additionally and most important, we observe the reconstructed backflow from the present $u^\varepsilon_\alpha = 0$ isoline, that was missing for the purely data driven approximation u^ε. Hence, the LNS is capable to provide a clear improvement of the velocity in the inner boundary layer.

Iterated Navier-Stokes method. In Figures 4.5 and 4.7 we present the results of the data assimilation under the iterated Navier-Stokes method (INS). Again, the backflow in the most inner boundary layer is identified. Compared with the results of the LNS method, we observe reduced perturbations, in particular for the case of the higher Reynolds number. Note that the method at least formally eliminates linearization errors.

Non-linear Navier-Stokes method. The results of the non-linear Navier-Stokes method (NNS) are optically similar to those of the INS method and, therefore, not presented. The NNS method is clearly the most expensive of the presented techniques, however, we observe the pay-off in the reconstruction errors.

Quantification of the reconstruction errors. To quantify the reconstruction errors, we restrict the velocity errors to the evaluation domain Ω_{eval}. The enhanced approximations

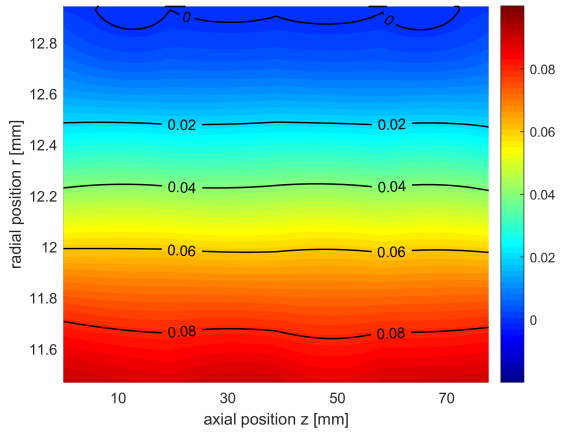

Figure 4.4: Reconstruction u_α^ε of the axial velocity [m/s] with LNS ($\mathrm{Re}_{\max} = 1000$) in Ω_{ill}.

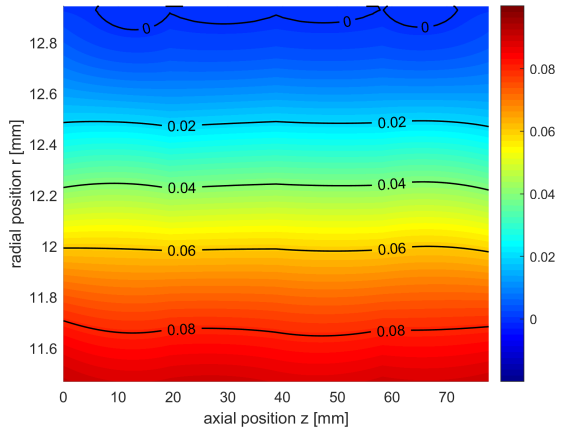

Figure 4.5: Reconstruction u_α^ε of the axial velocity [m/s] with INS ($\mathrm{Re}_{\max} = 1000$) in Ω_{ill}.

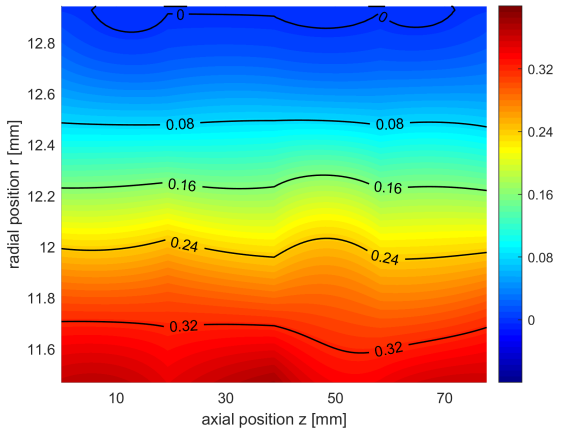

Figure 4.6: Reconstruction u_α^ε of the axial velocity [m/s] with LNS ($\mathrm{Re}_{\max} = 4000$) in Ω_{ill}.

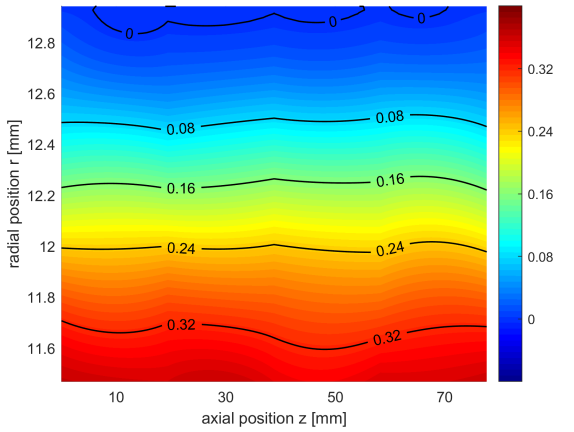

Figure 4.7: Reconstruction u_α^ε of the axial velocity [m/s] with INS ($\mathrm{Re}_{\max} = 4000$) in Ω_{ill}.

$u_\alpha^\varepsilon \in H^1(\Omega_{\mathrm{eval}})$ lead to distributional wall shear stress estimates. We quantify the performance with respect to the wall shear stress estimation therefore by the H^1 error in the thin boundary layer and the deviation in the mean wall shear stress, amounting to a functional evaluation. Note that the full wall shear stress error in the distributional space continuously depends on the H^1 error. We compute relative errors with respect to the corresponding purely data driven errors and introduce

$$E_{H^1}(u) := \frac{\|u - u^\dagger\|_{H^1(\Omega_{\mathrm{eval}})}}{\|u^\varepsilon - u^\dagger\|_{H^1(\Omega_{\mathrm{eval}})}}, \quad E_{\mathrm{WSS}}(u) := \frac{|\int_\Gamma \tau(u) - \tau^\dagger \,\mathrm{d}s|}{|\int_\Gamma \tau^\epsilon - \tau^\dagger \,\mathrm{d}s|}.$$

The results for the mean wall shear stress errors $E_{\mathrm{WSS}}(u_\alpha^\varepsilon)$ are given in Table 4.1. We observe an error reduction by more than 85% for all considered data assimilation strategies. Considering the more general $H^1(\Omega_{\mathrm{eval}})$ errors in Table 4.2, a significant error reduction compared to the purely data driven approximation is preserved. However, the LNS

setup	LNS	INS	NNS
$\mathrm{Re}_{\max} = 1000$	0.1227	0.1131	0.1206
$\mathrm{Re}_{\max} = 4000$	0.1433	0.0972	0.1233

Table 4.1: Relative reduction of the mean wall shear stress error $E_{\mathrm{WSS}}(u_\alpha^\varepsilon)$ for the different data assimilation methods with respect to the purely data driven reconstruction.

setup	LNS	INS	NNS
$\mathrm{Re}_{\max} = 1000$	0.2070	0.1926	0.1929
$\mathrm{Re}_{\max} = 4000$	0.4307	0.3081	0.2297

Table 4.2: Relative reduction of the $H^1(\Omega_{\mathrm{eval}})$ error $E_{H^1}(u_\alpha^\varepsilon)$ for the different data assimilation methods with respect to the purely data driven reconstruction.

method is clearly affected from linerization errors for higher Reynolds numbers, while the NNS method reveals nearly no dependence on larger convective forces. The INS method represents a fair trade-off between accuracy of the enhanced velocity approximation and computational effort. Let us summarize our observations in the following remark.

Remark 4.11. As expected, the incorporation of a data driven localized and linearized flow model in a data assimilation approach may lead to a substantial improvement of the purely data driven velocity approximations in the inner boundary layer and consequently an enhancement of the corresponding wall shear stress estimates. In particular for large convective forces, additional improvements may be obtained by eliminating the linearization error in the convective term, as it is done in the INS and NNS methods.

4.5 Geometry Enhancement

In the numerical validation of the purely data driven technique we observed a high sensitivity of the velocity approximation u_β^ε with respect to the geometry parameter R, in particular the lowest Fourier mode of R. This motivates the following enhancement strategy for the geometry parameter R: compare the purely data driven velocity approximation $u_\beta^\varepsilon(R)$ with some accessible other velocity approximations with only mild dependence on the geometry. For this velocity, we have two natural choices - the velocity data u^ε or a model based velocity $u(R)$.

Modified geometry forward operator. Let $v_\beta^\varepsilon(R)$ denote the unique Tikhonov minimizer of the velocity approximation problem (2.47) with fixed regularization parameter $\beta > 0$ and geometry parameter $R \in \mathcal{G}$, where the set of admissible geometry parameters $\mathcal{G}$ is given by (2.36). Let $u_\beta^\varepsilon(R) \in L^2(\Omega_{\mathrm{FOV}})$ denote the corresponding velocity in the physical domain, extended by zero to the field of view. We introduce the forward operator

$$F : \mathcal{G} \cap H^3(D) \subset H^3(D) \to L^2(\Omega_{\mathrm{FOV}}), \quad F(R) := u_\beta^\varepsilon(R). \tag{4.18}$$

Data based geometry enhancement. We compare the reconstructed velocity with the original velocity data $u^\varepsilon \in L^2(\Omega_{\mathrm{FOV}})$ in the field of view. Hence, we introduce the data based geometry enhancement functional

$$J_{\mathrm{data}}(R) \;:=\; \|F(R) - u^\varepsilon\|^2_{L^2(\Omega_{\mathrm{FOV}})}. \tag{4.19}$$

This amounts to the data misfit in the Tikhonov functional of the velocity approximation.

Model based geometry enhancement. Another possibility is to compare the purely data driven velocity approximation $u^\varepsilon_\beta(R)$ with a velocity obtained from a flow model. For $R \in \mathcal{G}$ define $u(R)$ according to Definition 4.4 as solution of the quasistationary linearized flow model with convective velocity $w = u^\varepsilon_\beta(R)$, boundary data $u^\varepsilon_\beta(R)$ and model data $f = f^\varepsilon_\beta(R)$ on the flow domain $\Omega(R)$, where the model data are obtained by (4.17) from velocity approximations of the adjacent time-steps. Finally, we introduce the model based geometry enhancement functional

$$J_{\mathrm{model}}(R) \;:=\; \|F(R) - u(R)\|^2_{L^2(\Omega_C)}, \tag{4.20}$$

where $\Omega_C \subseteq \cap_{R\in\mathcal{G}}\,\Omega(R)$ is a suitable subset of all admissible geometries.

Sensitivity of the velocities on the geometry. Obviously, the original velocity data u^ε is independent of the geometry reconstruction. Regarding the dependence of the model solution $u(R)$ on the geometry parameter, we make the following remark.

Remark 4.12. Model velocities depend smooth on the geometry parameter. We only sketch a proof, for a rigorous analysis we refer to the literature [43, 48]. Let us map the model velocity $u(R)$ to the reference domain, yielding $v(R) = u(R) \circ \Phi_R$ with Φ_R the forward transformation associated with the geometry parameter R. Skipping the boundary conditions, we can write the governing partial differential equations after mapping to the reference domain in abstract form as

$$\text{find } (v,q) \in H^1(\widehat{\Omega}) \times L^2_0(\widehat{\Omega}) \text{ with } E((v,q),R) = 0 \text{ in } H^{-1}(\widehat{\Omega}) \times L^2_0(\widehat{\Omega}). \tag{4.21}$$

With mapped convection $\hat{w}_R \in L^3(\widehat{\Omega})$ and model data $\hat{f}_R \in L^3(\widehat{\Omega})$ the system E reads

$$\begin{aligned}\langle E((v,q);R),(\lambda,\pi)\rangle = \int_{\widehat{\Omega}} \nu\, I_R\,(A_R v, A_R\lambda) + \frac{1}{2}\, I_R\,[((\hat{w}_R\, A_R\,\nabla)v,\lambda) - ((\hat{w}_R\, A_R\,\nabla)\lambda, v)] \\ - I_R\, A_{R,i}\nabla\lambda_i\, q - I_R\, A_{R,i}\nabla v_i\,\pi \;-\; I_R\,(\hat{f}_R,\lambda)\,\mathrm{d}x.\end{aligned}$$

The terms I_R, A_R and $A_{R,i}$ account for the mapping and are smooth functions with respect to R. By re-mapping to the physical domain, we observe that $E(v(R),q(R);R) = 0$ for a suitable $q(R) \in L^2_0(\widehat{\Omega})$ and $\partial_{(v,q)}E((v,q);R)$ is regular for arbitrary $R \in \mathcal{G}$. From the representation of E we observe its smoothness with respect to R. Hence, the implicit function theorem ensures smoothness of the well-posed mapping $R \mapsto v(R)$.

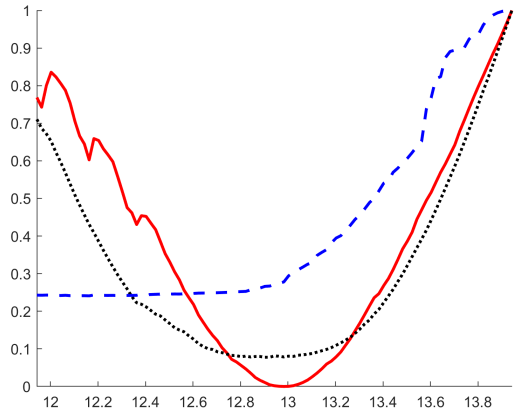

Figure 4.8: Normalized data based geometry enhancement functional $J_{\text{data}}(R)$ (blue, dashed) and model based geometry enhancement functional $J_{\text{data}}(R)$ (black, dotted) alongside the normalized mean wall shear stress error $\text{ERR}_{\text{WSS}}(R)$ (red) for different samples of the geometry parameter R; x-axis are mean values of R in [mm].

The smooth dependence of the model velocity on the geometry is in accordance with the actual physical dependence of the flow velocity with respect to the geometry.

Numerical experiment. To test the principle capability of the geometry enhancement functionals J_{data} and J_{model} for identifying the geometry, we consider the experimental setup of 4.4.2 with resting conditions $\text{Re}_{\max} = 4000$. We sample the lowest Fourier mode of the geometry parameter and consider $R = R_\alpha^\delta + dr$ with $dr \in [-1\text{mm}, 1\text{mm}]$.

For every sample $R \in \mathcal{G}$, we compute the corresponding data driven velocity approximation $F(R) = u_\beta^\varepsilon(R)$, the wall shear stress $\tau_\beta^\varepsilon(R)$ and the model velocity $u(R)$. Then we evaluate the functionals $J_{\text{data}}(R)$ and $J_{\text{model}}(R)$ as well as - using the exact solution - the squared mean wall shear stress error on the parameter domain D

$$\text{ERR}_{\text{WSS}}(R) := \left| \int_D \widehat{\tau}_\beta^\varepsilon(R) - \widehat{\tau}^\dagger \, \mathrm{d}(\varphi, s) \right|^2.$$

Note that the geometry enhancement functionals are computable without knowledge of the exact data $R^\dagger$ and $u^\dagger$.

The numerical results are depicted in Figure 4.8. The data based geometry enhancement functional reveals a plateau, the minimizer is $R_{\text{data}} = 12.1\text{mm}$, resulting in a high error of the corresponding wall shear stress estimate. The model based geometry enhancement functional, on the other hand, exhibits a clear minimum at $R_{\text{model}} = 12.92\text{mm}$ that is in good accordance with the exact geometry $R^\dagger = 12.94\text{mm}$. As expected, the estimated wall shear stress clearly depends on the geometry parameter with the best estimation at $R \approx R^\dagger$. While the data based geometry enhancement leads to large wall shear stress estimation errors, in our experimental setup the model based technique is capable to provide accurate estimates of the wall shear stress without requiring highly accurate geometry

reconstructions.

Outlook. Inspired from these results, one might think about reconstructing the whole geometry parameter R using the model based geometry enhancement functional. Similar problems arise in the context of shape optimization [43] and are typically ill-posed [18]. Hence, we should apply Tikhonov regularization leading to the model informed geometry identification problem

$$\min_{R \in H^3(D) \cap \mathcal{G}} \|F(R) - u(R)\|^2_{L^2(\Omega_C)} + \alpha \|R\|^2_{H^3(D)}.$$

This problems fit into the framework of Tikhonov regularization for non-linear inverse problems in Hilbert spaces that was presented in Subsection 2.2.2, but is beyond the scope of this investigation.

Summary. In this chapter, we have presented model based strategies for the enhancement of the purely data driven reconstruction of flow geometry, velocity and wall shear stress. The underlying fluid dynamical model makes wide use of the available data driven approximations of the flow velocity, to linearize and temporally localize the Navier-Stokes equations, leading to a well-posed quasistationary Oseen model that is stable with respect to perturbations of the convective velocity. In the numerical application, a local restriction to a thin boundary layer leads to linear problems of moderate dimension that can be solved with feasible computational effort.

The problem that purely data driven velocity approximations can not sufficiently resolve the boundary layer for physiologically realistic flows, indicated from the phase inaccuracy, is tackled with a variational data assimilation approach. Although more expensive reconstruction strategies eliminating the linearization errors in the flow model lead to better results, the data assimilation using the quasistationary Oseen model already provides a significant improvement of the purely data driven velocity approximations.

Finally, we briefly presented an approach for a model based enhancement of the geometry reconstruction. The approach is based on the observation that the purely data driven velocity approximation exhibits a high sensitivity to the geometry, but produces reasonable approximations of the velocity for sufficiently accurate geometry. The flow model, however, resembles the moderate sensitivity of the real physical flow on the geometry. Therefore, a low deviation between the purely data driven and the model based velocity should characterize the actual geometry. A first numerical example confirmed this strategy, rendering the approach an interesting subject for further research.

Chapter 5

Summary

In this thesis, we investigated the problem of reconstructing wall shear stress from magnetic resonance data for the application in the medical practice. For its solution we proposed a purely data driven technique that sequentially reconstructs the flow geometry, velocity and, finally, the wall shear stress. The reconstruction problems for the geometry and velocity are ill-posed and, therefore, solved utilizing Tikhonov regularization. Based on a conditional stability estimate, we were able to provide a comprehensive analysis of the wall shear stress estimation problem, that also covers the numerical realization and establish error bounds for the resulting estimate in terms of the measurement noise. Our theory expects a high amplification of geometry reconstruction errors, making the accurate reconstruction of the flow geometry the crucial ingredient for the wall shear stress estimation.

An extensive validation including the wall shear stress estimation from actual magnetic resonance measurements of flows that are dynamic similar to the flows in the human aorta and for which *ground truth*, i.e. highly accurate reference values, are accessible, proved the basic applicability of the technique. In particular, this holds for considerably low data resolution, where the reconstruction benefits from a detailed data acquisition model. On the other hand, we discovered the limitations of the method, such as unresolved boundary layers due to the low resolution, and confirmed the critical sensitivity with respect to the geometry.

As a remedy for these issues, we investigated the suitable incorporation of a basic fluid dynamical model. The velocity approximations, obtained from the purely data driven technique, allow for linearizing and localizing the fluid dynamical model in space and time. Hence, solutions can be computed under feasible computational effort. The numerical examples revealed the potential of this simplified and data driven model to provide valuable additional information about the flow, in particular in the inner boundary layer. Regarding the limitations to resolve the boundary layer, we proposed a variational data assimilation technique for the enhancement of the purely data driven velocity approximation using the linearized quasistationary model, leading to a significant reduction of the approximation error.

In a first numerical experiment, we also observed that model informed techniques offer the possibility to enhance the geometry reconstruction. The comprehensive analysis in the context of parameter estimation is an interesting subject for further research. Regarding the model informed techniques, improvements can also be expected from the incorporation of

stabilization techniques and better suited flow models, in particular for the blood rheology. However, the development of appropriate preconditioners for the arising systems, to unlock high dimensional discretizations, appears difficult: apart from the saddlepoint structure the presence of convection and the high aspect ratio of the considered geometries are major obstacles.

From a more practical perspective, reliable fully automatic pre-segmentation techniques are desired. The *in vivo* application requires the incorporation of moving geometries into the framework. In view of the sensitivity to geometry errors, multimodal measurements should be taken into consideration, where the geometry is identified using, for instance, computer tomography and only the translation and rotation of the geometry in the magnetic resonance field of view is detected from the magnetic resonance data.

In conclusion, referring back to the observation of Petersson et al. [69] that all data driven methods are impacted by considerable errors, we may reply: the sources of estimation errors in a data driven reconstruction are widely understood. With treating these problems appropriately, valuable wall shear stress estimation for physiologically realistic flow regimes from magnetic resonance imaging data appears possible.

Bibliography

[1] R. A. Adams and J. J. F. Fournier. *Sobolev Spaces*. Elsevier Science, 2003.

[2] M. Andersson, J. Lantz, T. Ebbers, and M. Karlsson. Multidirectional WSS Disturbances in Stenotic Turbulent Flows: A Pre-and Post-Intervention Study in an Aortic Coarctation. *Journal of Biomechanics*, 51:8–16, 2017.

[3] M. A. G. Ballester, A. P. Zisserman, and M. Brady. Estimation of the Partial Volume Effect in MRI. *Medical Image Analysis*, 6:389–405, 2002.

[4] A. J. Barker, C. Lanning, and R. Shandas. Quantification of Hemodynamic Wall Shear Stress in Patients with Bicuspid Aortic Valve using Phase-Contrast MRI. *Annals of Biomedical Engineering*, 38:788–800, 2010.

[5] A. J. Barker, M. Markl, J. Burk, R. Lorenz, J. Bock, S. Bauer, J. Schulz-Meger, and F. von Knobelsdorff-Brenkenhoff. Bicuspid Aortic Valve Is Associated with Altered Wall Shear Stress in the Ascending Aorta. *Circulation Cardiovascular Imaging*, 5:457–466, 2012.

[6] D. M. Barker, W. Huang, Y. R. Guo, A. J. Bourgeois, and Q. N. Xiao. A Three-dimensional Variational Data Assimilation System for MM5: Implementation and Initial Results. *Monthly Weather Review*, 132:897–914, 2004.

[7] A. Bauer, M. Bopp, S. Jakirlic, C. Tropea, A. J. Krafft, N. Shokina, and J. Hennig. Analysis of the Wall Shear Stress in a Generic Aneurysm under Pulsating and Transitional Flow Conditions. *Experiments in Fluids*, 61:1–16, 2020.

[8] A. Bauer, S. Wegt, M. Bopp, S. Jakirlic, C. Tropea, A. J. Krafft, N. Shokina, J. Hennig, G. Teschner, and H. Egger. Comparison of Wall Shear Stress Estimates Obtained by Laser Doppler Velocimetry, Magnetic Resonance Imaging and Numerical Simulations. *Experiments in Fluids*, 60:1–16, 2019.

[9] A. Binder, H. W. Engl, A. Neubauer, O. Scherzer, and C. W. Groetsch. Weakly Closed Nonlinear Operators and Parameter Identification in Parabolic Equations by Tikhonov Regularization. *Applicable Analysis*, 55:215–234, 1994.

[10] G. Biros and O. Ghattas. Parallel Lagrange–Newton–Krylov–Schur Methods for PDE-Constrained Optimization. Part II: The Lagrange–Newton Solver and its Application to Optimal Control of Steady Viscous Flows. *SIAM Journal on Scientific Computing*, 27:714–739, 2005.

[11] B. Blaschke, A. Neubauer, and O. Scherzer. On Convergence Rates for the Iteratively Regularized Gauss-Newton Method. *IMA Journal of Numerical Analysis*, 17:421–436, 1997.

[12] D. Braess. *Finite Elemente: Theorie, Schnelle Löser und Anwendungen in der Elastizitätstheorie*. Springer, 5th edition, 2013.

[13] F. Brezzi. On the Existence, Uniqueness and Approximation of Saddle-point Problems Arising from Lagrangian Multipliers. *R.A.I.R.O. Analyse Numérique*, 8:129–151, 1974.

[14] A. N. Brooks and T. J. R. Hughes. Streamline Upwind/Petrov-Galerkin Formulations for Convection Dominated Flows with Particular Emphasis on the Incompressible Navier-Stokes Equations. *Computer Methods in Applied Mechanics and Engineering*, 32:199–259, 1982.

[15] R. W. Brown, Y. C. N. Cheng, E. M. Haacke, M. R. Thompson, and R. Venkatesan. *Magnetic Resonance Imaging: Physical Principles and Sequence Design*. Wiley-Blackwell, 2nd edition, 2014.

[16] M. Bruschewski, M. H. A. Piro, C. Tropea, and S. Grundmann. Fluid Flow in a Diametrally Expanded CANDU Fuel Channel – Part 1: Experimental Study. *Nuclear Engineering and Design*, 357:110371, 2019.

[17] K. B. Chandran, S. E. Rittgers, and A. P. Yoganathan. *Biofluid Mechanics: The Human Circulation, Second Edition*. CRC Press, 2nd edition, 2012.

[18] D. Chenais and E. Zuazua. Controllability of an Elliptic Equation and its Finite Difference Approximation by the Shape of the Domain. *Numerische Mathematik*, 95:63–99, 2003.

[19] J. Cheng and M. Yamamoto. One New Strategy for A Priori Choice of Regularizing Parameters in Tikhonov's Regularization. *Inverse Problems*, 16:31–38, 2000.

[20] F. H. Clauser. The Turbulent Boundary Layer. *Advances in Applied Mechanics*, 4:1–51, 1956.

[21] C. De Boor. *A Practical Guide to Splines (Revised Edition)*. Springer, 1st edition, 2001.

[22] A. A. Duquette, P. M. Jodoin, O. Bouchot, and A. Lalande. 3D Segmentation of Abdominal Aorta From CT-Scan and MR Images. *Computerized Medical Imaging and Graphics*, 36:294–303, 2012.

[23] H. Egger and B. Hofmann. Tikhonov Regularization in Hilbert Scales under Conditional Stability Assumptions. *Inverse Problems*, 34:115015, 2018.

[24] H. Egger, T. Seitz, and C. Tropea. Enhancement of Flow Measurements using Fluid-Dynamic Constraints. *Journal of Computational Physics*, 344:558–574, 2017.

[25] H. Egger and G. Teschner. On the Stable Estimation of Flow Geometry and Wall Shear Stress from Magnetic Resonance Images. *Inverse Problems*, 35:095001, 2019.

[26] C. J. Elkins and M. T. Alley. Magnetic Resonance Velocimetry: Applications of Magnetic Resonance Imaging in the Measurement of Fluid Motion. *Experiments in Fluids*, 43:823–858, 2007.

[27] H. C. Elman, D. J. Silvester, and A. J. Wathen. *Finite Elements and Fast Iterative Solvers: with Applications in Incompressible Fluid Dynamics*. Oxford University Press, 2nd edition, 2014.

[28] H. W. Engl, M. Hanke, and A. Neubauer. *Regularization of Inverse Problems*. Springer, 1996.

[29] H. W. Engl, K. Kunisch, and A. Neubauer. Convergence Rates for Tikhonov Regularisation of Non-Linear Ill-Posed Problems. *Inverse Problems*, 5:523–540, 1989.

[30] I. Ergatoudis, B. M. Irons, and O. C. Zienkiewicz. Curved, Isoparametric, Quadrilateral Elements for Finite Element Analysis. *International Journal of Solids and Structures*, 4:31–42, 1968.

[31] C. L. Fefferman. Existence and Smoothness of the Navier-Stokes Equation. *The Millennium Prize Problems*, 57:22, 2006.

[32] J. H. Ferziger and M. Perić. *Numerische Strömungsmechanik*. Springer, 1st edition, 2008.

[33] D. P. G. Foures, N. Dovetta, D. Sipp, and P. J. Schmid. A Data-Assimilation Method for Reynolds-Averaged Navier–Stokes-Driven Mean Flow Reconstruction. *Journal of Fluid Mechanics*, 759:404–431, 2014.

[34] D. Freudenhammer, E. Baum, B. Peterson, B. Böhm, B. Jung, and S. Grundmann. Volumetric Intake Flow Measurements of an IC Engine using Magnetic Resonance Velocimetry. *Experiments in Fluids*, 55:1724–100, 2014.

[35] J. Garcia, A. J. Barker, and M. Markl. The Role of Imaging of Flow Patterns by 4D Flow MRI in Aortic Stenosis. *JACC: Cardiovascular Imaging*, 12:252–266, 2019.

[36] P. Gauthier, M. Tanguay, S. Laroche, S. Pellerin, and J. Morneau. Extension of 3DVAR to 4DVAR: Implementation of 4DVAR at the Meteorological Service of Canada. *Monthly Weather Review*, 135:2339–2354, 2007.

[37] O. Ghattas and J. H. Bark. Optimal Control of Two- and Three-dimensional Incompressible Navier–Stokes Flows. *Journal of Computational Physics*, 136:231–244, 1997.

[38] M. A. Gimbrone, T. Nagel, and J. N. Topper. Biomechanical Activation: an Emerging Paradigm in Endothelial Adhesion Biology. *J. Clinical Investigation*, 99:1809–1813, 1997.

[39] V. Girault and P. A. Raviart. *Finite Element Methods for Navier-Stokes Equations: Theory and Algorithms*. Springer, 1986.

[40] J. L. Guermond, J. T. Oden, and S. Prudhomme. Mathematical Perspectives on Large Eddy Simulation Models for Turbulent Flows. *Journal of Mathematical Fluid Mechanics*, 6:194–248, 2004.

[41] M. Gunzburger. Adjoint Equation-Based Methods for Control Problems in Incompressible, Viscous Flows. *Flow, Turbulence and Combustion*, 65:249–272, 2000.

[42] J. Hadamard. *Lectures on Cauchy's Problem in Linear Partial Differential Equations*. Yale University Press, 1923.

[43] H. Harbrecht. Analytical and Numerical Methods in Shape Optimization. *Mathematical Methods in the Applied Sciences*, 31:2095–2114, 2008.

[44] M. Hinze, R. Pinnau, M. Ulbrich, and S. Ulbrich. *Optimization with PDE Constraints*. Springer, 1st edition, 2008.

[45] E. Hopf. Über die Anfangswertaufgabe für die Hydrodynamischen Grundgleichungen. Erhard Schmidt zu seinem 75. Geburtstag Gewidmet. *Mathematische Nachrichten*, 4:213–231, 1950.

[46] M. C. Hsu and Y. Bazilevs. Blood Vessel Tissue Prestress Modeling for Vascular Fluid-Structure Interaction Simulation. *Finite Elements in Analysis and Design*, 47:593–599, 2011.

[47] F. Irgens. *Rheology and Non-Newtonian Fluids*. Springer International Publishing, 1st edition, 2014.

[48] K. Ito, K. Kunisch, and G. H. Peichl. Variational Approach to Shape Derivatives. *ESAIM Control Optimisation and Calculus of Variations*, 14:517–539, 2008.

[49] B. Kaltenbacher, T. T. N. Nguyen, and O. Scherzer. The Tangential Cone Condition for some Coefficient Identification Model Problems in Parabolic PDEs. In *Time-Dependent Problems in Imaging and Parameter Identification*, pages 121–163. Springer International Publishing, 2021.

[50] V. P. Kamphuis, J. J. M. Westenberg, R. L. F. van der Palen, N. A. Blom, A. de Roos, R. van der Geest, M. S. M. Elbaz, and A. A. W. Roest. Unravelling Cardiovascular Disease using Four Dimensional Flow Cardiovascular Magnetic Resonance. *The International Journal of Cardiac Imaging*, 33:1069–1081, 2017.

[51] E. Karabelas, M. A. F. Gsell, C. M. Augustin, L. Marx, A. Neic, A. J. Prassl, L. Goubergrits, T. Kuehne, and G. Plank. Towards a Computational Framework for Modeling the Impact of Aortic Coarctations upon Left Ventricular Load. *Frontiers in Physiology*, 9:538, 2018.

[52] G. K. Khoury, P. Schlatter, A. Noorani, P. F. Fischer, G. Brethouwer, and A. V. Johansson. Direct Numerical Simulation of Turbulent Pipe Flow at Moderately High Reynolds Numbers. *Flow, Turbulence and Combustion*, 91:475–495, 2013.

[53] A. Kolipaka, V. S. P. Illapani, P. Kalra, J. Garcia, X. Mo, M. Markl, and R. D. White. Quantification and Comparison of 4D-Flow MRI-Derived Wall Shear Stress and MRE-derived Wall Stiffness of the Abdominal Aorta. *Journal of Magnetic Resonance Imaging*, 45:771–778, 2017.

[54] T. S. Koltukluoğlu and P. J. Blanco. Boundary Control in Computational Haemodynamics. *Journal of Fluid Mechanics*, 847:329–364, 2018.

[55] W. Kühnel. *Differentialgeometrie: Kurven - Flächen - Mannigfaltigkeiten*. Springer, 6th edition, 2013.

[56] J. Leray. Sur Le Mouvement D'un Liquide Visqueux Emplissant L'espace. *Acta Mathematica*, 63:193–248, 1934.

[57] J. Li, M. Yamamoto, and J. Zou. Conditional Stability and Numerical Reconstruction of Initial Temperature. *Communications on Pure & Applied Analysis*, 8:361–382, 2009.

[58] A. Manzoni, A. Quarteroni, and S. Salsa. A Saddle Point Approach to an Optimal Boundary Control Problem for Steady Navier-Stokes Equations. *Mathematics in Engineering*, 1:252–280, 2019.

[59] M. Markl, S. Schnell, C. Wu, E. Bollache, K. Jarvis, A. J. Barker, J. D. Robinson, and R. C. K. Advanced Flow MRI: Emerging Techniques and Applications. *Clinical Radiology*, 71:779–795, 2016.

[60] G. McGibney. An Unbiased Signal-to-Noise Ratio Measure for Magnetic Resonance Images. *Medical Physics*, 20:1077–1078, 1993.

[61] L. F. Moody. Friction Factors for Pipe Flow. *Trans. Asme*, 66:671–684, 1944.

[62] D. Mumford and J. Shah. Optimal Approximations by Piecewise Smooth Functions and Associated Variational Problems. *Communications on Pure and Applied Mathematics*, 42:577–685, 1989.

[63] K. S. Nayak, J. Nielsen, M. A. Bernstein, M. Markl, P. D. Gatehouse, R. M. Botnar, D. Saloner, C. Lorenz, H. Wen, B. S. Hu, F. H. Epstein, J. N. Oshinski, and S. V. Raman. Cardiovascular Magnetic Resonance Phase Contrast Imaging. *Journal of Cardiovascular Magnetic Resonance*, 17:1–26, 2015.

[64] A. Neubauer. When Do Sobolev Spaces Form a Hilbert Scale? *Proceedings of the American Mathematical Society*, 103:557–562, 1988.

[65] M. A. Olshanskii and E. V. Chizhonkov. On the Best Constant in the Inf-Sup-Condition for Elongated Rectangular Domains. *Mathematical Notes*, 67:325–332, 2000.

[66] S. Osher and R. P. Fedkiw. Level Set Methods: An Overview and Some Recent Results. *Journal of Computational Physics*, 169:463–502, 2001.

[67] J. N. Osinnski, D. Ku, S. Mukundan, F. Loth, and R. I. Pettigrew. Determination of Wall Shear Stress in the Aorta with the Use of MR Phase Velocity Mapping. *Journal of Magnetic Resonance Imaging*, 5:640–647, 1995.

[68] S. Oyre, S. Ringgaard, S. Kozerke, W. P. Paaske, M. B. Scheidegger, P. Boesiger, and E. M. Pedersen. Quantitation of Circumferential Subpixel Vessel Wall Position and Wall Shear Stress by Multiple Sectored Three-Dimensional Paraboloid Modeling of Velocity Encoded CINE MR. *Magnetic Resonance in Medicine*, 40:645–655, 1998.

[69] S. Petersson, P. Dyverfeldt, and T. Ebbers. Assessment of the Accuracy of MRI Wall Shear Stress Estimation using Numerical Simulations. *Journal of Magnetic Resonance Imaging*, 36:128–138, 2012.

[70] F. Piatti, S. Pirola, M. Bissell, I. Nesteruk, F. Sturla, A. C. Della, A. Redaelli, and E. Votta. Towards the Improved Quantification of In Vivo Abnormal Wall Shear Stresses in BAV-Affected Patients from 4D-Flow Imaging: Benchmarking and Application to Real Data. *Journal of Biomechanics*, 50:93–101, 2016.

[71] R. Pohle and K. D. Toennies. Segmentation of Medical Images using Adaptive Region Growing. In *Medical Imaging 2001: Image Processing*, volume 4322, pages 1337–1346. International Society for Optics and Photonics, 2001.

[72] W. V. Potters, H. A. Marquering, E. van Bavel, and A. J. Nederveen. Measuring Wall Shear Stress using Velocity-Encoded MRI. *Current Cardiovascular Imaging Reports*, 7:1–12, 2014.

[73] W. V. Potters, P. van Ooij, H. Marquering, E. van Bavel, and A. J. Nederveen. Volumetric Arterial Wall Shear Stress Calculation Based on CINE Phase Contrast MRI. *Journal of Magnetic Resonance Imaging*, 41:505–516, 2015.

[74] M. Raissi, P. Perdikaris, and G. E. Karniadakis. Physics-Informed Neural Networks: A Deep Learning Framework for Solving Forward and Inverse Problems Involving Nonlinear Partial Differential Equations. *Journal of Computational Physics*, 378:686–707, 2019.

[75] G. A. Roth et al. Global Burden of Cardiovascular Diseases and Risk Factors, 1990-2019. *Journal of the American College of Cardiology*, 76:2982–3021, 2020.

[76] P. Sagaut. *Large Eddy Simulation for Incompressible Flows: an Introduction*. Springer Science & Business Media, 2006.

[77] A. V. Salsac, S. R. Sparks, J. M. Chomaz, and J. C. Lasheras. Evolution of the Wall Shear Stresses during the Progressive Enlargement of Symmetric Abdominal Aortic Aneurysms. *Journal of Fluid Mechanics*, 560:19–51, 2006.

[78] O. Scherzer. Convergence Criteria of Iterative Methods Based on Landweber Iteration for Solving Nonlinear Problems. *Journal of Mathematical Analysis and Applications*, 194:911–933, 1995.

[79] H. Schlichting, K. Gersten, E. Krause, and H. Oertel. *Boundary-Layer Theory*. Springer, 9th edition, 2017.

[80] J. Seitz, M. Strotzer, J. Schlaier, W. R. Nitz, M. Völk, and S. Feuerbach. Comparison Between Magnetic Resonance Phase Contrast Imaging and Transcranial Doppler Ultrasound with Regard to Blood Flow Velocity in Intracranial Arteries: Work in Progress. *Journal of Neuroimaging*, 11:121–128, 2001.

[81] T. Seitz. *Geometry Identification and Data Enhancement for Distributed Flow Measurements*. Phd thesis, Technische Universität Darmstadt, 2018.

[82] A. M. Shaaban and A. J. Duerinckx. Wall Shear Stress and Early Atherosclerosis. *American Journal of Roentgenology*, 174:1657–1665, 2000.

[83] M. Shojima, M. Oshima, K. Takagi, R. Torii, M. Hayakawa, K. Katada, A. Morita, and T. Kirino. Magnitude and Role of Wall Shear Stress on Cerebral Aneurysm: Computational Fluid Dynamic Study of 20 Middle Cerebral Artery Aneurysms. *Stroke*, 35:2500–2505, 2004.

[84] N. Shokina, A. Bauer, G. Teschner, W. B. Buchenberg, C. Tropea, H. Egger, J. Hennig, and A. J. Krafft. MR-based Wall Shear Stress Measurements in Fully Developed Turbulent Flow using the Clauser Plot Method. *Journal of Magnetic Resonance*, 305:16–21, 2019.

[85] N. Shokina, G. Teschner, A. Bauer, C. Tropea, H. Egger, J. Hennig, and A. J. Krafft. Quantification of Wall Shear Stress in Large Blood Vessels using Magnetic Resonance Imaging. *Computational Technologies*, 24:4–27, 2019.

[86] N. Shokina, G. Teschner, A. Bauer, C. Tropea, H. Egger, J. Hennig, and A. J. Krafft. Parametric Sequential Method for MRI-based Wall Shear Stress Quantification. *IEEE Transactions on Medical Imaging*, 40:1105–1112, 2020.

[87] J. A. Staessen, J. Wang, G. Bianchi, and W. H. Birkenhäger. Essential Hypertension. *The Lancet*, 361:1629–1641, 2003.

[88] A. F. Stalder, M. F. Russe, A. Frydrychowicz, J. Bock, J. Hennig, and M. Markl. Quantitative 2D and 3D Phase Contrast MRI: Optimized Analysis of Blood Flow and Vessel Wall Parameters. *Magnetic Resonance in Medicine*, 60:1218–1231, 2008.

[89] P. D. Stein and H. N. Sabbah. Turbulent Blood Flow in the Ascending Aorta of Humans with Normal and Diseased Aortic Valves. *Circulation Research*, 39:58–65, 1976.

[90] G. R. Tabor and M. H. Baba-Ahmadi. Inlet Conditions for Large Eddy Simulation: A Review. *Computers & Fluids*, 39:553–567, 2010.

[91] F. Tröltzsch. *Optimale Steuerung Partieller Differentialgleichungen*. Vieweg+Teubner, 2nd edition, 2009.

[92] R. Tsai et al. Level Set Methods and their Applications in Image Science. *Communications in Mathematical Sciences*, 1:1–20, 2003.

[93] G. Uhlmann. Electrical Impedance Tomography and Calderón's Problem. *Inverse Problems*, 25:123011, 2009.

[94] P. van Ooij, M. Markl, J. D. Collins, J. C. Carr, C. Rigsby, R. O. Bonow, S. C. Malaisrie, P. M. McCarthy, P. W. M. Fedak, and A. J. Barker. Aortic Valve Stenosis Alters Expression of Regional Aortic Wall Shear Stress: New Insights From a 4-Dimensional Flow Magnetic Resonance Imaging Study of 571 Subjects. *Journal of the American Heart Association Cardiovascular and Cerebrovascular Disease*, 6:e005959, 2017.

[95] F. von Knobelsdorff-Brenkenhoff, A. Karunaharamoorthy, R. F. Trauzeddel, A. J. Barker, E. Blaszczyk, M. Markl, and J. Schulz-Menger. Evaluation of Aortic Blood Flow and Wall Shear Stress in Aortic Stenosis and Its Association with Left Ventricular Remodeling. *Circulation: Cardiovascular Imaging*, 9:e004038, 2016.

[96] C. Wieners. Taylor-Hood Elements in 3D. In *Analysis and Simulation of Multifield Problems*, pages 189–196. Springer, 2003.

[97] R. A. Willoughby. Solutions of Ill-posed Problems (A. N. Tikhonov and V. Y. Arsenin). *SIAM Review*, 21:266–267, 1979.

[98] J. R. Womersley. Method for the Calculation of Velocity, Rate of Flow and Viscous Drag in Arteries when the Pressure Gradient is Known. *The Journal of Physiology*, 127:553–563, 1955.

[99] A. Zienkiewicz, M. Favre, H. Ferdinando, S. Iring, J. Serrador, and T. Myllylä. Blood Pressure Wave Propagation–a Multisensor Setup for Cerebral Autoregulation Studies. *Physiological Measurement*, 42:115007, 2021.

[100] J. Zimmermann, D. Demedts, H. Mirzaee, P. Ewert, H. Stern, C. Meierhofer, B. Menze, and A. Hennemuth. Wall Shear Stress Estimation in the Aorta: Impact of Wall Motion, Spatiotemporal Resolution, and Phase Noise. *Journal of Magnetic Resonance Imaging*, 48:718–728, 2018.

[101] W. Zulehner. Nonstandard Norms and Robust Estimates for Saddle Point Problems. *SIAM Journal on Matrix Analysis and Applications*, 32:536–560, 2011.

Wissenschaftlicher Werdegang

Wissenschaftlicher Werdegang

Gabriel Teschner

2022	Promotion Mathematik
2016 - 2021	Wissenschaftlicher Mitarbeiter in der AG Numerik an der TU Darmstadt
2014 - 2016	Studium der Mathematik an der TU Darmstadt mit Abschluss M.Sc.
2011 - 2014	Studium der Mathematik an der TU Darmstadt mit Abschluss B.Sc.
2011	Abitur am Franziskanergymnasium Kreuzburg in Großkrotzenburg